



UNIVERSITEIT VAN PRETORIA  
UNIVERSITY OF PRETORIA  
YUNIBESITHI YA PRETORIA  
Faculty of Engineering, Built Environment and  
Information Technology

DEPARTMENT OF MECHANICAL AND AERONAUTICAL ENGINEERING

**CLAMPED PLATE-STYLE RECUPERATOR FOR A  
SMALL-SCALE SOLAR THERMAL BRAYTON CYCLE  
USING HIGH-TEMPERATURE SEALANT**

by

**Kyle Eric Dellar**

Submitted in partial fulfilment of the requirements for the degree:  
Master of Engineering (Mechanical Engineering)

in the

Department of Mechanical and Aeronautical Engineering  
Faculty of Engineering, Built Environment and Information Technology

UNIVERSITY OF PRETORIA  
SOUTH AFRICA

2019

# SUMMARY

---

## CLAMPED PLATE-STYLE RECUPERATOR FOR A SMALL-SCALE SOLAR THERMAL BRAYTON CYCLE USING HIGH-TEMPERATURE SEALANT

by

**Kyle Eric Dellar**

Supervisor: Dr W. G. le Roux  
Co-supervisor: Prof J. P. Meyer  
Department: Mechanical and Aeronautical Engineering  
University: University of Pretoria  
Degree: MEng (Mechanical Engineering)  
Keywords: Recuperator; Micro-turbine; Brayton cycle; Solar.

\* \* \*

South Africa is plagued by rolling blackouts, and many citizens do not have access to electricity or clean water. A personalised micro-turbine power generation system presents a solution to this issue and may become as commonplace as a personal computer. With South Africa's excellent solar direct normal irradiation (DNI) levels, a small-scale recuperated solar thermal Brayton cycle (STBC) shows enormous potential. However, a recuperator comprises up to 30% of the capital cost associated with a micro-turbine package and requires complex and costly manufacturing methods within a South African context. Thus, the objective of this research is to investigate a clamped plate-style recuperator that can be cost-effectively manufactured locally. Literature was consulted and criteria were outlined that a recuperator in a Brayton cycle should adhere to. To uphold these requirements, a counterflow plate-style recuperator is mandatory, and to combat complex manufacturing methods, a gasketed stacked-plate design, which requires a gasket material, was proposed. A sodium silicate-based sealant called Soudal Calofer is available locally and can withstand the operating conditions of an STBC. Experimental testing was carried out successfully on two small-scale versions of the proposed

recuperator design. Testing showed that the physical construction was simple and cost-effective and the clamped plate-style high-temperature sealant combination worked well to form the recuperator core, facilitating an easy assembly and disassembly process. The construction sustained an airtight seal (Mark I) for the entire testing period at various pressures and high temperatures. Despite the occurrence of heavy soot-based fouling deposits during Test 1 due to incomplete combustion of the LPG as a result of the very low air mass flow rates, a mathematical model was able to match the values gathered from the testing. The data showed a cold-side effectiveness of 58.6% and a total pressure loss of 17.78%. For Test 2, a cold-side effectiveness of 82.5% and a total pressure loss of 11.48% were found for the recuperator core, which also validated the mathematical model. A case study was performed for the small-scale STBC. The results showed that the combination of a cold-side effectiveness of 84% and a total pressure loss of less than 5% could be attained when implementing the recuperator within the STBC for a channel height of 1 mm and width of 50 mm. Alternatively, if pressure loss is of less concern, a cold-side effectiveness of 89% could be achieved by increasing the total pressure loss to 19 kPa, which equates to an 8.8% pressure loss. It is recommended that a large-scale recuperator be built and tested to confirm the performance characteristics of larger mass flow rates and that the insulation of the unit be varied to determine its effects. Gasket geometry and the assembly method also need to be further researched to develop a uniform and consistent assembly technique that results in an airtight seal for every unit assembled. This may be achieved by regulating the amount of water added to the Soudal Calofer for thinning purposes to achieve a consistency which facilitates uniform application and by extended drying time to allow for the assembly to be completed, while not thinning the sealant so much as to lead to a seal failure. In conjunction, the clamping force distribution is critical to sealing the inner channel division. It is also recommended that the usable lifespan of such a recuperator be determined. Most crucially, thermal and pressure cycling must be investigated, especially where seal integrity is concerned.

## ACKNOWLEDGEMENTS

---

To my supervisor and now good friend, Dr Willem le Roux, and his wife, Leandri, I cannot express my gratitude enough. You have taught me so much. I have never come across a teacher and mentor with as much patience, insight and wisdom as you. It was an absolute pleasure to travel this part of my life's journey with you. May you both continue to live a long, happy and prosperous life.

I would like to extend my gratitude to Professor Meyer for his supervision and support.

Praise is also due to the largely unsung heroes of the department. To Tersia Evans, Ilka Meyer, Karabo Kunene, Bonolo Mokoka and Estelle Greyling, you ladies are the backbone of the Clean Energy Research Group (CERG). Additionally, I must express my gratitude to Peet Kruger, Edwin Mohale, Wim Murray, Chris Govinder, Donald Keetse and Koos Mthombeni. If not for these gentlemen, most of the research carried out within the engineering faculty would not be possible.

To my fellow colleagues and to the lecturers within CERG, I appreciate the time and effort you lent me during my studies. Your intelligence and insight inspired me to strive for academic excellence.

*This work is based on the research supported by the National Research Foundation (NRF) of South Africa (Grant Number 109311), the Technology Innovation Agency of South Africa (TIA) and the University of Pretoria's Research and Development Plan (RDP). Opinions expressed, and conclusions arrived at are those of the author and are not necessarily to be attributed to the NRF, TIA or RDP.*

Lastly, thank you to my family and friends for their never-ending support and love. You have earned this too.

# RESEARCH OUTPUTS

---

## Conference papers

The following papers from this work were presented at conferences:

1. Dellar, K. E., Le Roux, W. G. and Meyer, J. P., 2018. Small-Scale Solar Thermal Brayton Cycle Recuperator: Experimental Testing and Heat Loss Analysis. In: Proceedings of the 5<sup>th</sup> Southern Africa Solar Energy Conference (SASEC 2018), 25-27 June, Durban, South Africa.
2. Dellar, K. E., Le Roux, W. G. and Meyer, J. P., 2018. Experimental Testing of a Small-Scale Solar Thermal Brayton Cycle Recuperator. In: Proceedings of the 16<sup>th</sup> International Heat Transfer Conference (IHTC 2018), pp. 4815-4822, 10-15 August, Beijing, China.

## Patent

1. Le Roux, W. G. and Dellar K. E., South African Patent Application No. 2019/03915 in the name of UNIVERSITY OF PRETORIA – "Recuperator".

## Journal paper

1. The findings from this work have been summarized into a manuscript which has been submitted for publication in a suitable journal.

# TABLE OF CONTENTS

---

SUMMARY .....	i
ACKNOWLEDGEMENTS.....	iii
RESEARCH OUTPUTS.....	iv
LIST OF FIGURES .....	viii
LIST OF TABLES .....	x
NOMENCLATURE .....	xi
1 INTRODUCTION .....	1
1.1 Background .....	1
1.2 Current technologies .....	3
1.3 Problem statement.....	4
1.4 Research objective.....	5
1.5 Thesis overview.....	5
2 LITERATURE STUDY .....	7
2.1 Introduction .....	7
2.2 Brayton cycle.....	7
2.3 Micro-turbines.....	9
2.3.1 Remote control jet aeroplane and helicopter turbine engines.....	10
2.3.2 Turbochargers and future outlook.....	11
2.4 Solar thermal Brayton cycle.....	13
2.5 Recuperators.....	16
2.6 Summary .....	21
3 THEORETICAL MODEL .....	22
3.1 Introduction .....	22
3.2 Recuperator concept.....	22

3.3	Heat transfer calculation.....	24
3.4	Heat loss analysis .....	25
3.5	Pressure drop analysis .....	28
3.6	Stress analysis .....	29
3.7	Summary .....	30
4	EXPERIMENTAL SETUP .....	31
4.1	Introduction .....	31
4.2	Test 1 – Mark I rig.....	31
4.3	Test 2 – Mark II rig .....	33
4.4	Cost analysis.....	36
4.5	Experimental procedure .....	37
4.6	Summary .....	38
5	TESTING AND RESULTS.....	40
5.1	Introduction .....	40
5.2	Test 1 .....	40
5.2.1	Temperatures.....	40
5.2.2	Pressures .....	44
5.2.3	Mass flow rate.....	45
5.2.4	Results.....	45
5.2.5	Model validation .....	47
5.3	Test 2.....	49
5.3.1	Temperatures.....	49
5.3.2	Pressures .....	50
5.3.3	Mass flow rate.....	51
5.3.4	Results and validation .....	53
5.4	Summary .....	54

6	CASE STUDY.....	56
6.1	Introduction.....	56
6.2	Results.....	56
6.3	Summary.....	60
7	SUMMARY, CONCLUSION AND RECOMMENDATIONS.....	62
7.1	Summary.....	62
7.2	Conclusion.....	62
7.3	Recommendations.....	63
8	REFERENCES.....	65
	APPENDICES.....	A-1
	Appendix A Soudal Calofer specification sheet (Soudal, 2015).....	A-1
	Appendix B Suto mass flow meter calibration certificate.....	B-1
	Appendix C Pressure transducer calibration certificate.....	C-1
	Appendix D In-stream K-Type thermocouple calibration certificate.....	D-1
	Appendix E Weld-pad K-Type thermocouple calibration certificate.....	E-1
	Appendix F Error propagation analysis.....	F-1



## LIST OF FIGURES

---

Figure 1 Direct normal irradiance (DNI) distribution map of South Africa (left) and North America (right) (Solargis, 2019).....	2
Figure 2 Capstone C30 (left) and MTT EnerTwin Micro-CHP (right) micro-turbines (Capstone (2019); MTT (2019)). .....	3
Figure 3 Temperature-entropy diagram of an ideal turbo-jet engine.....	7
Figure 4 Recuperated gas turbine Brayton cycle. ....	8
Figure 5 Recuperated micro-turbine with integrated generator produced by Capstone (2019).	9
Figure 6 RC micro-jet engine (Mirshahidi, 2012). ....	10
Figure 7 Turbocharger schematic model (Garrett, 2009). ....	11
Figure 8 Magneti Marelli TERS turbocharger (Formula 1 Dictionary, 2014). ....	12
Figure 9 Hybrid turbocharger with flexible coupling (Shiraishi & Ono, 2007). ....	13
Figure 10 Standard solar thermal Brayton plant. ....	14
Figure 11 The small-scale dish-mounted open STBC (Le Roux & Meyer, 2017). ....	15
Figure 12 Classification of heat exchangers (Shah, 1981). ....	16
Figure 13 Ingersoll-Rand's plate-fin recuperator (Kesseli, et al., 2003). ....	18
Figure 14 Section view of coiled pipe-in-pipe heat exchanger (Clay & Tansley, 2011). ....	18
Figure 15 Basic plate heat exchanger layout. ....	22
Figure 16 Plate-style counterflow recuperator concept. ....	23
Figure 17 Exploded view of the recuperator concept. ....	23
Figure 18 Actual recuperator cross section (top) and heat loss analysis recuperator cross section (bottom).....	28
Figure 19 Mark I recuperator gasket geometry.....	31
Figure 20 SolidWorks Mark I recuperator model (left); experimental model being assembled with Calofer (right). ....	32
Figure 21 Complete Mark I recuperator test rig. ....	32

Figure 22 Mark II recuperator gasket geometry. ....	33
Figure 23 Mark II gasket during assembly process. ....	34
Figure 24 Assembled Mark II core. ....	34
Figure 25 Partially assembled Mark II test rig.....	35
Figure 26 Complete Mark II test rig with calming section and mass flow meter.....	36
Figure 27 Mark I recuperator surface and insulation thermocouple placement. ....	43
Figure 28 Condition of the cold channels (left) and the hot channels (right). ....	47
Figure 29 Test 2 measured thermocouple temperatures versus time. ....	50
Figure 30 Mark II leak and mass balance schematic. ....	51
Figure 31 Mark II thermocouple placement. ....	52
Figure 32 Model results for effectiveness versus number of channel pairs at various channel lengths. ....	58
Figure 33 Model results for pressure loss versus number of channel pairs at various channel lengths. ....	58
Figure 34 Effectiveness (top) and pressure loss (bottom) versus number of channel pairs for different numbers of recuperators. ....	59
Figure 35 Effectiveness (top) and pressure loss (bottom) versus number of channel pairs for varying manifold tube diameters. ....	60

## LIST OF TABLES

---

Table 1 Comparison of various available and proposed micro-turbine solutions. ....	4
Table 2 Typical existing recuperator solutions, extracted from Xiao et al. (2017). ....	17
Table 3 Listing the ideal micro-Brayton cycle recuperator characteristics (McDonald, 2000). .....	19
Table 4 Properties of commonly used high-temperature recuperator materials (Ohadi & Buckley, 2001).....	20
Table 5 Average in-stream and wall temperature measurements at steady state.....	40
Table 6 Average insulation temperatures at steady state. ....	42
Table 7 Recuperator steady-state averaged heat loss temperatures. ....	44
Table 8 Recuperator steady-state averaged absolute pressures. ....	44
Table 9 Main experimental results.....	46
Table 10 Mark I theoretical model inputs.....	47
Table 11 Mark I main model outputs and comparison. ....	48
Table 12 Model heat loss temperatures and comparison. ....	49
Table 13 Test 2 steady-state fluid temperatures. ....	50
Table 14 Test 2 steady-state absolute pressure values.....	51
Table 15 Test 2 mass flow data.....	52
Table 16 Test 2 calculated hot inlet temperature. ....	53
Table 17 Mark II theoretical model inputs. ....	53
Table 18 Mark II main model outputs, experimental results and comparison.....	54
Table 19 Optimised STBC input parameters. ....	56
Table 20 Additional STBC modelling parameters.....	57

## NOMENCLATURE

---

$A$	Area	$m^2$
$A_i$	Inner area	$m^2$
$A_o$	Outer area	$m^2$
$a$	Channel width	m
$B$	Constant	-
$b$	Channel height	m
$C_p$	Specific heat	J/kg.K
$C_{rh}$	Capacity ratio	-
$D$	Diameter	m
$E$	Young's Modulus	GPa
$f$	Friction factor	-
$h$	Enthalpy	J/kg
$h$	Heat transfer coefficient	$W/m^2 \cdot ^\circ C$
$k$	Thermal conductivity	$W/m \cdot ^\circ C$
$L$	Length	m
$\dot{m}$	Mass flow rate	kg/s
$M$	Mach number	-
$N$	Number of channel pairs	-
$NR$	Number of recuperators	-
$Nu$	Nusselt number	-
$P$	Pressure	Pa
$\dot{Q}$	Heat transfer rate	W
$\dot{Q}^*$	Available solar power	W
$r$	Radius	m
$r$	Pressure ratio	-
$r_i$	Inner radius	m
$r_o$	Outer radius	m
$R$	Thermal resistance	$^\circ C/W$
$R_f$	Fouling factor	$m^2 \cdot ^\circ C/W$
$s$	Entropy	J/kg.K
$t$	Thickness	m
$T$	Temperature	$^\circ C$

$U$	Overall heat transfer coefficient	$W/m^2 \cdot ^\circ C$
$V$	Velocity	m/s
$\dot{W}$	Power	W
$x$	Distance	m
$y$	Deflection	m
<b>Greek symbols</b>		
$\varepsilon$	Effectiveness	-
$\rho$	Density	$kg/m^3$
$X$	Dimensionless position	-
$\chi$	Dimensionless external heat loss	-
$\theta$	Dimensionless temperature difference	-
$\sigma$	Mechanical stress	Pa
$\gamma$	Gas constant	-
<b>Subscripts</b>		
$25$	Depth of 25 mm	-
$50$	Depth of 50 mm	-
$at$	After throttle	-
$atm$	Atmospheric	-
$avg$	Average	-
$btm$	Bottom of	-
$bs$	Bottom surface	-
$c$	Compressor (only in Figure 11)	-
$c$	Cold	-
$cch$	Combustion chamber exhaust	-
$channel$	Per channel	-
$end$	The end of the body	-
$f$	Fouling	-
$h$	Hot	-
$h$	Hydraulic	-
$headertube$	Associated with the header tube	-
$i$	Inlet	-
$inr$	On the inside (inner)	-
$ins$	Insulation	-
$leak$	Denotes the leak value	-
$loss$	Loss of	-

<i>max</i>	Maximum	-
<i>mid</i>	Middle	-
<i>net</i>	Net	-
<i>o</i>	Outlet	-
<i>outr</i>	On the outside (outer)	-
<i>s</i>	Surface	-
<i>side</i>	Side of	-
<i>ss</i>	Side surface	-
<i>SS</i>	Stainless steel	-
<i>steel</i>	For steel	-
<i>t</i>	Tube	-
<i>t</i>	Turbine	-
<i>throttle</i>	Associated with the throttle plate	-
<i>top</i>	Top of	-
<i>tot</i>	Total	-
<i>ts</i>	Top surface	-
<i>tubes</i>	Per tube	-
<i>w</i>	Wall	-
$\infty$	Environment	-

### **Acronyms**

<i>ACTE</i>	Company name	-
<i>CSP</i>	Concentrated solar power	-
<i>DNI</i>	Direct normal irradiance	-
<i>IC</i>	Internal combustion	-
<i>LPG</i>	Liquified petroleum gas	-
<i>NTU</i>	Number of transfer units	-
<i>RC</i>	Remote control	-
<i>RSAB</i>	Rekuperator Svenska AB (Company name)	-
<i>STBC</i>	Solar thermal Brayton cycle	-
<i>TERS</i>	Thermal energy recovery system	-
<i>TIG</i>	Tungsten inert gas	-
<i>UAV</i>	Unmanned aerial vehicle	-

# 1 INTRODUCTION

---

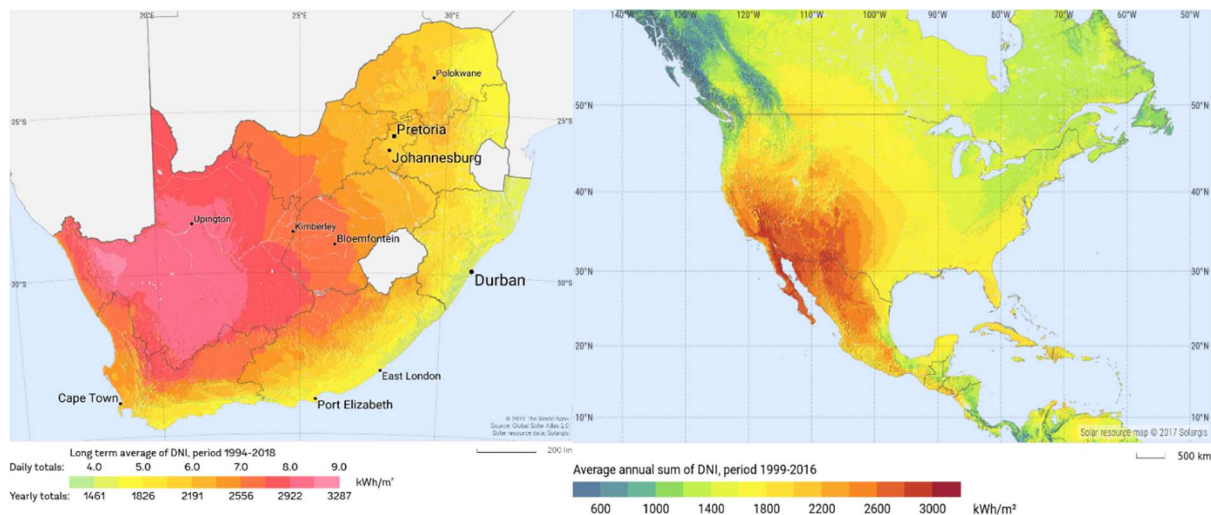
## 1.1 Background

South Africa is an astonishingly beautiful country filled with diversity, in both its cultures and techno-economic requirements. Although South Africa can be considered a modern and developed country, a vast percentage of the population still do not have access to electricity. Having access to electricity leads to opportunity in this day and age. It is the light by which children study, the catalyst which allows a dream to be transformed into a business. Electricity enables families to meet their most basic needs, and it is the connection that is needed to plug Africa into the grid of the global economy.

South Africa's electricity woes are partly due to the need to distribute electricity across the country to reach small communities, where it is often too costly for the distribution network to connect a rural community to the power grid. In addition to this, the national electricity provider has faced issues of mismanagement, poor planning, cable theft and aging coal power plants, which have caused frequent rolling blackouts. These blackouts have a detrimental effect on the economy, both for the large industrial and commercial sectors as well as for small businesses. According to Schoeman and Saunders (2018), more than two-thirds of the businesses in Johannesburg have stated that they experience, on average, between one and three power outages per month, while 18.5% have stated that they experience between four and seven power outages per month. Not only do power outages increase business expenses, but 42.6% of those businesses have also recorded a reduction in income on days with power outages. Couple this to an already saturated employment sector, with a youth unemployment rate of 39.6% (Department of Statistics South Africa, 2019), and it is evident that the requirement for emerging technologies to burgeon industrial growth is sorely needed so that the majority of South Africa's citizens may have a chance to gain skills-based knowledge, find employment and lift themselves out of poverty.

Additionally, the state of climate change has recently been at the forefront of concern within the scientific, economic, geo-political and humanitarian landscapes. As a result, there is a significant call for renewable energy utilisation. One of the biggest potential contributors to possible renewable solutions is that of solar energy. This is especially prevalent within a South

African context where a combination of demand for national and off-grid energy sources is high, large areas of open land are available and significant solar energy is accessible. Currently, more than 77% of South Africa's primary energy requirements are provided by coal (Department of Energy South Africa, 2019). One need only compare the direct normal irradiance (DNI) distribution map of South Africa with that of North America, displayed in Figure 1, to understand the enormous untapped potential that is represented by the available solar resource (Solargis, 2019).



**Figure 1 Direct normal irradiance (DNI) distribution map of South Africa (left) and North America (right) (Solargis, 2019).**

McDonald and Rodgers (2002) state that personal micro-turbine power generation systems may be as commonplace in the future as owning a personal computer. They suggest that a compact, gas-fired, silent-running personal micro-turbine with very low emissions would operate unattended and would be essentially maintenance-free, resulting in generator sets having the potential to become standard items in new homes in coming decades. When one considers that these micro-turbines can be designed to operate on a wide variety of fuels, with infrequent service intervals as well as the ability to utilise solar energy as heat source, it quickly becomes clear that micro-turbines are an attractive solution. One proposed solution is small, modular micro-turbine power plants which can generate electricity and hot water for any household or small community using concentrated solar power and gas (Le Roux, 2018). The creation of an industrial sector aimed at producing such micro-turbine solutions for the South African market would allow for a large amount of skills-based job creation, boosting the economy and simultaneously improving the quality of life for many South Africans.



## 1.2 Current technologies

Internationally there have been developments in micro-turbine technologies, with off-the-shelf solutions now being available. Various companies have gone about addressing the interest in micro-turbine technology from numerous angles. For example, Jakadofsky Jet Engines (Jakadofsky, 2019), Capstone Turbine Corporation (Capstone, 2019) and Bladon Jets (Bladon, 2019) have all chosen to manufacture units which solely produce electricity, with their JetVolt, C30 and MTG units respectively. On the other hand, MTT's EnerTwin Micro-CHP (MTT, 2019) and Samad Power's proposed TwinGen (Samad Power Ltd, 2019) and Turbo Green Boiler (Samad Power Ltd, 2019) models produce both electrical and thermal energy in the form of water heating. Figure 2 compares the Capstone and MTT units to scale. Table 1 contains a comparison between the various micro-turbine solutions from the aforementioned companies.



*Figure 2 Capstone C30 (left) and MTT EnerTwin Micro-CHP (right) micro-turbines (Capstone (2019); MTT (2019)).*

The specifications listed in Table 1 reveal that there are many micro-turbine products which cater to varying requirements. What all the aforementioned products, excluding the Jakadofsky JetVolt, have in common is that they utilise a recuperator to improve the thermal efficiency of the unit, thus greatly reducing the fuel consumption. This is important considering that for these systems to be economically viable, the running costs need to be kept as low as possible.

<b>Company</b>	<b>Model</b>	<b>Power output</b>	<b>Fuel consumption</b>	<b>Fuel type(s)</b>	<b>Service intervals</b>
<b>Jakadofsky</b> (2019)	JetVolt	8 kW	10 L/hour (kerosene)	Diesel, petrol, kerosene	-
<b>Capstone</b> (2019)	C30	30 kW	9.6 m <sup>3</sup> /hour (natural gas)	Natural gas, liquid fuels, propane, biogas	-
<b>Bladon</b> (2019)	MTG	12 kW	4.9 L/hour (kerosene)	Diesel, petrol, kerosene	8000 hours
<b>MTT</b> (2019)	Micro-CHP	3.2 kW electric 15.6 kW thermal	1.87 m <sup>3</sup> /hour (natural gas)	Natural gas, hydrogen	5000 hours
<b>Samad Power</b> (2019)	TwinGen (proposed)	2 kW electric 10 kW thermal	12.65 kW	Natural gas	6000 hours
	Turbo Green (proposed)	3 kW electric 17 kW thermal	21 kW		5000 hours

*Table 1 Comparison of various available and proposed micro-turbine solutions.*

However, the JetVolt was optimised to be lightweight and ergonomic, which is advantageous for mobile applications. The issue with the necessity for a recuperator is that, according to McDonald (2000), a recuperator represents up to 30 % of the capital cost of a micro-turbine package.

### **1.3 Problem statement**

Due to a combination of South Africa's geographic location, economic standing in the global perspective and current technological requirements, it is either not possible or too expensive to acquire any of the off-the-shelf micro-turbine solutions. Additionally, none of the available

micro-turbine solutions currently offer a solar-powered option, which would be highly valuable in the South African small-scale power generation market (less than 20 kW). Thus, it is necessary to develop such a technology locally. As previously stated, the recuperator within such a system is vital, but it also contributes significantly to the expense. Moreover, the recuperator poses a similar issue to the turn-key micro-turbine solutions insofar as they are not found locally, thus they either cannot be acquired or are too costly. This is also the case when local manufacturing is considered. Due to the technologies required, such as furnace brazing, laser welding and metal 3-D printing, not being well established in South Africa, it is either uneconomic or not possible as a whole to locally manufacture a recuperator.

#### **1.4 Research objective**

Considering the aforementioned challenges, the research carried out in this work was aimed at investigating a possible recuperator design which utilises a sodium silicate-based sealant as well as a clamped plate-style construction. The novelty of the design stems from the objective to locally manufacture the recuperator using readily available materials and methods. Not only would this present an effective solution to the need for a solar-powered recuperated personal micro-turbine, but it could also create employment opportunities and stimulate the economy of South Africa.

#### **1.5 Thesis overview**

The following thesis contains a literature review in Chapter 2, which contains an in-depth review of the knowledge base necessary to understand Brayton cycles, micro-turbine technology, solar thermal Brayton cycles and recuperators. Thereafter, the methodology implemented to accurately model a clamped plate-style recuperator is explored in Chapter 3. The themes addressed are: the overall layout of the recuperator, the heat transfer mechanisms, how heat loss and pressure loss was accounted for, as well as the mechanical stresses experienced by the plates. Two separate experiments with different recuperators were conducted so that a range of data for differing geometries and fluid conditions could be acquired. Chapter 4 details the differences between the two test rigs utilised during experimentation as well as the means by which the data was gathered. Chapter 5 contains the results gathered from extensive experimental testing performed utilising the two test rigs that

were constructed. Test 1 and 2 were carried out for the Mark I and Mark II recuperators respectively, and the data was analysed to determine their performance. This was achieved by examining the temperature measurements, mass flow rate readings, pressure loss characteristics and heat loss. Once the data from each test was analysed, the results were compared to the results generated by the theoretical model to ascertain whether it models the recuperator's performance accurately. After analysis of the experimental data, the validated model was used to examine whether the proposed recuperator design could be applied to a small-scale solar thermal Brayton cycle. To explore this possibility, various geometries and recuperator configurations were modelled in Chapter 6. Chapter 7 encompasses a summary of the findings throughout the thesis, the conclusions that were drawn from these findings, as well as recommendations that the author proposes be investigated for future work. The appendices consist of a specification sheet, calibration certificates, and an error analysis.

## 2 LITERATURE STUDY

### 2.1 Introduction

This chapter contains an in-depth review of the knowledge base necessary to understand Brayton cycles, micro-turbine technology, solar thermal Brayton cycles and recuperators. The methodology employed in the remainder of the report is based on the literature study which shows that a clamped plate-style recuperator could be a viable solution for waste heat recovery in a Brayton cycle.

### 2.2 Brayton cycle

Invented by and named after George Brayton, the Brayton cycle is a relatively simple process. First one can consider the ideal Brayton cycle, which can be summarised as follows: air is pressurised by a compressor isentropically (constant entropy); fuel is added to the air and combusted, heating it isobarically (constant pressure); the air-fuel mixture is then expanded and work extracted isentropically; and lastly, the leftover gas is expelled isobarically to the atmosphere. A more realistic Brayton cycle operates as follows: adiabatic (no heat loss) compression, isobaric combustion, adiabatic expansion, and isobaric heat rejection (Weston, 2000). The compressor and turbine within a jet engine are of an axial flow design, meaning the air (and air-fuel mix through the turbine) flows parallel to the shaft.

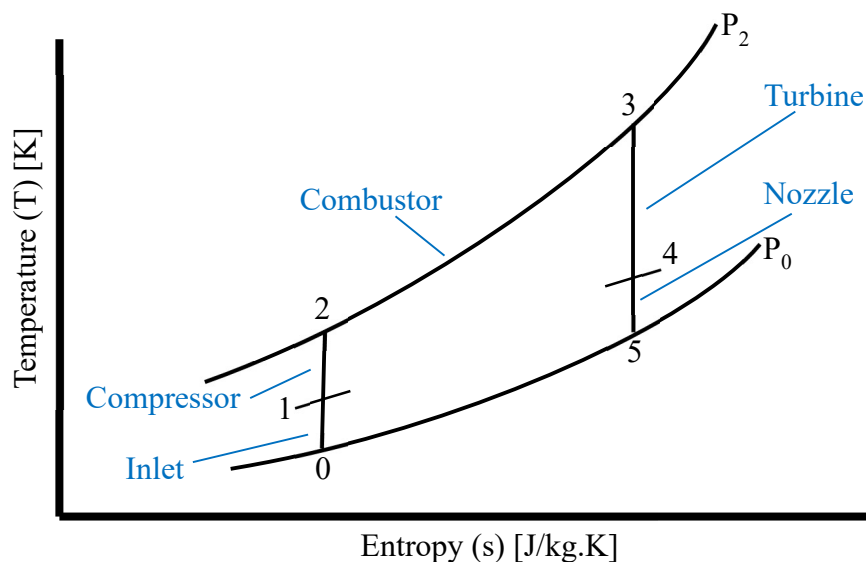
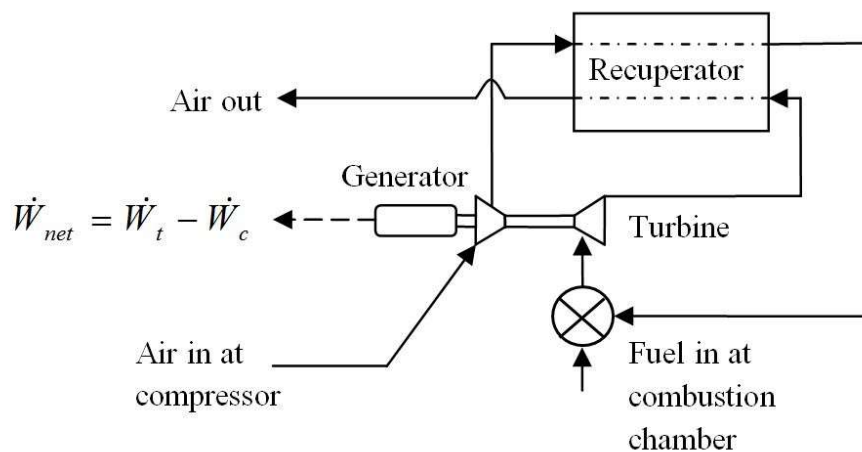


Figure 3 Temperature-entropy diagram of an ideal turbo-jet engine.

Figure 3 demonstrates how all the components work together to perform their specific functions in a turbo-jet engine. A turbo-jet engine usually consists of multiple stages (rows) of blades that gradually compress or expand the gases as they travel through. The turbines used in a Brayton cycle for power generation differ since the power produced is extracted by coupling a generator to the shaft of the turbine instead of using the raw power (thrust) of the exhausted gases coming from the nozzle. This means that turbo-jet engines designed for aircraft are not suitable for power generation purposes as the intake is designed to accept air travelling in at high velocities. The exhaust is designed to vector the thrust, hence the nozzle, and the turbine stage of the jet engine is small due to the fact that it only has to power the compressor. However, with a gas turbine for power generation, the air intake cowl is designed to allow air to be 'sucked' in whilst stationary. There are typically more turbine stages to provide more shaft power than thrust power, and the exhaust nozzle is replaced so that it does not increase velocity but instead directs the used gases off at an angle. Considering that the standard gas turbine cycle expels a large amount of residual heat energy from the exhaust, if one were to somehow utilise that wasted heat energy, the efficiency could be drastically improved. A recuperated Brayton cycle accomplishes exactly this via the implementation of a heat exchanger known as a recuperator. The specifics of a recuperator are detailed in Section 2.5. Xiao et al. (2017) state that the addition of a recuperator can improve the overall cycle efficiency by up to 30%.

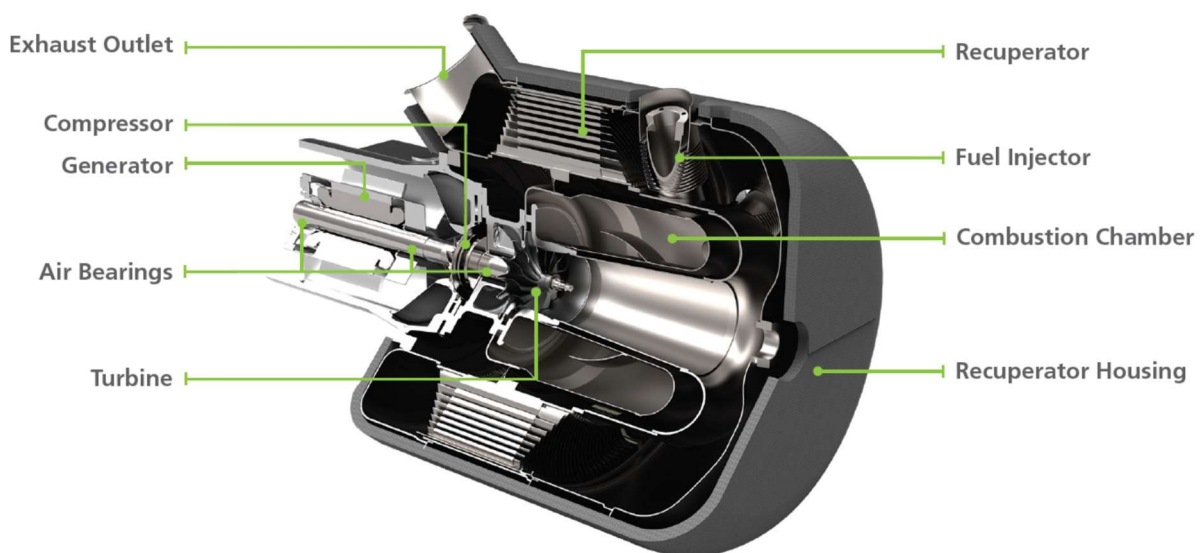


**Figure 4** *Recuperated gas turbine Brayton cycle.*

A representation of a recuperated Brayton cycle is shown in Figure 4. For a solar thermal Brayton cycle (STBC), the heat input of the combustor (see Figure 4) is substituted by the heat input of a solar receiver (see Section 2.4).

### 2.3 Micro-turbines

Micro-turbines can vary from 25 kW to 500 kW in output capacity, with an efficiency of 20 to 30% (Cadorin, et al., 2012). They are able to run on natural gas, hydrogen, propane or diesel, making them very versatile. Because of their ability to run on hydrogen, the most abundant element in the universe, it is potentially a very sustainable method of generating power since when hydrogen burns, the only waste product is water vapour. Micro-turbines have been purpose-built to produce torque and not thrust. The units are compact and manufactured with high-speed permanent magnet generators with which they can generate electricity, as shown in Figure 5 below (Capstone, 2019). Another advantage to this design is the integrated recuperator, which increases efficiency. There are, however, some challenges associated with micro-turbine implementation. Firstly, the capital cost to purchase and implement a micro-turbine ranges from \$ 700 to \$ 1100 per kW (Capehart, 2016). Thus, for an average South African residence which requires 3216 kWh of electrical energy per annum according to the World Energy Council (2016), equating to a 9 kW generator, it would cost between \$ 6300 and \$ 9900 to implement, and one would still have to incur the fuel, installation and maintenance costs.

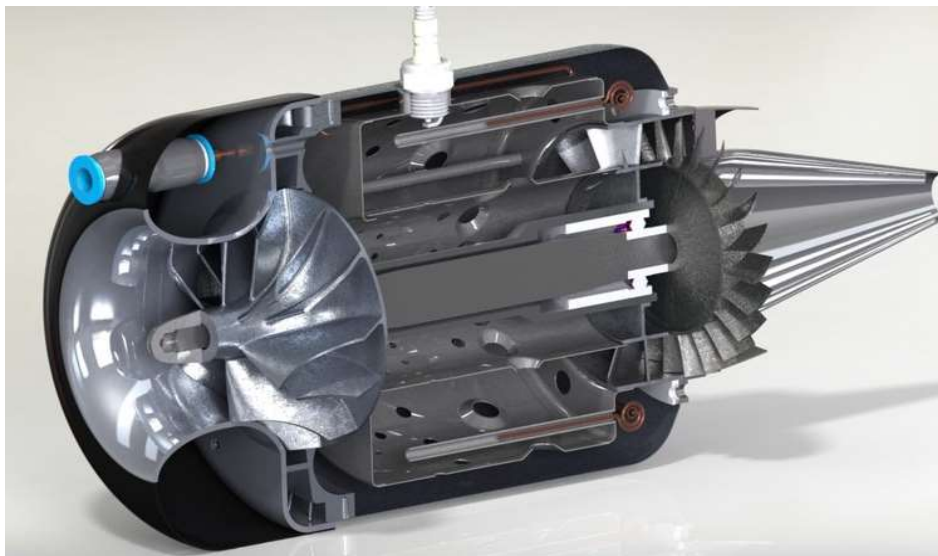


*Figure 5 Recuperated micro-turbine with integrated generator produced by Capstone (2019).*

Upon inspection of the design, the exit from the compressor and inlet to the turbine are at the centre of the device, making it complex to retrofit to an STBC. However, the micro-turbine core consists of a compressor and turbine which are available in small-scale commercial applications at competitive prices.

### **2.3.1 Remote control jet aeroplane and helicopter turbine engines**

One type of micro-turbine that has had extensive development and is widely produced is that of a small turbo-jet engine used for remote control (RC) jet aeroplanes. They have a high power-to-weight ratio; however, they were designed to be used in flight and produce thrust (not torque) due to the small turbine stage relative to the compressor, visible in Figure 6 (Mirshahidi, 2012). Additionally, considering this design, it would be difficult to accommodate the solar thermal input. Thus, an RC aeroplane jet engine would not be an attractive solution. Helicopter RC turbo-shaft engines could be easier to modify since they have two turbines, where one turbine is connected to the rotor via a gearbox; however, the lifetime of the gearbox is only 25 hours (Heli-Factory, 2013).

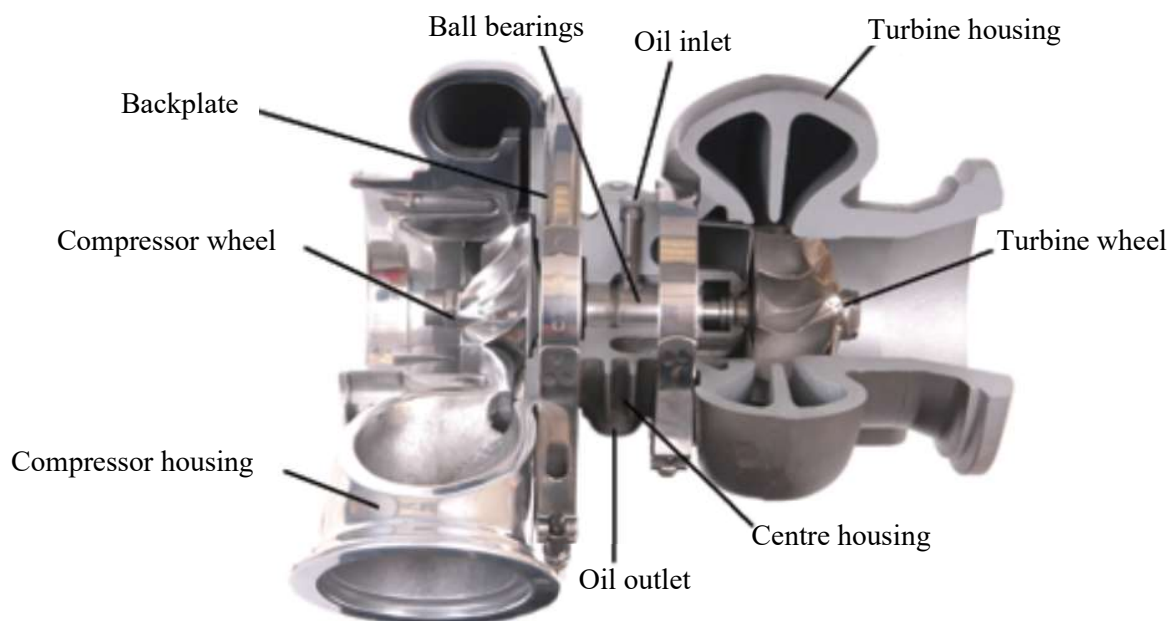


*Figure 6 RC micro-jet engine (Mirshahidi, 2012).*



### 2.3.2 Turbochargers and future outlook

Despite the lack of affordable or readily available micro-turbine options, a possible solution is to use a turbocharger. Invented by Swiss engineer Alfred Büchi in 1925 (BorgWarner, 2016), its basic function is to utilise the energy in expelled exhaust gases from an internal combustion (IC) engine to compress the intake air fed into the engine. The exhaust gases pass through the exhaust housing of the turbo and are further expanded by the turbine wheel, just as they are in a gas turbine engine. However, in this case, it is not an axial turbine, but instead the gases enter radially and exit axially, represented in Figure 7 below (Garrett, 2009). Just like a jet engine, the turbine wheel is linked to the compressor wheel via a shaft. Thus, if the turbine is spun, so is the compressor. Therefore, one can deduce that by simply linking the outlet of the compressor and the inlet of the turbine by a device that inputs heat, such as a combustion chamber or solar receiver, a Brayton cycle can be created. Turbochargers have been under development for almost 100 years, resulting in a refined technology. Turbochargers have been made remarkably efficient as well as robust and are able to have high pressure ratios over a single radial compressor or turbine stage. The performance characteristics of turbochargers can be altered to suit the application by changing impeller geometries, or pairing various compressor and turbine wheels with one another.



*Figure 7 Turbocharger schematic model (Garrett, 2009).*

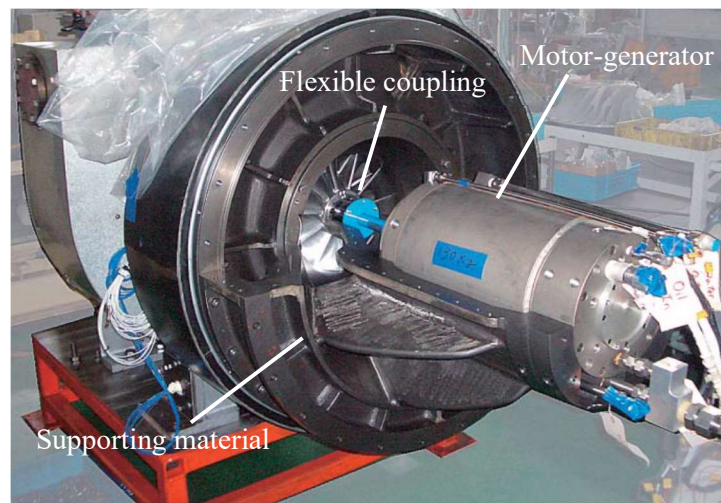
Additionally, turbochargers are readily available at a relatively low cost (in comparison to purpose-built micro-turbines), starting from R 3000 for smaller units to R 30 000 for bigger turbochargers (Turbo Direct, 2019). Another option, still fully in the prototype stage, is to utilise pre-built turbochargers that have electric motors or stators built into them. Firstly, there is a turbocharger that is electrically assisted under development by G+L Innotec (G+L Innotec, 2014). Their design is meant to decrease emissions of vehicles by electrically spooling the turbocharger in the lower rpm ranges of an automobile IC engine, where it operates inefficiently. Due to the electric motor already being coupled to the turbocharger, it could be slightly modified to instead produce power from the rotation of the shaft. The next candidate comes from Magneti Marelli. Their design entails a turbocharger which has a TERS (thermal energy recovery system) motor-generator situated between the compressor and turbine housings interacting with the shaft, as shown in Figure 8 (Formula 1 Dictionary, 2014). This system was developed for Formula 1 Grand Prix cars to extract more energy from the exhaust gases being expelled from the engine, and to rapidly increase the shaft speed for instantaneous power delivery.



***Figure 8 Magneti Marelli TERS turbocharger (Formula 1 Dictionary, 2014).***

Another potential solution results in the turbine and compressor stages being separated from each other. The compressor is powered by an electric motor, while the turbine drives an electric generator (Aeristech, 2015). This allows the turbine and compressor to rotate at different

speeds, yielding better efficiency for each component. The company in question, Aeristech, are still in the developmental phase.



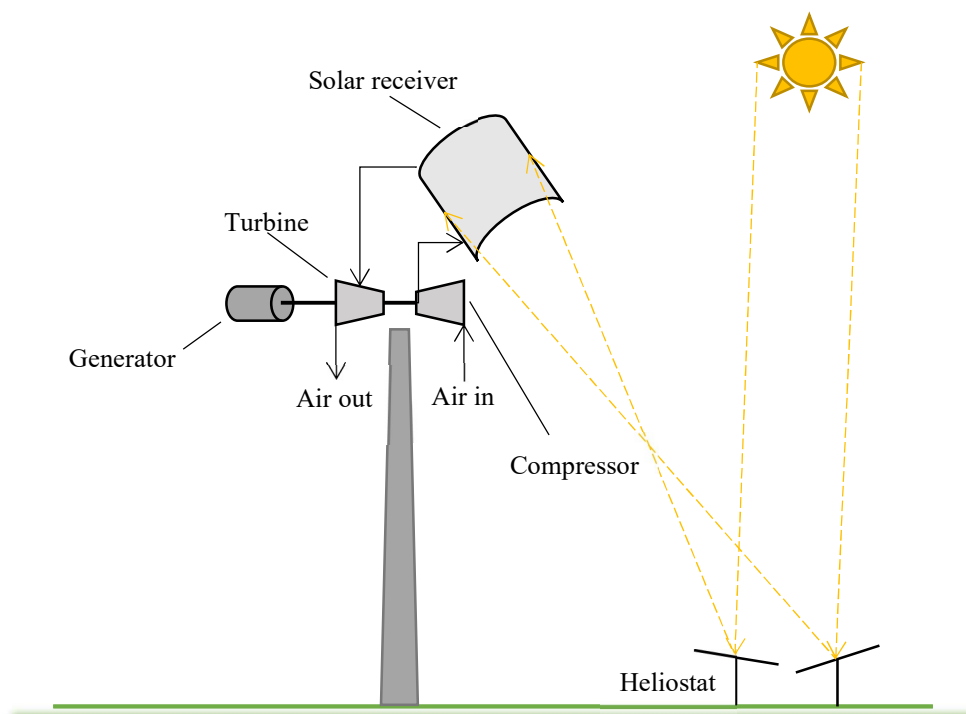
*Figure 9 Hybrid turbocharger with flexible coupling (Shiraishi & Ono, 2007).*

Visser et al. (2011) also researched coupling turbochargers to electric generators for the MTT EnerTwin Micro-CHP project, having demonstrated 2.7 kWe power output at 12.3% electrical efficiency. Finally, along similar lines, another option may be a two-shaft arrangement where one turbocharger solely produces the hot gases to be expanded further by a second, larger turbine (without a compressor) that then rotates at a lower speed and is coupled to an alternator (a power turbine) whilst the first turbocharger's turbine only provides power to the compressor (a gas generator). To aid in coupling a turbocharger to an alternator, the idea of utilising a flexible coupling, which would reduce the need for a perfectly balanced and aligned shaft system, was proposed by Shiraishi and Ono (2007) at Mitsubishi Heavy Industries, pictured in Figure 9. The author suspects that the development and commercialisation of electrically-assisted turbochargers as well as micro-turbine range extenders for electric vehicles will decrease the costs of these units in the future.

#### **2.4 Solar thermal Brayton cycle**

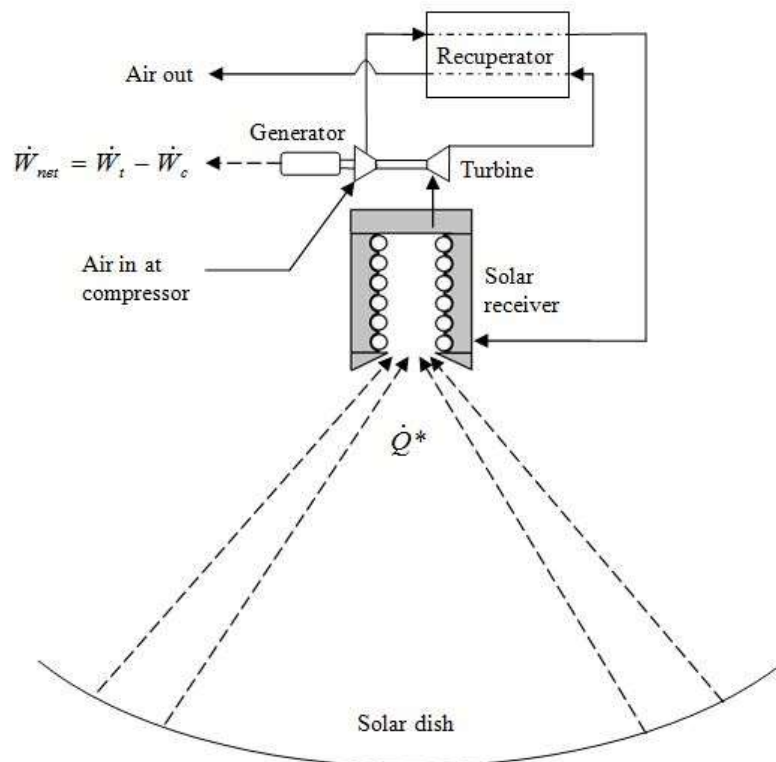
Concentrating solar power (CSP) utilises the direct normal irradiance (DNI) from the sun to create thermal energy that can then be used in processes to accomplish work and, if needed, generate electricity. One form of CSP system is a central receiver design whereby a large array of heliostats (reflective mirrors) focus the DNI to a receiver. The receiver is essentially an

insulated heat exchanger which transfers the solar thermal energy to a separate working fluid such as air. The highly concentrated solar flux can then be used as the heat source for a power cycle such as the Brayton cycle, assimilating the role of a combustion chamber, creating what is referred to as a solar thermal Brayton cycle (STBC). The compressed and heated air is then expanded through a turbine, as in a Brayton cycle, and from this shaft work is produced which can be utilised to generate electricity. Ssebabi et al. (2019) found that a solar-hybrid two-shaft micro-turbine system can shift the equilibrium running conditions to a more favourable operating point, essentially resulting in the hybridised system being more efficient than the non-hybridised counterpart in addition to it utilising the free solar resource. An STBC is attractive when considering smaller-scale applications due to the lower costs (Mills, 2004), high reliability (Pietsch & Brandes, 1989), added simplicity and reduced water-consuming nature, especially within a southern African context, since the STBC generally uses air as a working fluid. The STBC has been shown to operate at solar to electric efficiencies of 11.76% (Dickey, 2011) to thermal efficiencies beyond 30% (Stevens, et al., 2004) whilst maintaining achievable turbine inlet temperatures in the region of 760 °C to 871 °C (Pietsch & Brandes, 1989).



***Figure 10 Standard solar thermal Brayton plant.***

A representation of the Solugas cycle (Korzynietz, et al., 2016) is depicted in Figure 10. In place of large flat heliostats situated in a field focussing towards a central tower that move and 'track' the sun, a miniaturised solar Brayton cycle is comprised of a solar dish reflector mounted on the same frame to which the receiver is mounted (Wang, et al., 2015). This allows for a more compact package that could possibly be implemented commercially for small-scale power generation. Figure 11 shows a cycle diagram for the small-scale dish-mounted open STBC optimised by Le Roux (2015) using the method of entropy generation minimisation. Modelling of the cycle, fitted with a recuperator to make use of the exhaust heat and improve the cycle efficiency, has been performed by Le Roux & Meyer (2015). The cycle is considered to be small-scale due to it having a proposed output in the 1 kW - 20 kW range (Shah, 2005). The prototype would generate mechanical power by reflecting solar irradiance with a 4.8 m reflective dish into an open cavity tubular receiver, at solar to mechanical efficiencies ranging from 10% to 20%, which leaves room for large improvements (Le Roux & Meyer, 2015).



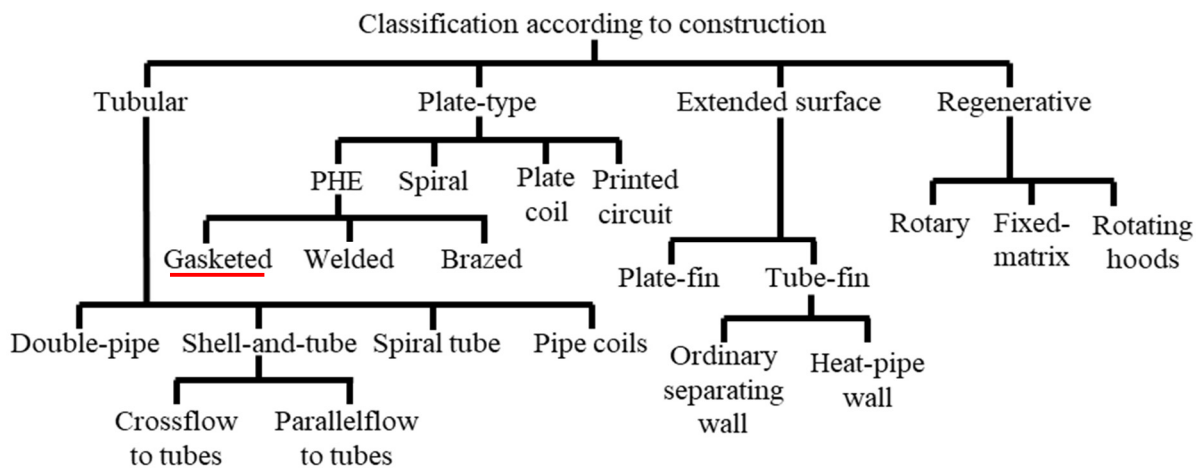
**Figure 11 The small-scale dish-mounted open STBC (Le Roux & Meyer, 2017).**

Lanchi et al. (2015) also researched a similar cycle as part of the OMSoP project, which saw the implementation of a dish-mounted STBC. The small-scale STBC could also be hybridised to use combustion as an additional heat source when the solar resource is sparse or not

available, i.e. at night. Alternatively, thermal storage systems such as packed rock bed (Allen, 2010) and lithium fluoride (Cameron, et al., 1972) storage may also be added to the cycle. Le Roux & Sciacovelli (2019) also postulate molten aluminium to be an effective thermal storage medium which could be employed within the solar receiver to ensure that a constant turbine inlet temperature is realised. Additionally, the excess heat given off at the exhaust of the cycle can be captured for water heating (Le Roux, 2018), absorption chilling or desalination (water purification). The purpose of the small-scale STBC would be to provide a mobile, off-grid source of electricity to communities in water-scarce areas that are in need of such resources.

## 2.5 Recuperators

A component which is instrumental in the small-scale STBC's success is the recuperator, which is essentially a high-temperature (operating temperatures above 650 °C (Aquaro & Pieve, 2007)) heat exchanger that utilises the left-over heat emitted from the outlet of the turbine and transfers it to the cool air coming from the compressor before going into the open cavity solar receiver. The recuperator allows for less external heat input (fuel or solar irradiance) in addition to lowering the required pressure ratios (typically three to four times lower) (Shah, 2005).



**Figure 12 Classification of heat exchangers (Shah, 1981).**

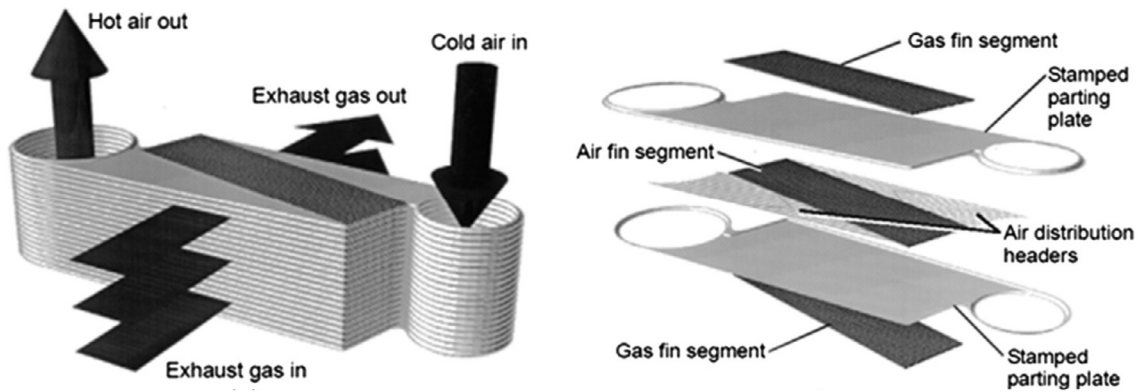
In order for the STBC to operate at moderate to high efficiencies with the implementation of a turbocharger, the recuperator shown in Figure 11 is key since the turbocharger runs optimally at lower pressure ratios. Furthermore, the recuperator allows for a less complex solar receiver (Le Roux, et al., 2013). Heat exchangers, and by extension recuperators, can be configured in

many different ways. Each layout has unique attributes which can be beneficial depending on the application. Figure 12 details the multitude of categories under which heat exchangers can be classified (Shah, 1981). Xiao et al. (2017) state that the main heat exchanger categories which encompass recuperators are tubular, plate-type (also known as primary-surface recuperators), and plate-fin, which falls under the extended surface category. However, plate-type and plate-fin recuperators are the most widely implemented due to their ability to achieve high effectiveness values and low pressure losses as well as remaining compact. Table 2, extracted from Xiao et al. (2017), compares various typical recuperator solutions that manufacturers have provided.

<b>Organisation</b>	<b>Recuperator type</b>	<b>Pressure ratio</b>	<b>Total pressure loss [%]</b>	<b>Cold-side effectiveness [%]</b>
<b>Turbec (Manufactured by Ansaldo Energia, Italy)</b>	Primary-surface	4.5	4.8	88.9-93.1
<b>Tokyo Institute of Technology</b>	Plate-offset-strip-fin	3	6.3	80
		4	7.8	80
<b>RSAB</b>	Primary-surface	<4.5	<4.5	>89
<b>Ingersoll-Rand</b>	Primary-surface	>3	5	90
<b>Capstone</b>	Primary-surface	2.7-4.2	<2.5	90
<b>Chang Gung University</b>	Swiss-roll	2.77	10-30	60-85
<b>Rolls-Royce</b>	Primary-surface	>6	-	92
<b>ACTE</b>	Primary-surface	-	-	90

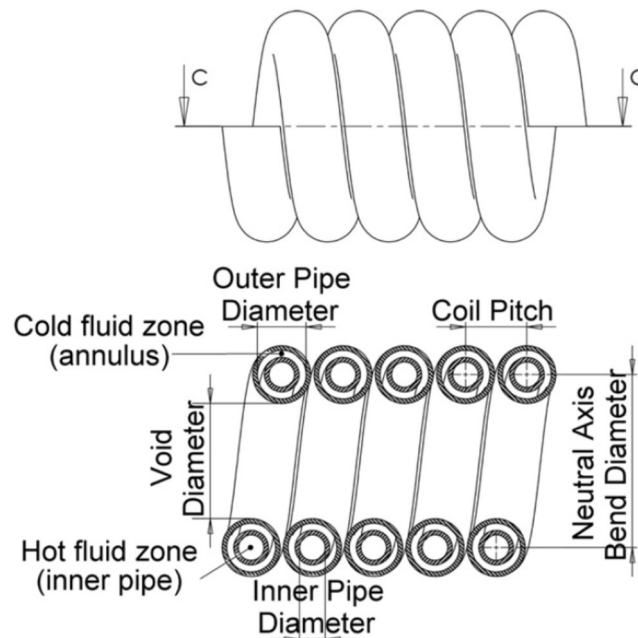
*Table 2 Typical existing recuperator solutions, extracted from Xiao et al. (2017).*

What is noteworthy from this information is firstly the performance characteristics of these recuperators. Typically, pressure loss values of between 5% and 10% were observed whilst an effectiveness of between 80% and 90% can be expected. The issue with the recuperator designs listed in Table 2 is that the manufacturing methods involved are complex, scarce and expensive due to the necessity for processes such as furnace brazing, laser welding and metallic 3D printing. An example of a recuperator from Table 2 is the primary-surface recuperator developed by Ingersoll-Rand, which is shown in Figure 13 (Kesseli, et al., 2003). The body is constructed from plates and gaskets which are stacked; however, the body is then furnace brazed together to form a seal.



**Figure 13 Ingersoll-Rand's plate-fin recuperator (Kesseli, et al., 2003).**

Clay & Tansley (2011) developed and analysed a simpler recuperator which falls under the tubular heat exchanger category, pictured in Figure 14.



**Figure 14 Section view of coiled pipe-in-pipe heat exchanger (Clay & Tansley, 2011).**

The design managed an adequate effectiveness of 76% although this came at the cost of a pressure loss in the region of 15%. Thus, although the simple design allows for a low-cost solution, the performance is heavily affected. Furthermore, Cordova et al. (2015) proposed a more complex radial configuration recuperator for oil-free turbogenerators, which could achieve an effectiveness of over 90%. In alignment with the findings of Xiao et al. (2017) represented in Table 2, for recuperators within a Brayton cycle specifically, McDonald (see Table 3) lists the typical criteria a recuperator must adhere to in order for it to function well



within the cycle (McDonald, 2000). From the criteria listed, it is shown that other heat exchanger types such as cross-flow types would not be suitable due to the high effectiveness and compact size required. Therefore, a counter-flow arrangement is necessary; more specifically, one approaching a plate-style configuration.

<b>Major design criteria</b>	Low heat exchanger cost High recuperator reliability
<b>Performance</b>	High recuperator cold-side effectiveness (> 90%) Low total pressure loss (< 5%)
<b>Fabrication</b>	Adaptable to high volume production methods (continuous/automated fabrication) Simple sealing (eliminate need for furnace brazing)
<b>Type of construction</b>	Compact and light weight matrix Integral manifolds/headers
<b>Cost</b>	No basic material wastage (zero scrap) Minimum (or zero) labour effort Unit cost goal not to exceed 1.5 times material cost

**Table 3 Listing the ideal micro-Brayton cycle recuperator characteristics (McDonald, 2000).**

Although McDonald (2003) suggests the use of plate-fin type counter-flow recuperators to maximise the compactness, Scaccia and Theoclitus (1980) posit that fins should be avoided within a Brayton recuperator. This is due to the increased likelihood of fouling, which would reduce the effectiveness to below that of a standard plate-style arrangement, as well as the negligible effect of fins in such a recuperator relative to the expenses (cost, weight) when considering the low velocity of the heat transfer fluid stream. One of the main aspects regarding the performance and reliability of a recuperator within an STBC would be the high temperatures of operation. Standard materials such as baseline commercial steels are limited by their thermal expansion, creep and fatigue limits at lower temperatures than what will be necessary. Super-alloys such as Inconel (McDonald, 2003) or even Elkonite 2050C, according to Van Greuning (2006), would have to be used to achieve a suitable service lifespan, although it is known that the ultimate goal would be the use of ceramics to attain the high cycle

temperatures necessary for efficiencies exceeding 30-40% (McDonald, 2003). Table 4 categorises and lists the main potential materials which could be used for high-temperature recuperator applications as well as the material properties (Ohadi & Buckley, 2001). Ohadi & Buckley (2001) stated that the joints of a metallic-alloy recuperator would be weak due to thermal expansion. For ceramic oxides fabrication is very expensive and the associated technology is proprietary, while carbon-carbon and carbon-SiC composites have short life-times but are comparatively less expensive (Ohadi & Buckley, 2001). Vick (2012) also suggests that a light-weight ceramic recuperator may be a solution in a small turboshaft engine for UAV propulsion, having achieved effectiveness values in the 84-87% range.

<b>High-temperature material or fabrication technology</b>	<b>Metallic Ni alloys (Inconel 718)</b>	<b>Ceramic oxides</b>	<b>Carbon-carbon composite</b>	<b>Carbon fibre-SiC composite</b>
<b>Temperature range</b>	1200-1250 °C	1500-2500 °C	3300 °C (inert environment) 1400-1650 °C (with SiC layer)	1400-1650 °C
<b>Tensile strength</b>	800-1360 MPa	48-2000 MPa	33 MPa (Bulk modulus)	1400-4500 Mpa
<b>Tensile modulus</b>	50 GPa	140-600 GPa	4.8 GPa	140-720 MPa
<b>Strength</b>	Adequate	Not adequate	Poor	Highest

***Table 4 Properties of commonly used high-temperature recuperator materials (Ohadi & Buckley, 2001).***

However, Le Roux and Sciacovelli (2019) have shown that lower receiver operating temperatures in the STBC have an advantage in terms of cost since for recuperator inlet temperatures of less than 670 °C, stainless steel materials can be used instead of super-alloys (Shah, 2005). Considering the aforementioned information regarding the capabilities of certain recuperator geometries as well as the relative cost associated with those designs, developing a recuperator that adheres to the criteria of McDonald (2000) whilst remaining cost-effective is a challenge. In this work, the utilisation of a gasketed, plate-type recuperator (underlined in Figure 12) is investigated. Gasketed plate-type heat exchangers are often used for lower temperature applications (Çengel & Ghajar, 2011) because the gasket material limits the operating temperature. However, a high-temperature sodium silicate-based sealant (Soudal,

2015) is available in South Africa for 170 R/L and can withstand temperatures of up to 1 500 °C. It is supplied in paste-form, in 310 ml cartridges, and was designed to be used for the sealing of joints and openings in high-temperature applications such as stoves, ovens and fireplaces.

## 2.6 Summary

In this chapter, the small-scale solar thermal Brayton cycle (STBC) with an estimated power output of 1 kW - 20 kW was considered because of its potential for hybridisation, the addition of thermal storage to extend operational time into the night, and the water-heating capability, which could prove useful for many South African citizens. In the field of micro-turbines, it was observed that there are a number of off-the-shelf micro-turbine solutions available such as remote-control aeroplane and helicopter engines. The issue with these solutions is the short lifetime as well as the difficulty associated with modifying the unit to work within a solar Brayton cycle. Turbochargers offer a developed technology that is available and cost-effective. However, a turbocharger would still need to be coupled to an electric generator to develop an STBC. In response to this issue, electrically assisted turbochargers appear to be an attractive solution, should the technology be developed further and made more commercially available. Recuperators, high-temperature (>650°C) heat exchangers, were investigated and it was noted that they allow for lower pressure ratios within a Brayton cycle. They are constructed in many different ways, with the primary-surface (plate-type) recuperator being the most widely implemented. These recuperators have demonstrated very good performance but require complex and expensive manufacturing techniques such as laser welding and metallic 3D printing, making them an infeasible product in a South African context. Criteria that a recuperator in a Brayton cycle should adhere to were also outlined, stipulating that a cold-side effectiveness of 90% or above and a total pressure loss of less than 5% are necessary. To uphold these requirements, it is suggested that a counterflow plate-style recuperator is mandatory. To combat complex manufacturing methods, a gasketed stacked-plate design was proposed. A sodium silicate-based sealant called Soudal Calofer is available in South Africa and can withstand the operating temperatures of an STBC.

### 3 THEORETICAL MODEL

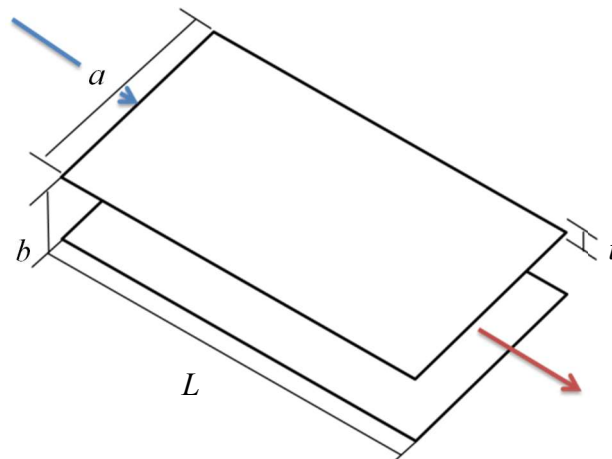
---

#### 3.1 Introduction

This chapter contains the methodology implemented to accurately model a clamped plate-style counterflow recuperator analytically at steady state. The themes addressed are the overall layout of the recuperator, the heat transfer mechanisms, how heat and pressure loss is accounted for, as well as the mechanical stresses experienced by the plates. The modelling of the steady-state performance of the recuperator allows for the analysis of the experimental results and to predict the effect that different recuperator geometries have on the effectiveness.

#### 3.2 Recuperator concept

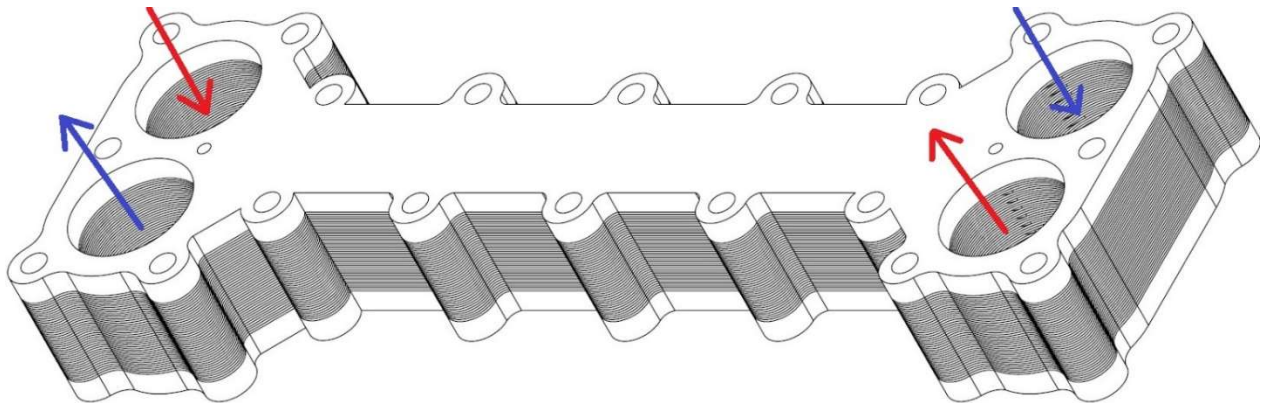
The effectiveness- $NTU$  method was employed to analyse and create a model of the proposed counterflow plate-style recuperator. Figure 15 shows the basic layout on which the calculations were based, whereby a single channel was considered for each fluid flow stream. Note that  $a$  is the channel width,  $b$  the channel height,  $L$  the channel length and  $t$  the plate thickness between channels.



*Figure 15 Basic plate heat exchanger layout.*

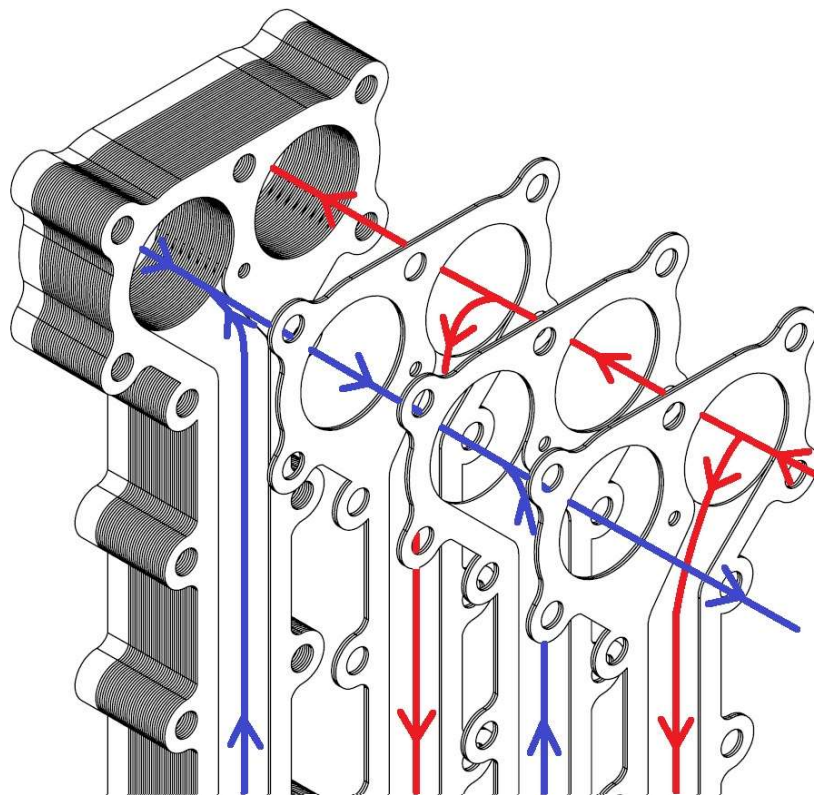
To continue with the development of a model that can predict the performance of a recuperator to be built and tested, a design had to be conceptualised. Figure 16 depicts a schematic of the plate-style counterflow recuperator design, which was generated iteratively with the

development of the theoretical model.



**Figure 16** *Plate-style counterflow recuperator concept.*

The proposed design is generated to fulfil the requirements outlined previously, with cost-effectiveness, ease of assembly and disassembly being the key concerns. Its construction relies on the repetition of alternating plates and gaskets, which can be laser cut from any metal sheet of the user's specification. Each plate is identical, and so is each gasket. The gaskets are then inverted for each placement to create separate hot and cold fluid flow paths.



**Figure 17** *Exploded view of the recuperator concept.*

The plate-gasket layers can then be stacked ad infinitum to generate a recuperator with the desired number of flow channels. Additionally, the thickness of the channel height,  $b$ , can be changed by selecting a metal sheet of the desired thickness. Once stacked to create a recuperator of the specified size, the ‘core’ can then be sandwiched between two thick plates and squeezed together via bolts around the periphery of the unit. To ensure that no leakage occurs, a unique high-temperature sodium silicate-based sealant made by Soudal called Calofer (Soudal, 2015) can be instituted between the plates and gaskets. This method was proposed due to the high cost of high-temperature gasket material as well as its lack of availability in Africa.

The odd ‘bone’ shape of the recuperator is a result of the need to keep the channel width narrow, in order to prevent excess stress in the plates at high temperatures due to the pressure difference between the hot and cold channels, while maintaining sufficiently large header tube diameters so as not to induce a significant pressure drop. Figure 17 details the layout of the gasket-plate arrangement by showing an exploded view of the recuperator. The alternating hot and cold channels can now be observed clearly, revealing how the fluid streams follow a counterflow path.

### 3.3 Heat transfer calculation

The main calculations are done by utilising Equations (1) and (2) to calculate the number of transfer units ( $NTU$ ), and subsequently the effectiveness (Çengel & Ghajar, 2011):

$$NTU = \frac{A_s}{C_{p,c} \dot{m}_{channel} \left[ \frac{2ab}{Nu(a+b)} \left( \frac{1}{k_c} + \frac{1}{k_h} \right) + R_{f,h} + R_{f,c} + \frac{t}{k_{steel}} \right]} \quad (1)$$

$$\varepsilon = \frac{1 - e^{-NTU(1-C_{rh})}}{1 - C_{rh} e^{-NTU(1-C_{rh})}} \quad (2)$$

Equation (1) is specific to the design because it is representative of a recuperator with channels operating within a laminar fully developed flow regime. Due to this operating state, the Nusselt number,  $Nu = 8.24$ , is constant for the specific channel geometry where  $a/b \gg 8$  (Çengel & Ghajar, 2011). This Nusselt number is slightly conservative because the average Nusselt number will be higher due to the developing flow region, which will enhance heat transfer

(Meyer & Everts, 2018) and because mixed convection will occur (Everts & Meyer, 2018). However, the increase is found to be so small, in the region of 1%, that it has a negligible effect on the performance of the recuperator. The fouling factor for the clean air on the cold-side is taken to be  $R_{f,c} = 0.0004 \text{ m}^2 \cdot \text{°C}/\text{W}$ , while  $R_{f,h} = 0.0006 \text{ m}^2 \cdot \text{°C}/\text{W}$  (Çengel & Ghajar, 2011) for the hot side due to the possible combustion of liquified petroleum gas (LPG), which only introduces a small amount of water vapour and  $\text{CO}_2$  when combusted stoichiometrically. The fouling factor for the hot side could be different for the experimental validation as a result of incomplete combustion leading to large soot deposits. The material conductivity of the initial test unit, Test 1, manufactured out of mild steel for cost-effectiveness, was taken as  $k_{\text{steel}} = 60 \text{ W}/\text{m} \cdot \text{°C}$  (Çengel & Ghajar, 2011), but stainless steel ( $k_{\text{SS}} = 15 \text{ W}/\text{m} \cdot \text{°C}$ ) would be the material of choice for further iterations, in Test 2, due to its corrosion and creep resistance.

### 3.4 Heat loss analysis

The heat loss analysis conducted for the recuperator design is based on Equations (1) and (2), where the adiabatic model produces one effectiveness value for the recuperator as a whole. The reality is that when heat loss is considered, the hot and cold-side effectiveness values will differ since the hot side can be considered more effective due to it losing more heat than what the cold side gains. To calculate the hot and cold-side effectiveness values for a counterflow heat exchanger with heat loss, Equations (3) to (11) are employed, adapted from Nellis & Pfotenhauer (2005):

$$\varepsilon_h = \begin{cases} 1 - \theta_{X=1}, & C_{rh} < 1 \\ C_{rh}(1 - \theta_{X=1}), & C_{rh} > 1 \end{cases} \quad (3)$$

$$\varepsilon_c = \begin{cases} (1 - \theta_{X=0})/C_{rh}, & C_{rh} < 1 \\ 1 - \theta_{X=0}, & C_{rh} > 1 \end{cases} \quad (4)$$

where the dimensionless temperature differences are:

$$\theta_{X=0} = \frac{B + (\chi_h + C_{rh}\chi_c)[1 - e^{NTU_h(C_{rh}-1)}]}{(C_{rh} - 1)[e^{NTU_h(C_{rh}-1)} - 1/C_{rh}]} \quad (5)$$

$$\theta_{X=1} = NTU_h(\chi_c + \chi_h) + \frac{(\theta_{X=0} - 1)}{C_{rh}} + 1 \quad (6)$$

with:

$$B = [NTU_h(\chi_c + \chi_h) + (C_{rh} - 1)/C_{rh}](C_{rh} - 1) \quad (7)$$

$$C_{rh} = C_{p,h}/C_{p,c} \quad (8)$$

$$NTU_h = \frac{UA}{\dot{m}_h C_{ph}} \quad (9)$$

and the dimensionless external heat losses are:

$$\chi_h = -\frac{\dot{Q}_{loss,h}}{UA(T_{h,i} - T_{c,i})} \quad (10)$$

$$\chi_c = -\frac{\dot{Q}_{loss,c}}{UA(T_{h,i} - T_{c,i})} \quad (11)$$

The heat loss rate from each hot side and each cold side of a recuperator channel pair is calculated by dividing the top and bottom heat loss values by the number of channels and adding the side heat loss per channel according to Le Roux et al. (2014), as follows:

$$\dot{Q}_{loss,h} = (\dot{Q}_{loss,top,h})/N + \dot{Q}_{loss,side,h} \quad (12)$$

$$\dot{Q}_{loss,c} = (\dot{Q}_{loss,btm,c})/N + \dot{Q}_{loss,side,c} \quad (13)$$

where:

$$\dot{Q}_{loss,top,h} = [(T_{h,i} + T_{h,o})/2 - T_{\infty}]/R_{top,h} \quad (14)$$

$$\dot{Q}_{loss,btm,c} = [(T_{c,i} + T_{c,o})/2 - T_{\infty}]/R_{btm,c} \quad (15)$$

$$\dot{Q}_{loss,side,h} = \frac{[(T_{h,i} + T_{h,o})/2 - T_{\infty}]}{R_{side,h}} \quad (16)$$



$$\dot{Q}_{loss,side,c} = \frac{[(T_{c,i} + T_{c,o})/2 - T_{\infty}]}{R_{side,c}} \quad (17)$$

and the thermal resistances are:

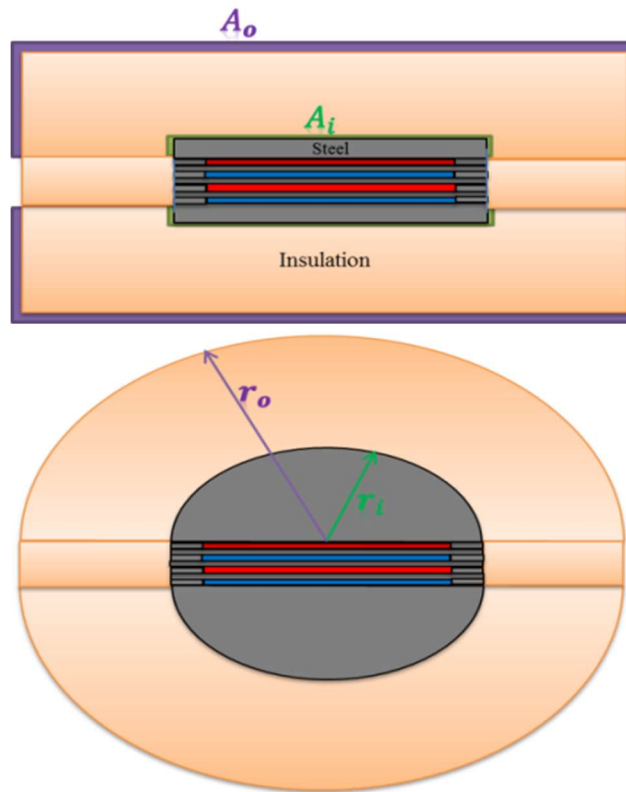
$$R_{top,h} = \frac{1}{h_{inr,h}aL} + \frac{\ln\left(\frac{r_o}{r_i}\right)}{\pi L k_{ins}} + \frac{1}{h_{outr}(a + 2t_{ins,side})L} \quad (18)$$

$$R_{btm,c} = \frac{1}{h_{inr,c}aL} + \frac{\ln\left(\frac{r_o}{r_i}\right)}{\pi L k_{ins}} + \frac{1}{h_{outr}(a + 2t_{ins,side})L} \quad (19)$$

$$R_{side,h} = \frac{1}{2h_{inr,h}bL} + \frac{t_{ins,side}}{2k_{ins}bL} + \frac{1}{2h_{outr}bL} \quad (20)$$

$$R_{side,c} = \frac{1}{2h_{inr,c}bL} + \frac{t_{ins,side}}{2k_{ins}bL} + \frac{1}{2h_{outr}bL} \quad (21)$$

The inner convective heat transfer coefficients,  $h_{inr,h}$  and  $h_{inr,c}$ , are calculated by considering laminar fully developed flow, resulting in a constant Nusselt number, for the same reasons stipulated in Section 3.3.  $k_{ins}$  is the thermal conductivity of the insulation material used to minimise heat loss from the recuperator body, and can be attained from the specification sheet provided by the manufacturer. Note that conduction through a plane wall is considered for the calculation of the thermal resistance of the recuperator side walls, as shown in Equations (20) and (21). For the calculation of the thermal resistance of the top and bottom surfaces of the recuperator, conduction through a cylindrical layer is assumed, as shown in Equations (18) and (19) as well as Figure 18. At the top of Figure 18, a representation of a cross-sectional view of the insulated recuperator is shown. Note that the top and bottom insulation is not only confined to the surface of the recuperator, but rather that it ‘fans’ outward. This leads to the outer surface of the insulation being larger than the outer surface of the recuperator. Therefore, to model the heat losses more accurately, conduction through a cylindrical layer is assumed. The top and bottom surfaces were thus modelled as cylindrical walls where the outer and inner surface areas of the insulation was kept constant and used to calculate effective radii to represent a cylinder. Figure 18 (bottom) provides an exaggerated example of what this looks like. However, note that the steel ‘grey part’ is not actually any thicker than it is in the top diagram.



**Figure 18 Actual recuperator cross section (top) and heat loss analysis recuperator cross section (bottom).**

Besides the obvious values such as the insulation thickness, the convection heat transfer coefficient on the outside surface of the insulation ( $h_{out}$ ) is also important. Natural convection was assumed for calculation of this value for each surface since the experimental testing would be conducted indoors. The last components of heat loss to be considered in the model were those produced by the measurement equipment. The heat loss rate from the thermocouples and pressure transducers were modelled as smooth stainless steel cylinders being affected by natural convection. Although for a full-scale test setup these losses would most likely be negligible, for a small-scale test rig with only a few channels to incur the heat losses, the proportional amount of heat loss could be significant.

### 3.5 Pressure drop analysis

The next most valuable output from the model would be the pressure drop for the recuperator. Equation (23) was derived from Equation (22) to determine the pressure drop in a specific channel (Çengel & Ghajar, 2011), while Equation (24) (integrated to account for variable mass flow rate over the inlet and outlet sections) allowed the pressure drop to be found in the inlet

and outlet header tubes that feed the channels. This approach is necessary because the fluid mass flow rate decreases linearly as the fluid flows further into the inlet header tube, being distributed among the channels, and vice versa when the fluid accumulates linearly as the fluid flows towards the exit of the outlet header tube.

$$\Delta P = \frac{fL}{D_h} \cdot \frac{\rho V^2}{2} \quad (22)$$

$$\Delta P_{channel} = \frac{fL(\dot{m}_{channel})^2(a+b)}{4\rho(ab)^3} \quad (23)$$

$$\Delta P_{headertube} = \frac{1}{L} \int_0^L \frac{f \cdot x}{D} \cdot \frac{[\dot{m}(x)]^2}{2\rho A^2} dx = \frac{4f(\dot{m}_{tot})^2(N[b+t])}{3\pi^2\rho(D)^5} \quad (24)$$

where

$$\dot{m}(x) = -\frac{\dot{m}_{tot}}{2N[b+t]} \cdot x + \dot{m}_{tot} \quad (25)$$

The total pressure drop for the entire recuperator in the STBC (see Figure 11) is simply a summation of the inlet header tube, channel and outlet header tube pressure drop for both the hot and cold sides, as shown in Equation (26).

$$\Delta P_{tot} = \Delta P_{headertube,c} + \Delta P_{headertube,h} + \Delta P_c + \Delta P_h \quad (26)$$

### 3.6 Stress analysis

The final output of note from the model would be the stress and deflection in the plates which make up the channels, due to the pressure differential from the high pressure (cold) side and the low pressure (hot) side, as shown in Figure 17. Equation (27) calculates the stress, while Equation (28) calculates the maximum deflection (Young & Budynas, 2002) of a recuperator channel plate.

$$\sigma_m = \frac{-0.5\Delta P_{avg}(a)^2}{t^2} \quad (27)$$

$$y_{max} = \frac{0.0284 P_{avg}(a)^4}{Et^3} \quad (28)$$

$\Delta P_{avg}$  is the average pressure difference across a recuperator channel plate which separates a hot channel from a cold channel while the Young's modulus,  $E$ , is evaluated at the average operational temperature of the plate.

### 3.7 Summary

In this chapter, the modelling methodology was outlined. The novel bone-shape of the stacked-plate recuperator offered a proposed solution. The heat transfer and heat loss were accounted for whilst also considering the effect of pressure loss in both the channels themselves as well as in the inlet and outlet header tubes. Finally, the mechanical stresses present in the proposed design were considered since the elevated temperatures coupled with a pressure difference would in fact affect the plate's integrity and the channel height due to deflection.

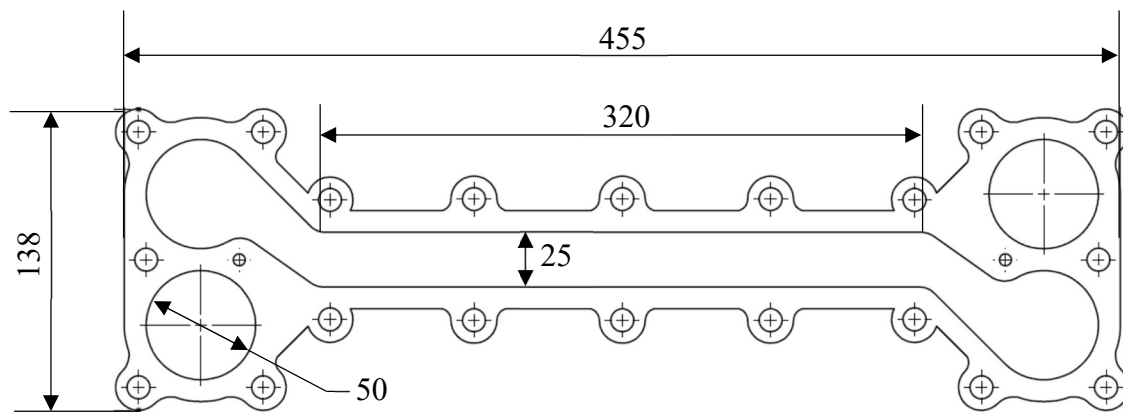
## 4 EXPERIMENTAL SETUP

### 4.1 Introduction

Two separate tests with different recuperators were conducted so that a range of data for differing geometries and fluid conditions could be acquired. This chapter details the differences between the two test rigs that were utilised during experimentation as well as the means by which the data was gathered.

### 4.2 Test 1 – Mark I rig

The Mark I design which was generated from the theoretical model, was manufactured from mild steel. The dimensions were determined iteratively during the early stages of the model's development by aiming for an effectiveness as close to 90% as possible while remaining within size and weight constraints to which a working prototype would have to adhere when attached to the small-scale STBC prototype (Wolff, et al., 2018). The pressure loss and plate deflection values also played a role in the design. Figure 19 shows a schematic representation of a Mark I recuperator gasket.



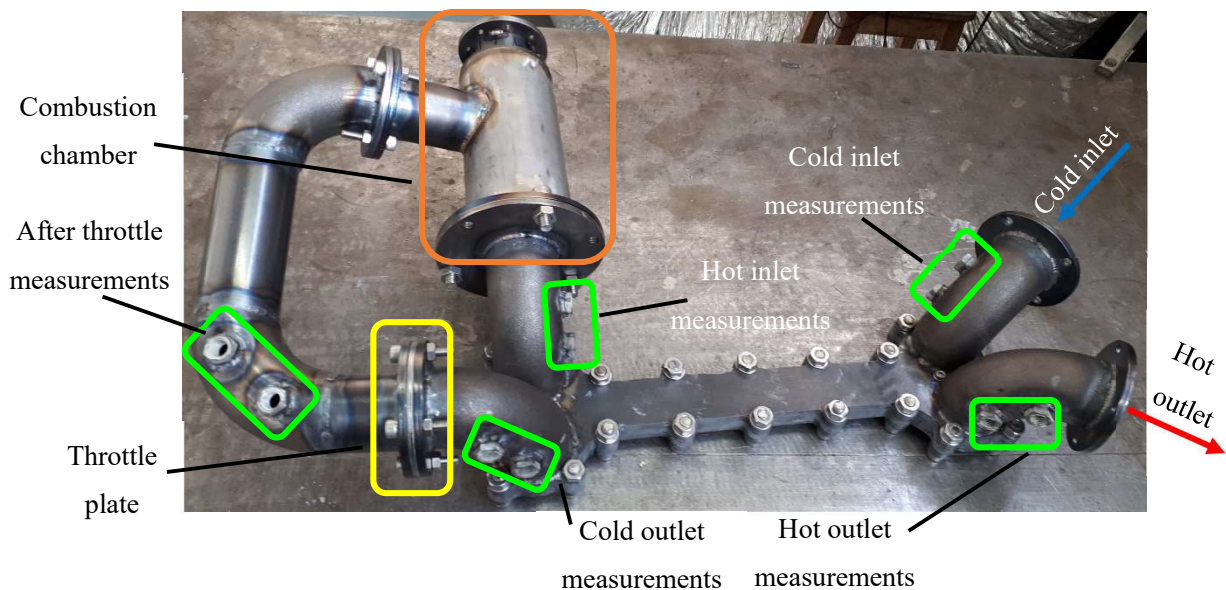
*Figure 19 Mark I recuperator gasket geometry.*

Figure 20 (right) displays the Mark I test rig, which is comprised of two channel pairs, during assembly with the sodium silicate-based sealant.



**Figure 20 SolidWorks Mark I recuperator model (left); experimental model being assembled with Calofer (right).**

To enable testing at higher temperatures while simulating the different pressures within the recuperator, a throttle plate and a combustion chamber (shown in Figure 21) were positioned between the cold-side outlet and hot-side inlet. The throttle plate had a 1.6 mm hole simulating the pressure drop that would be observed in the STBC due to the turbine and receiver while the combustion chamber simulated the heat input of the solar receiver, which increased the recuperator hot-side inlet temperature. Also indicated in Figure 21 are the points at which data was gathered with a combination of in-stream and weld-pad K-type thermocouples as well as highly accurate pressure transducers. The entire setup was insulated extensively with both ceramic fibre board and blanket to reduce heat loss. The combustion chamber was designed and constructed by the author and is a can-type design. Tungsten inert gas (TIG) welding along with various fabrication techniques such as milling, lathe work and plasma cutting were utilised to construct both test rigs.

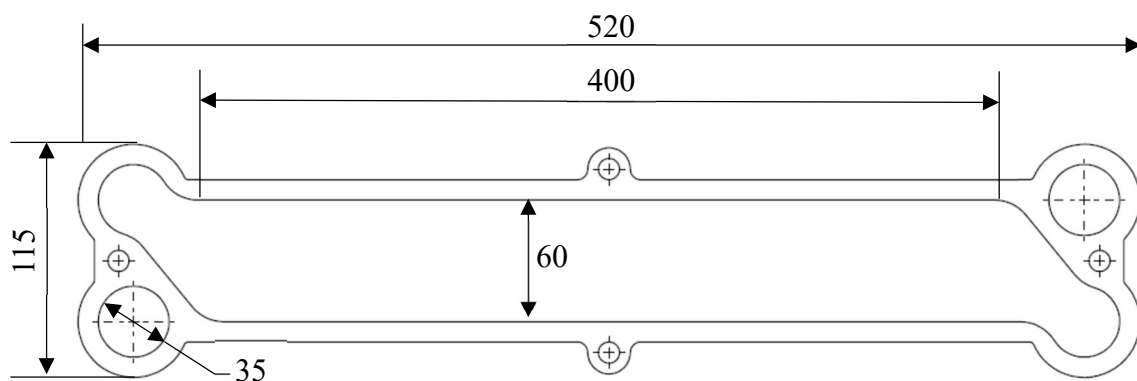


**Figure 21 Complete Mark I recuperator test rig.**

The drawback of gathering pressure data was that because the pressure transducers could not exceed 80 °C or risk failure, they had to be extended away from the measurement points by a length of copper tube so that the high temperatures at some of the positions could be cooled before reaching the pressure probes. This introduced a few issues, with the most important being the additional heat loss which had been added to the heat loss model. Another possible issue could be that the added air volume in the tube could interfere with pressure measurement because air is compressible. However, in this study, transient data was not needed for the experimental work and only steady-state values were used, thus any small undulations in pressure measurement would be negated.

### 4.3 Test 2 – Mark II rig

The second test rig (Mark II) was constructed from grade 316 stainless steel, implementing wider and longer channels, as well as more of them (20 versus two channel pairs as compared to Mark I). The goal of testing a recuperator with more channels was to increase the air mass flow rate. The need to test at higher flow rates originated from five requirements, namely; to have better combustion of the LPG (see Section 5.2.4), to experiment with alternative assembly techniques, to gain a better insight into the manufacturing logistics and expenses, to explore new geometries for further validation of the theoretical model, and to implement an industry standard mass flow meter so that accurate mass flow data could be retrieved. Figure 22 shows a schematic representation of a Mark II recuperator gasket.



*Figure 22 Mark II recuperator gasket geometry.*



*Figure 23 Mark II gasket during assembly process.*

Figure 23 displays a gasket from the Mark II test rig being coated in Soudal Calofer during the assembly process. The Calofer was prepared for application by mixing 1.5 litres with 200 millilitres of water to thin the mixture for even application and to extend the drying time. Only a portion of this mixture, roughly 500 millilitres, was actually adhered to the gaskets of the 20 channel pairs. The remainder of the Calofer was either wasted via spillage or via the cleaning of the application equipment (a small foam paint roller), or it was stored for later use.

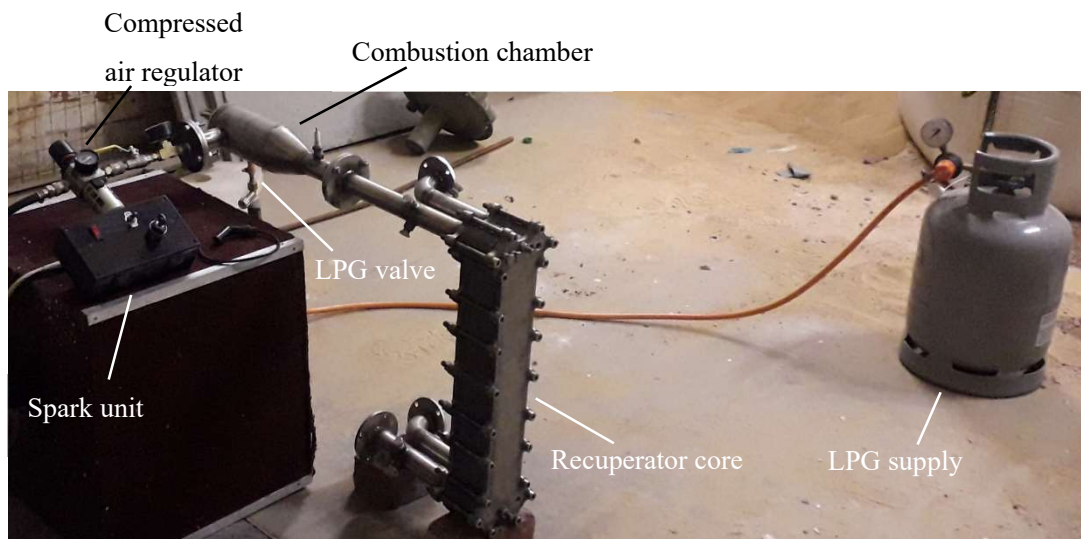


*Figure 24 Assembled Mark II core.*

The completely assembled Mark II recuperator core is displayed in Figure 24. The M10, 12.8 hardness, grade 316 stainless steel cap screws used to apply the clamping force can be observed in the figure. The ports used to attach or insert the measurement probes on the header tube



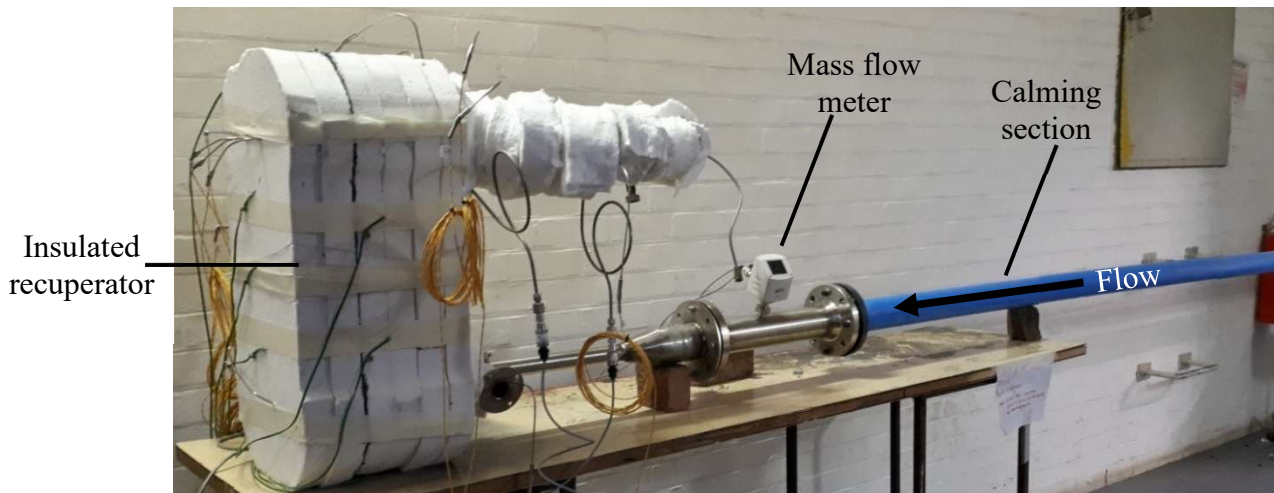
inlets and outlets are also visible. Similar to the Mark I rig, Mark II was pressure tested after the initial assembly. However, unlike Mark I, Mark II showed a leak.



***Figure 25 Partially assembled Mark II test rig.***

This could be the result of the new gasket geometry not being optimal for sealing, uneven clamping forces causing warpage, and inconsistent application of the Calofer. However, the pressure test did indicate that the mass flow leak occurred from the cold channel into the hot channel manifold port (indicated in Figure 23). It was also discovered that the leak was present on the ‘hot’ side of the recuperator, i.e. between the cold channel outlet and the hot channel inlet. This meant that by utilising the throttle plate mass flow data, the leak could be quantified by comparing the throttle plate mass flow data with data of the mass flow meter which shows the mass flow rate through the core of the recuperator. Figure 25 depicts the partially assembled Mark II test rig as it was being tested initially. Figure 26 depicts the completely assembled Mark II test rig with the Suto S421 mass flow meter installed. Note that the compressed air regulator was moved to the inlet of the calming section for the cold inlet air of the recuperator. A throttle plate with a 7.1 mm hole was installed between the cold outlet tube and the combustion chamber, similar to Figure 21. In addition to the Suto S421 mass flow meter which was supplied with a calibration certificate, the thermocouples as well as the pressure transducers were also calibrated. The calibration certificates for the mass flow meter, pressure

transducers, in-stream and weld-pad thermocouples can be found in Appendix B, C, D and E respectively.



**Figure 26 Complete Mark II test rig with calming section and mass flow meter.**

Each sensor was calibrated individually and supplied with a certificate; however, only the certificate for the most inaccurate sensor of each type is shown in the appendices. What is noteworthy is the four-metre-long inlet section shown in Figure 26. This was installed so that fully developed, uniform flow would pass the mass flow meter and accurate data could be collected. To mitigate the corrosion that was discovered in the Mark I test (see Section 5.2.4), the Mark II test rig was oriented vertically as opposed to horizontally so that any condensation formed in the hot channels upon start-up of the test rig could drain from the hot outlet. The ceramic fibre insulation board thickness was also increased for Test 2, to a thickness of 100 mm from 50 mm that was implemented for Test 1, to further reduce the total heat loss.

#### **4.4 Cost analysis**

The amount of Soudal Calofer that was used equates to a sealant assembly cost of R 4.50 per channel pair. This cost is low relative to welding or furnace brazing costs and thus adheres to the criteria stipulated in Table 3 by McDonald. Thus, the total cost per channel pair (in Rands) for the Mark II recuperator core can be characterised by Equation (29), which takes into account the cost of the stainless steel plates, gaskets as well as the top and bottom clamping plates, the stainless steel cap screws and the Soudal Calofer used. The cost of the laser cutting performed to make the plates, gaskets and clamping plates is also considered.

$$\text{Core cost } (N) = 452 \cdot (N) + 1950 \quad (29)$$

The fixed costs were considered to be the top and bottom clamping plates as well as the nuts and washers used for clamping purposes, since these components must always be present to assemble a recuperator core. Thus, the variable costs are the plates, gaskets, Calofer and the length of the bolts required.

#### 4.5 Experimental procedure

The procedure formulated for the testing of each recuperator is as follows:

- Turn on the data logger to do a test of the sensors. Determine the ambient conditions at the start of the test. The data should also be saved to check whether the computer is functioning correctly before the multiple hour-long test is carried out. The logging frequency does not need to be set high since tracking quick fluctuations during transience is not of interest. The sampling rate can be anywhere from one measurement every second to five seconds, to minimize the volume of data.
- When certain that everything is in working order, restart the logging equipment for the actual test.
- Turn on the compressed air supply to the cold-side inlet, starting with the regulator at 0 kPa. Slowly increase the pressure to achieve the operating simulated compressor pressure ratio required (for example:  $r_c = 1.45$ ), which in the case of an atmospheric pressure of  $P_{am} = 87$  kPa would equate to an operating gauge pressure of 39 kPa. Get as close as possible to the pressure ratio and allow the pressure time to stabilize. Compare the reading from the gauge fitted to the air regulator (a WIKA analog, oil-filled, 2 bar certified pressure gauge) to the pressure transducer readings from the logging system. Make the necessary adjustment to the regulator to attain the required pressure.
- Once the operating pressure has been set, ignite the burner (heat source).
- Whilst the temperatures of the system slowly rise to steady-state operating conditions, most likely over the course of a few hours, periodically make small adjustments to the regulator to maintain the operating pressure where it needs to be whilst the system

changes.

- Track the temperature increase rate over time. Once the temperatures have stopped increasing and are now hovering around a common point within a few degrees, steady-state conditions have been reached.
- Make sure the pressure in the cold channel remains at the target value once the steady state conditions have been reached.
- Let the testing continue without adjustments for at least 30 minutes to an hour at steady state whilst monitoring whether it remains steady.
- If it does not, and the temperature continues to increase, steady state has not been reached. Follow the above procedures again.
- If the temperature starts decreasing, and continues to do so without stabilizing, check the LPG bottle pressure. If it drops below the initial set operating point the amount of heat generated by the combustion chamber will decrease. The test will have to be restarted with a full bottle or a larger bottle to ensure this does not occur.
- If a successful period of steady state testing has been achieved, the heat source can now be switched off. Logging should however continue until the system has cooled significantly to monitor the probes and transducers for any signs of malfunction or error such as spikes in one or more thermocouples. If an anomaly is observed, the sensors in question should be removed for a check calibration.
- Only once either the cool down period showed no errors or the check calibration cleared the sensor, can the data be considered accurate for analysis. If errors were found, the sensor should be re-calibrated or replaced and the testing performed again.

This testing procedure can be followed as many times as necessary until sufficient data is gathered, at various operating points if required. Only after data analysis, will it be known how much more testing is needed.

#### **4.6 Summary**

The Mark I recuperator was constructed out of mild steel and consisted of only two channel pairs, whilst the Mark II recuperator was manufactured from stainless steel and constituted 20

channel pairs. Both tests implemented various thermocouples and pressure transducers for data acquisition. However, Test 2 added a calibrated mass flow meter.

## 5 TESTING AND RESULTS

---

### 5.1 Introduction

Chapter 5 details the results gathered from extensive experimental testing performed utilising the two test rigs that were constructed. Test 1 and 2 were carried out for the Mark I and II recuperators respectively, and the data was analysed to determine their performance. This was achieved by examining the temperature measurements, mass flow rate readings, pressure loss characteristics and the heat loss. Once the data from each test was analysed, the results were compared to the results generated by the theoretical model to ascertain whether it models the recuperator's performance accurately.

### 5.2 Test 1

#### 5.2.1 Temperatures

Cold inlet temperature ( $T_{c,i}$ ) [°C]	48.9
Cold outlet temperature ( $T_{c,o}$ ) [°C]	258.3
Temperature after throttle ( $T_{at}$ ) [°C]	218.2
Hot inlet temperature ( $T_{h,i}$ ) [°C]	406.4
Hot outlet temperature ( $T_{h,o}$ ) [°C]	72.7
Cold outlet wall temperature ( $T_{c,w,o}$ ) [°C]	254.9
Wall temperature after throttle ( $T_{w,at}$ ) [°C]	213.7
Hot inlet wall temperature ( $T_{h,w,i}$ ) [°C]	382.3

*Table 5 Average in-stream and wall temperature measurements at steady state.*

The steady-state data is shown in Table 5. The wall temperature measurements were recorded to compare with the in-stream values. This was due to the in-stream thermocouple being heated to a higher temperature than the walls, resulting in radiative heat transfer. The radiative heat

transfer has the effect of showing the measured fluid temperature recorded by the data logger to be lower than the actual fluid temperature. However, Table 5 shows that the difference between the measured in-stream and wall temperatures in Kelvin only ranges from 0.6% to a maximum of 3.7% for the hot inlet temperature, due to the well-insulated recuperator, which mitigates most of the heat loss from where the temperature measurements were taken. To calculate the effectiveness, the maximum available heat transfer needs to be found using Equation (30). Subsequently, the heat transfer for the channel in question needs to be determined. Equations (31) and (32) calculate the heat transfer from and to the hot and cold channels respectively. The effectiveness values for either the hot or cold channels can be determined by substituting into Equations (33) and (34) respectively. It must be noted that the effectiveness value of most importance is that of the cold channel because this effectiveness indicates how much of the waste heat is now being recycled back into the cycle. Finally, the amount of heat loss that occurs to the environment can be ascertained by implementing Equation (35):

$$\dot{Q}_{max} = \dot{m}C_{p,c}(T_{h,i} - T_{c,i}) \quad (30)$$

$$\dot{Q}_h = \dot{m}C_{p,h}(T_{h,i} - T_{h,o}) \quad (31)$$

$$\dot{Q}_c = \dot{m}C_{p,c}(T_{c,o} - T_{c,i}) \quad (32)$$

$$\varepsilon_h = \frac{\dot{Q}_h}{\dot{Q}_{max}} \quad (33)$$

$$\varepsilon_c = \frac{\dot{Q}_c}{\dot{Q}_{max}} \quad (34)$$

$$\dot{Q}_{loss} = \dot{Q}_h - \dot{Q}_c \quad (35)$$

The cold and hot-side specific heat values,  $C_{p,c}$  and  $C_{p,h}$ , were evaluated at the fluid temperature for air. The properties of the hot-side fluid were not considered to be a gas mixture because the mass flow rate of LPG during the testing was not known and nor was the air-fuel-ratio, thus making determining the fluid properties challenging. Therefore, to maintain consistency, the

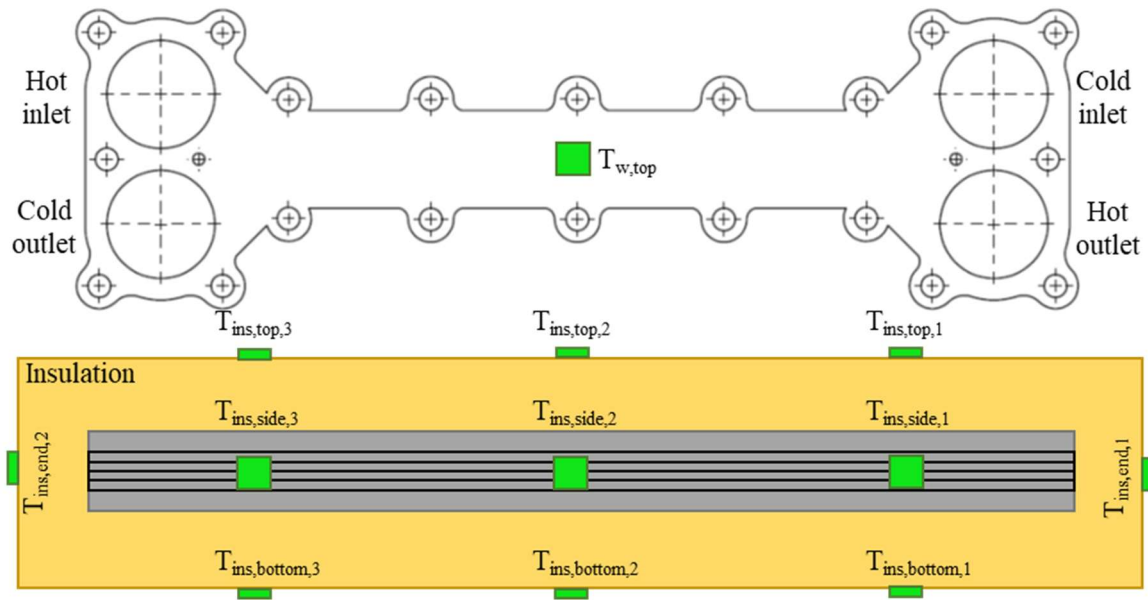
properties of air were chosen. Table 6 shows the average temperatures at steady state for the surface thermocouple measurements.

$T_{ins,top,1}$ [°C]	25.7
$T_{ins,top,2}$ [°C]	26.9
$T_{ins,top,3}$ [°C]	41
$T_{ins,side,1}$ [°C]	24.7
$T_{ins,side,2}$ [°C]	26.9
$T_{ins,side,3}$ [°C]	28.7
$T_{ins,bottom,1}$ [°C]	26
$T_{ins,bottom,2}$ [°C]	31
$T_{ins,bottom,3}$ [°C]	38.1
$T_{ins,end,1}$ [°C]	26.1
$T_{ins,end,2}$ [°C]	100.2

**Table 6 Average insulation temperatures at steady state.**

The insulation temperatures were measured at 11 points, three each on the top, side and bottom surfaces as well as one on each end of the recuperator body. The probes were placed down the centre line of the fluid path, with the first (denoted by the number 1) being closest to the ‘cold’ end of the test rig, i.e. the opposite side of where the combustion chamber is situated and where the cold inlet is; the second (denoted by the number 2) in the middle, directly above the weld-pad K-type thermocouple on the recuperator; and the third (denoted by the number 3) closest to the ‘hot’ side where the combustion chamber is located. The remaining two probes were situated on the insulation at the ends of the recuperator body, one at the air inlet and the other at the combustion chamber. Figure 27 shows the placement of the recuperator core surface thermocouples, as well as the thermocouples situated on the surface of the insulation. Note, the bottom recuperator surface thermocouple is located in the same position as the top surface probe.





**Figure 27 Mark I recuperator surface and insulation thermocouple placement.**

What is observable about the top, side and bottom insulation surface temperatures is that they increased more exponentially than linearly over the length of the recuperator, due to the fact that the conductivity of the insulation increased with temperature. A curve was fitted to the top, side and bottom surface temperatures, yielding correlation coefficients of  $R^2_{top} = 0.8236$ ,  $R^2_{side} = 0.9912$  and  $R^2_{bottom} = 0.9972$  for the top, side and bottom functions respectively, which are not ideal but better than a linear average. This yields Equations (36), (37) and (38):

$$T_{top}(x) = 24.14e^{0.468x} \quad (36)$$

$$T_{side}(x) = 24.78e^{0.149x} \quad (37)$$

$$T_{bottom}(x) = 25.88e^{0.381x} \quad (38)$$

Equations (36), (37) and (38) are then integrated for  $x$ -values from 0 to 1 representing the length of the recuperator surface to give average insulation surface temperatures of  $T_{ins,top,avg} = 30.8 \text{ }^\circ\text{C}$ ,  $T_{ins,side,avg} = 26.7 \text{ }^\circ\text{C}$  and  $T_{ins,bottom,avg} = 31.5 \text{ }^\circ\text{C}$ . These average values are shown in Table 7. The measured insulation temperatures on the ends of the recuperator were

taken to be the average values due to the small width relative to the length. The values listed in Table 7 could then be used for validation of the model.

$T_{ins,top,avg}$ [°C]	30.8
$T_{ins,side,avg}$ [°C]	26.7
$T_{ins,bottom,avg}$ [°C]	31.5
$T_{ins,end,1}$ [°C]	26.1
$T_{ins,end,2}$ [°C]	100.2
$T_{w,top,avg}$ [°C]	139.4
$T_{w,bottom,avg}$ [°C]	142.5

**Table 7 Recuperator steady-state averaged heat loss temperatures.**

### 5.2.2 Pressures

The pressure measurements took place at the same locations as the in-stream thermocouples. The measurement of the pressures allows for three key pieces of information to be determined, namely the mass flow rate, which is discussed in Section 5.2.3, the pressure ratio, and the pressure losses. The atmospheric pressure for the testing was taken at the beginning and end of each test and found to remain constant over that period at  $P_{atm} = 87$  kPa. Thus, only four pressures were actively measured during the tests, and their steady-state values can be observed in Table 8 below.

Cold inlet pressure ( $P_{c,i}$ ) [kPa]	Cold outlet pressure ( $P_{c,o}$ ) [kPa]	Pressure after throttle ( $P_{at}$ ) [kPa]	Hot inlet pressure ( $P_{h,i}$ ) [kPa]
174.1	173.1	134	132.5

**Table 8 Recuperator steady-state averaged absolute pressures.**

The pressure ratio can then be calculated using Equation (39), while Equations (40), (41) and (42) allow the cold-side, hot-side and total pressure losses to be determined:

$$r = \frac{P_{c,i}}{P_{atm}} \quad (39)$$

$$\Delta P_c = P_{c,i} - P_{c,o} \quad (40)$$

$$\Delta P_h = P_{h,i} - P_{atm} \quad (41)$$

$$\Delta P_{tot} = \Delta P_c + \Delta P_h \quad (42)$$

### 5.2.3 Mass flow rate

The role of the throttle plate in the experimental setup was to simulate the pressure drop that would be produced by the rest of the small-scale STBC, but also to allow for the determination of the mass flow rate by means of compressible flow relations utilising Mach numbers. The throttle plate (orifice plate when used as a measurement device) had a hole of known diameter (1.6 mm), and the pressures and temperatures on either side of the throttle plate were measured, thus allowing the Mach number to be calculated using Equation (43), then subsequently the mass flow rate using Equation (44) (Borgnakke & Sonntag, 2013):

$$M = -11.343 \left( \frac{P_{at}}{P_{c,o}} \right)^3 + 23.971 \left( \frac{P_{at}}{P_{c,o}} \right)^2 - 18.163 \left( \frac{P_{at}}{P_{c,o}} \right) + 5.5891 \quad (43)$$

$$\dot{m} = A_{throttle} \left[ \frac{P_{c,o}}{\sqrt{T_{c,o}}} \cdot \sqrt{\frac{\gamma}{R}} \cdot \frac{M}{\left[ 1 + M^2 \left( \frac{\gamma - 1}{2} \right) \right]^{\frac{\gamma + 1}{2(\gamma - 1)}}} \right] \quad (44)$$

where it is assumed that  $\gamma = 1.4$  and  $R = 287 \text{ J/kg.K}$ , which is the universal gas constant for air (Çengel & Ghajar, 2011), and the temperature is in Kelvin.

### 5.2.4 Results

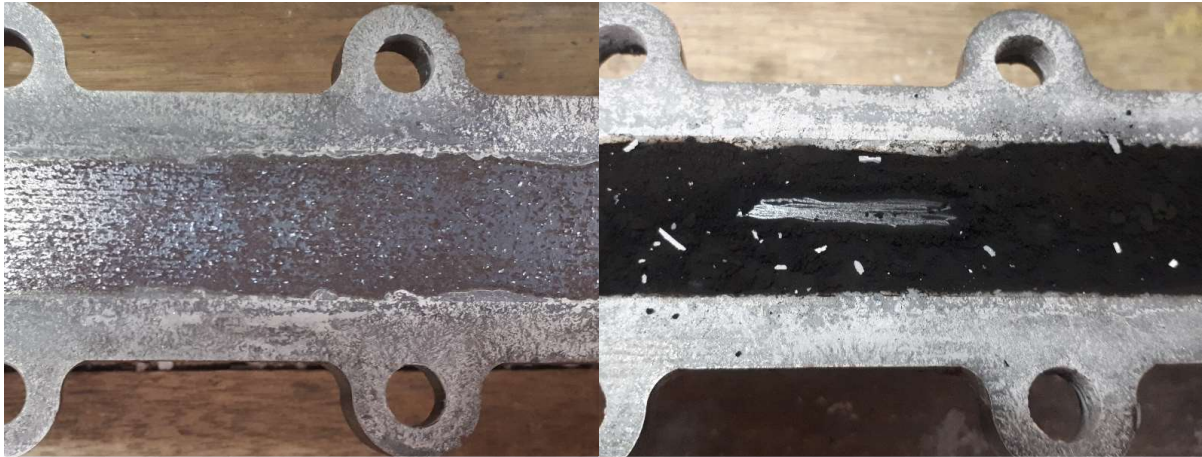
The results of the data analysis and use of equations in the previous three sections are presented below in Table 9. What is noteworthy about the results is the relatively low effectiveness and

fairly high hot-side pressure loss. To gain more insight into the reason for this occurrence as well as the performance of the high temperature sealant and the recuperator's ability to be dismantled, the test rig was disassembled.

Mass flow rate ( $\dot{m}_{tot}$ ) [kg/s]	0.000535
Maximum heat transfer rate ( $\dot{Q}_{max}$ ) [W]	194.2
Hot-side heat transfer rate ( $\dot{Q}_h$ ) [W]	182.5
Cold-side heat transfer rate ( $\dot{Q}_c$ ) [W]	113.7
Total heat loss rate ( $\dot{Q}_{loss}$ ) [W]	68.7
Cold-side effectiveness ( $\epsilon_c$ )	0.586
Pressure ratio ( $r$ )	2
Cold-side pressure loss ( $\Delta P_c$ ) [kPa]	0.9
Hot-side pressure loss ( $\Delta P_h$ ) [kPa]	45.5
Total pressure loss ( $\Delta P_{tot}$ ) [kPa]	46.4

**Table 9 Main experimental results.**

The Soudal Calofer sealed the recuperator very well but still allowed the plates to be separated without much difficulty when the clamping bolts were loosened. Upon inspection, the cold-side channels appeared to have some surface rust, most likely due to moisture. This was to be expected because the material used was mild steel. Despite the rust, there was no fouling, which resulted in a measurable layer. However, the severity of the contamination that was discovered in the hot channels was unprecedented. A thick layer of black soot coated all the heat transfer surfaces. As a result of the incomplete combustion, the fouling layer was estimated to be anywhere between 0.2 to 0.4 mm thick on each surface. This resulted in the 1 mm channel height,  $b$ , being reduced to a height varying from 0.6 mm to 0.2 mm, thus explaining the substantial pressure loss. Figure 28 provides some perspective on the contrast between the cold channels (left) and the hot channels (right).



**Figure 28** Condition of the cold channels (left) and the hot channels (right).

### 5.2.5 Model validation

To compare the model with the experimental results, the parameters that characterised the experimental setup during testing had to be inputted to the model, as shown in Table 10. Additional inputs that were necessary to approximate the experimental results included adding a fouling layer thickness to the hot-side geometry.

Pressure ratio ( $r$ )	2
Mass flow rate ( $\dot{m}_{tot}$ ) [kg/s]	0.000535
Cold inlet temperature ( $T_{c,i}$ ) [°C]	48.9
Hot inlet temperature ( $T_{h,i}$ ) [°C]	406.4
Channel width ( $a$ ) [m]	0.025
Channel height ( $b$ ) [m]	0.001
Channel length ( $L$ ) [m]	0.32
Plate thickness ( $t$ ) [m]	0.001
Number of channel pairs ( $N$ )	2

**Table 10** Mark I theoretical model inputs.

An average fouling layer thickness of  $t_f = 0.3$  mm was assumed on each surface of the hot channel, which aligned with the measured fouling thicknesses attained during the disassembly

of the test rig. Additionally, the hot-side fouling factor had to be increased from the cold-side value of  $R_{f,c} = 0.0006 \text{ m}^2\cdot\text{K}/\text{W}$  to  $R_{f,h} = 0.0125 \text{ m}^2\cdot\text{K}/\text{W}$ , which at the determined fouling thickness corresponded to a fouling thermal conductivity of  $k_f = 0.026 \text{ W}/\text{m}\cdot\text{K}$ . This conductivity is low but within the possible range of fouling conductivities (Çengel & Ghajar, 2011). Table 11 includes the remainder of the outputs from the model as well as a comparison with the experimental data.

Component	Model	Experimental	Difference
Total heat loss rate ( $\dot{Q}_{loss}$ ) [W]	68.68	68.7	0.02
Cold-side effectiveness ( $\epsilon_c$ )	0.586	0.586	0
Cold-side pressure loss ( $\Delta P_c$ ) [kPa]	0.98	0.90	0.08
Hot-side pressure loss ( $\Delta P_h$ ) [kPa]	45.4	45.5	0.1
Total pressure loss ( $\Delta P_{tot}$ ) [kPa]	46.4	46.4	0
Cold outlet temperature ( $T_{c,o}$ ) [°C]	258.5	258.3	0.2
Hot outlet temperature ( $T_{h,o}$ ) [°C]	77	72.7	4.38

**Table 11 Mark I main model outputs and comparison.**

The model outputs tend to correlate to the experimental data quite well. The 4.38 °C difference for the hot outlet temperature indicates that there are some minor additional heat losses experimentally for which the model does not account. The areas where the model lacks with respect to estimating the heat losses can be observed in Table 12, where the heat loss temperatures calculated by the model are shown and compared to the experimental measurements.

The model considers the insulation thicknesses, which are inputted values that matched the insulation thickness used on the test rig. These values are  $T_{ins,top} = T_{ins,bottom} = 60 \text{ mm}$ ,  $T_{ins,side} = 77.5 \text{ mm}$  and  $T_{ins,end} = 60 \text{ mm}$  for the top, bottom, side and end insulation sections respectively.

[°C]	Model	Experimental	Difference
$T_{ins,top,avg}$	30.6	30.8	0.2
$T_{ins,side,avg}$	27.4	26.7	0.7
$T_{ins,bottom,avg}$	31.2	31.5	0.3
$T_{ins,end,1}$	27.5	26.1	1.4
$T_{ins,end,2}$	100.2	100.2	0
$T_{w,top,avg}$	159.6	139.4	20.2
$T_{w,bottom,avg}$	141.4	142.5	1.1

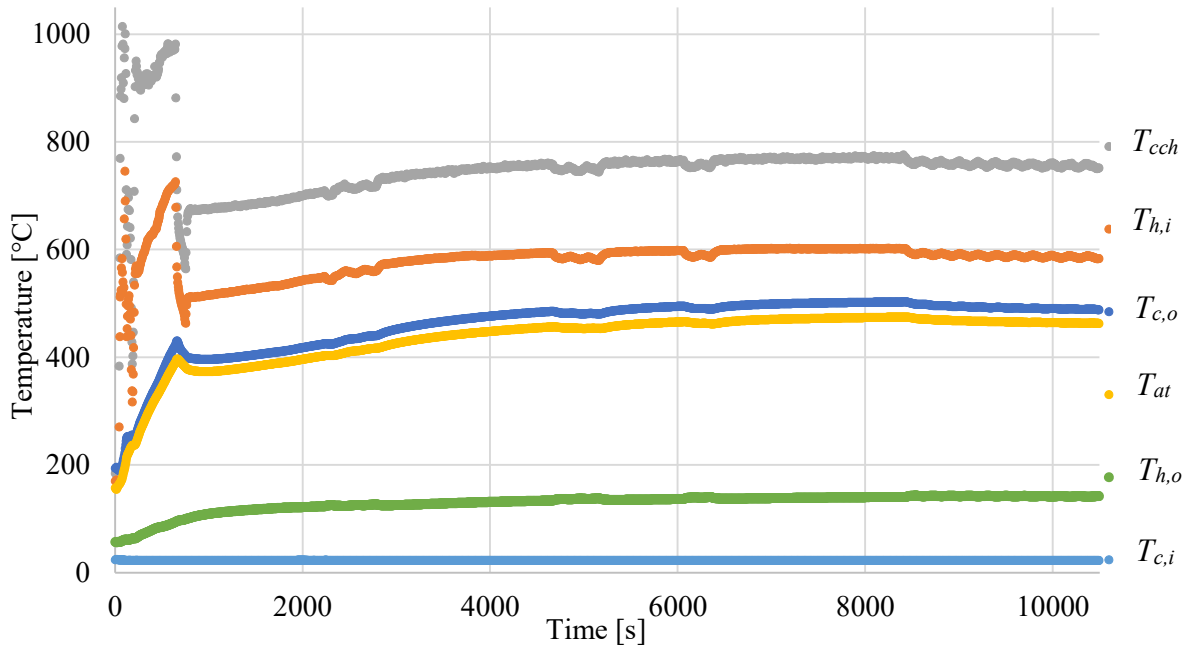
**Table 12 Model heat loss temperatures and comparison.**

Testing showed that although the Calofer sealed the Mark I recuperator very well, the combustion chamber design was not suited to the low air flow rates. The inability of the LPG to combust stoichiometrically led to incomplete combustion occurring. This was indicated during initial testing of the chamber alone, where a large yellow flame protruded from the opening, as well as during testing when black soot was occasionally ejected from the recuperator outlet. The low effectiveness could also be attributed to the low number of channel pairs. This results in the large heat losses incurred by the top and bottom surfaces only being distributed among few channels; thus, the heat loss per channel is high, significantly reducing the effectiveness. Increasing the number of channels would therefore also increase the effectiveness, purely from a relative heat loss perspective.

### 5.3 Test 2

#### 5.3.1 Temperatures

Test 2 exhibited an initial period of heavy transience while the combustion chamber was being calibrated to maintain a uniform temperature. Once stabilised, a steady-state region of operation was observed from 7100 seconds to 8520 seconds. Figure 29 displays the temperature data for the fluid stream at the various points of measurement.



**Figure 29 Test 2 measured thermocouple temperatures versus time.**

One of the advantages of the Mark II test rig over the Mark I test rig was that there were more in-stream thermocouples to measure fluid temperature at various points. The steady-state averaged fluid temperatures for Test 2 are shown in Table 13.

Cold inlet temperature ( $T_{c,i}$ ) [°C]	Cold outlet temperature ( $T_{c,o}$ ) [°C]	Temperature after throttle ( $T_{at}$ ) [°C]	Combustion temperature ( $T_{cch}$ ) [°C]	Hot inlet temperature ( $T_{h,i}$ ) [°C]	Hot outlet temperature ( $T_{h,o}$ ) [°C]
22.4	479.8	472.7	769.4	566.4	139.5

**Table 13 Test 2 steady-state fluid temperatures.**

The noteworthy difference between the combustion chamber exhaust temperature and the hot inlet temperature is discussed in Section 5.3.3.

### 5.3.2 Pressures

The steady-state pressure data for Test 2 is listed in Table 14.



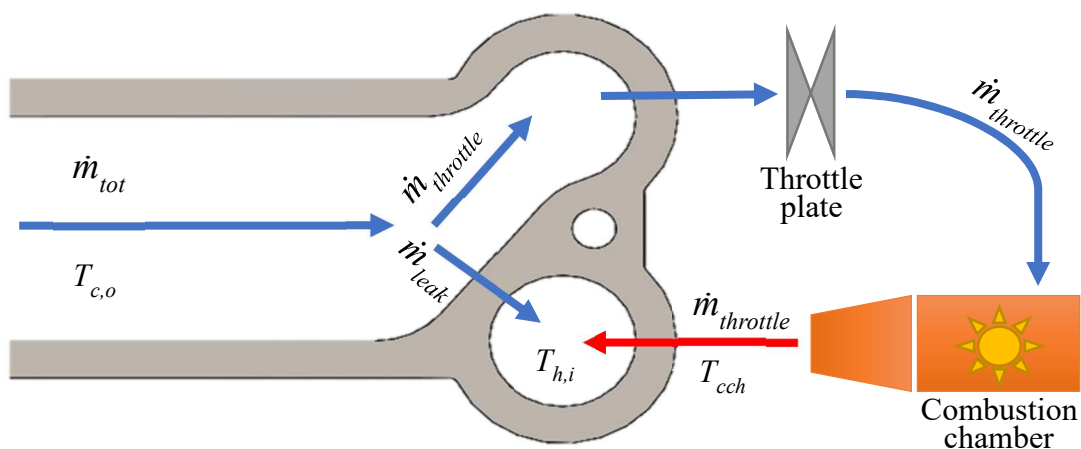
Atmospheric pressure ( $P_{atm}$ ) [kPa]	Cold inlet pressure ( $P_{c,i}$ ) [kPa]	Cold outlet pressure ( $P_{c,o}$ ) [kPa]	Pressure after throttle ( $P_{at}$ ) [kPa]	Hot inlet pressure ( $P_{h,i}$ ) [kPa]
87.9	130.9	127.9	113.3	111.9

*Table 14 Test 2 steady-state absolute pressure values.*

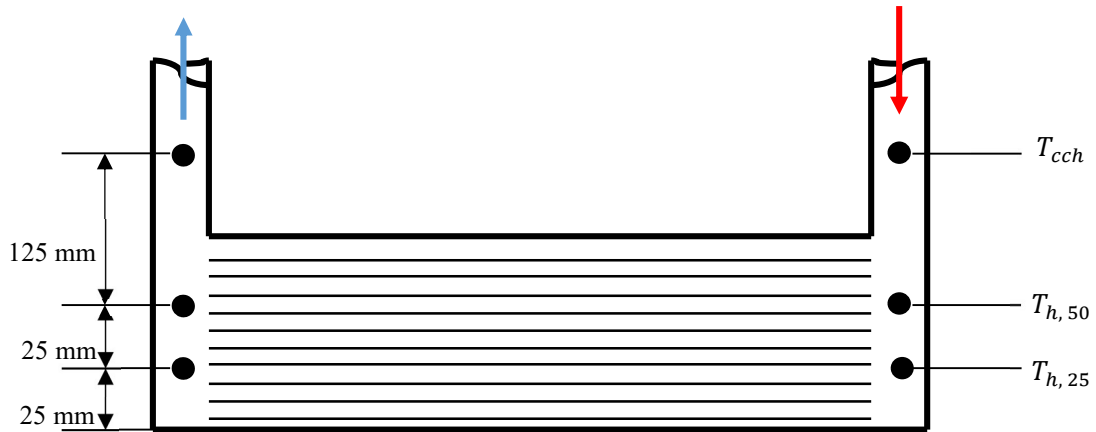
The pressure data gathered was consistent, and the cold inlet pressure was the parameter that was maintained at a constant value throughout testing to achieve a pressure ratio of about 1.5, which was proposed for the small-scale STBC (Le Roux, 2015).

### 5.3.3 Mass flow rate

The hot-side header tube leak, which was identified during the pressure test, could be quantified by means of a mass flow rate comparison as well as a mass balance if one considers a control volume around the area highlighted in Figure 23. Figure 30 is a schematic representation of the leak area. It details the division of the mass flow as well as which temperatures had to be considered. The total mass flow rate of air through the recuperator core was provided by the mass flow meter, while the throttle mass flow rate was provided via the same methodology implemented in Section 5.2.3, specifically Equations (43) and (44). The leakage as determined via the experimental data was simply the difference between the aforementioned mass flow rates. Note that the leak only affected the hot inlet temperature of the recuperator core, which still experienced the full mass flow rate.



*Figure 30 Mark II leak and mass balance schematic.*



**Figure 31 Mark II thermocouple placement.**

Total mass flow rate ( $\dot{m}_{tot}$ ) [kg/s]	Throttle mass flow rate ( $\dot{m}_{throttle}$ ) [kg/s]	Leak mass flow rate ( $\dot{m}_{leak}$ ) [kg/s]
0.0147	0.00499	0.0097

**Table 15 Test 2 mass flow data.**

Table 15 contains the mass flow rates used to calculate the hot inlet temperature. Then, using Equation (45) as well as the enthalpy values of the fluid streams, the hot inlet enthalpy can be determined.

$$h_{h,i} = \frac{\dot{m}_{leak} \cdot h_{c,o} + \dot{m}_{throttle} \cdot h_{cch}}{\dot{m}_{tot}} \quad (45)$$

Once the hot inlet enthalpy is calculated, it can be used to find the hot inlet temperature from thermodynamic tables (Borgnakke & Sonntag, 2013), the result of which is represented in Table 16. Figure 31 shows the placement of in-stream thermocouples within the Mark II test rig. The calculated hot inlet temperature can be compared with the average of the manifold ( $T_{h,25}$  and  $T_{h,50}$ ) temperature measurements (see Table 16).

Calculated hot inlet temperature ( $T_{h,i}$ ) [°C]	Average measured hot inlet manifold temperature ( $T_{h,i\_avg}$ ) [°C]
577	566.4

**Table 16 Test 2 calculated hot inlet temperature.**

The calculated hot inlet temperature is relatively close to the average of the manifold fluid temperatures, exceeding the measured value slightly. Therefore, the calculated hot fluid inlet temperature confirms the leak mass flow rate.

### 5.3.4 Results and validation

To conduct a validation, the Mark II recuperator geometries and Test 2 fluid conditions are entered into the model for the recuperator core. Table 17 contains all the necessary inputs to analyse and compare the theoretically calculated performance with the experimental results.

Pressure ratio ( $r$ )	1.49
Mass flow rate ( $\dot{m}_{tot}$ ) [kg/s]	0.0147
Cold inlet temperature ( $T_{c,i}$ ) [°C]	22.4
Hot inlet temperature ( $T_{h,i}$ ) [°C]	577
Channel width ( $a$ ) [m]	0.06
Channel height ( $b$ ) [m]	0.0009
Channel length ( $L$ ) [m]	0.4
Plate thickness ( $t$ ) [m]	0.0009
Number of channel pairs ( $N$ )	20

**Table 17 Mark II theoretical model inputs.**

Because of the accurate mass flow rate measurements, the calculated hot inlet temperature was utilised for the effectiveness calculation. Table 18 shows the results from the model and the

comparison with the experimental results. The experimental results showed a cold-side effectiveness of 82.5% and a total pressure loss of 11.48%. An error propagation analysis was performed in Appendix F, which shows that an uncertainty of 0.74% and 3.32 kPa is applicable for the cold-side effectiveness and total pressure loss respectively.

Component	Model	Experimental	Difference
Total heat loss rate ( $\dot{Q}_{loss}$ ) [W]	64.4	-147.9	212.3
Cold-side effectiveness ( $\epsilon_c$ )	0.868	0.825	0.043
Cold-side pressure loss ( $\Delta P_c$ ) [kPa]	2.08	2.95	0.87
Hot-side pressure loss ( $\Delta P_h$ ) [kPa]	21.3	21.9	0.6
Total pressure loss ( $\Delta P_{tot}$ ) [kPa]	23.4	24.9	1.5
Cold outlet temperature ( $T_{c,o}$ ) [°C]	503.8	479.8	24
Hot outlet temperature ( $T_{h,o}$ ) [°C]	99.1	139.5	40.4

**Table 18 Mark II main model outputs, experimental results and comparison.**

Upon analysis of the results, it can be noted that the model accurately predicted the cold outlet temperature, the effectiveness and the hot-side pressure loss values. The heat loss rate shows some deviation from the experimental data. However, because the calculated overall heat loss rate was a relatively low value (less than 100 W) and the thermocouples each had an error which could cascade during the calculation process, this deviation was inconsequential. The cascading of errors and additional heat loss also caused the hot outlet temperature to be experimentally higher than that of the model, while the slightly larger cold-side pressure loss was due to the leak since the cold flow channels were at a higher pressure than the hot flow channels.

#### 5.4 Summary

Testing of the two separate rigs was carried out successfully. Test 1 showed that the Mark I recuperator sealed very well, utilising the clamped-plate design with a high-temperature sealant. Due to the low number of channels, incomplete combustion of the LPG occurred and resulted in fouling. This fouling was, however, accounted for in the theoretical model, and the

experimental results validated the model, with a cold-side effectiveness of 58.6% and a total pressure loss of 17.8% having been found. Test 2 saw the implementation of a calibrated mass flow meter which allowed for a more accurate analysis. A leak was present in the boundary between the cold channel and hot inlet manifold tube, but it was quantified by comparing the throttle plate mass flow results with the mass flow meter data. The recuperator core still experienced the full mass flow rate; however, the hot inlet temperature had to be confirmed with the use of a mass and energy balance. Test 2, which also validated the analytical model, resulted in an effectiveness of 82.5% and a pressure loss of 11.48%.

## 6 CASE STUDY

### 6.1 Introduction

This chapter utilises the validated model to examine whether the proposed recuperator design could be applied to a small-scale solar thermal Brayton cycle (STBC). To explore this possibility, various geometries and recuperator configurations were modelled.

### 6.2 Results

The recuperator model can be used to explore the application of the recuperator within the small-scale STBC since it has been optimised by Le Roux & Meyer (2015) using the method of entropy generation and minimisation, thus providing input criteria from which to work. This process should provide some insight into the potential performance of the proposed recuperator and how changing various aspects of the available geometries affects its capabilities. The input parameters taken from Le Roux & Meyer (2015) are displayed in Table 19.

Pressure ratio ( $r$ )	Total mass flow rate ( $\dot{m}_{tot}$ ) [kg/s]	Cold inlet temperature ( $T_{c,i}$ ) [°C]	Hot inlet temperature ( $T_{h,i}$ ) [°C]	Ambient temperature ( $T_{\infty}$ ) [°C]
1.49	0.06	83.7	726.9	27

*Table 19 Optimised STBC input parameters.*

The additional parameters, that were fixed for the modelling process, can be observed in Table 20. These include the plate thickness and channel height. These parameters were fixed at this value because it is a commonly available thickness of grade 316 stainless steel sheet, from which the symmetrical plates and gaskets could easily and cost-effectively be manufactured. Therefore, the channel width could be ascertained next in a pre-calculation, using the model, to determine a fixed channel width input for the remainder of the modelling. This was achieved by increasing the width of the channel so that a pressure ratio of  $r = 2$  (selected as a precaution

to account for possible off-optimal operating points during transient periods) resulted in a safety factor of 2 between the maximum plate stress and yield stress of grade 316 stainless steel at 800 °C. This ensured that no significant deflection would occur so as to close off the channels, as well as ensuring that creep deterioration would be limited. It was also assumed that for the real application, the LPG or another preferred fuel would be completely combusted, thus resulting in either no or an insignificant fouling layer thickness.

Plate thickness ( $t$ ) [m]	Channel height ( $b$ ) [m]	Channel width ( $a$ ) [m]
0.001	0.001	0.05

**Table 20 Additional STBC modelling parameters.**

In addition to the aforementioned inputs, the same insulation thicknesses as the Mark II test rig was used. The type and number of measurement probes that were considered in the validation were also kept consistent and matched the experimental test rig. Making use of these parameters, Figure 32 and Figure 33 were generated by plotting the effectiveness and pressure loss against the number of channels for varying channel lengths respectively. Additionally, the plots for the various channel lengths ended at different positions, due to the hot-side outlet temperature approaching the cold-side inlet temperature. Increasing the number of channels would not result in further heat transfer occurring. Once these plots were created, a length of  $L = 0.25$  m was selected due to it exhibiting the best combination of a high effectiveness and low pressure drop. With this added constant, Figure 34 was generated whereby varying numbers of recuperators were connected in parallel, thus dividing the total mass flow rate among them. Once again, the effectiveness and pressure loss versus number of channels were plotted for one, two, three and four recuperators in parallel.

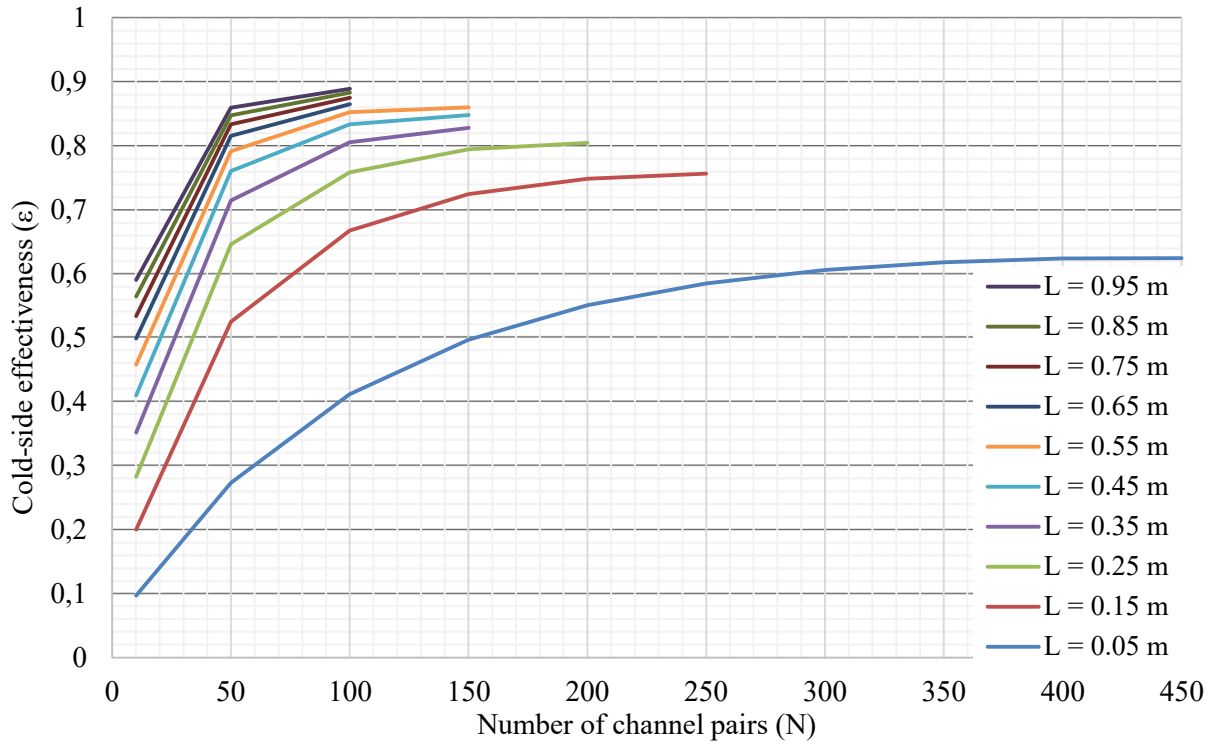


Figure 32 Model results for effectiveness versus number of channel pairs at various channel lengths.

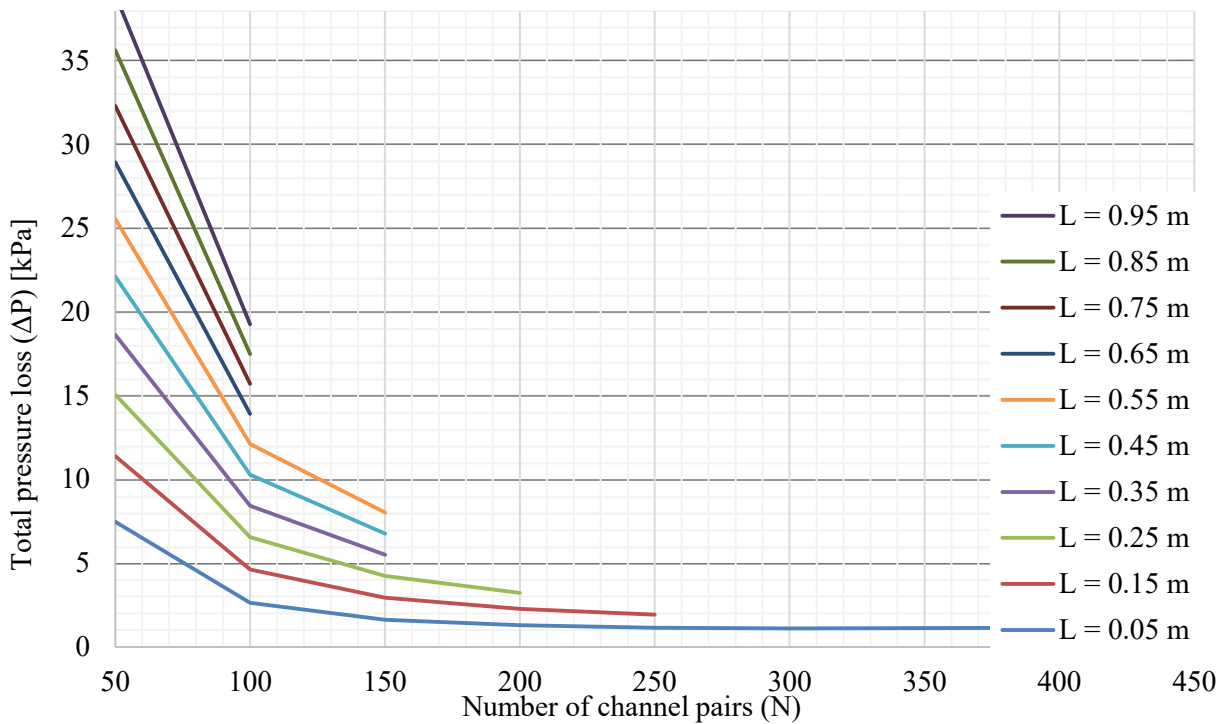
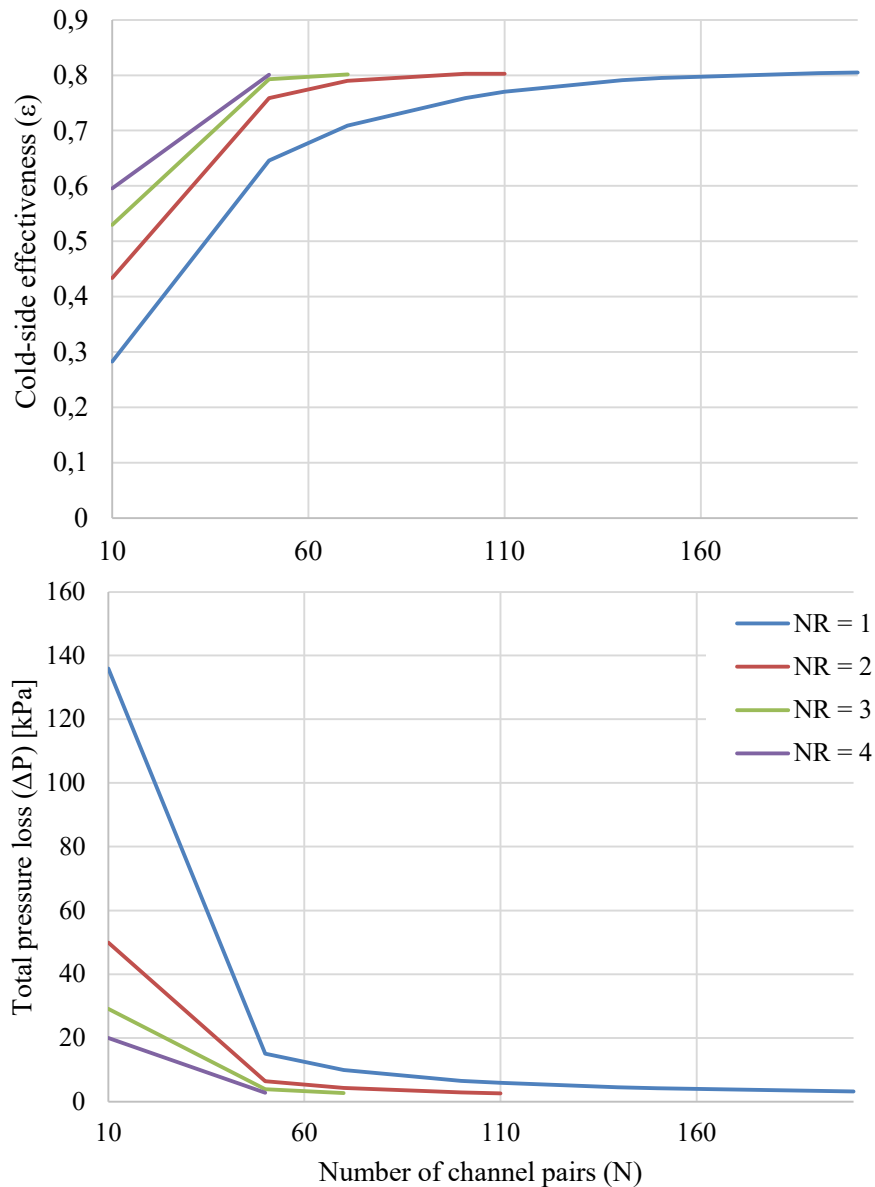


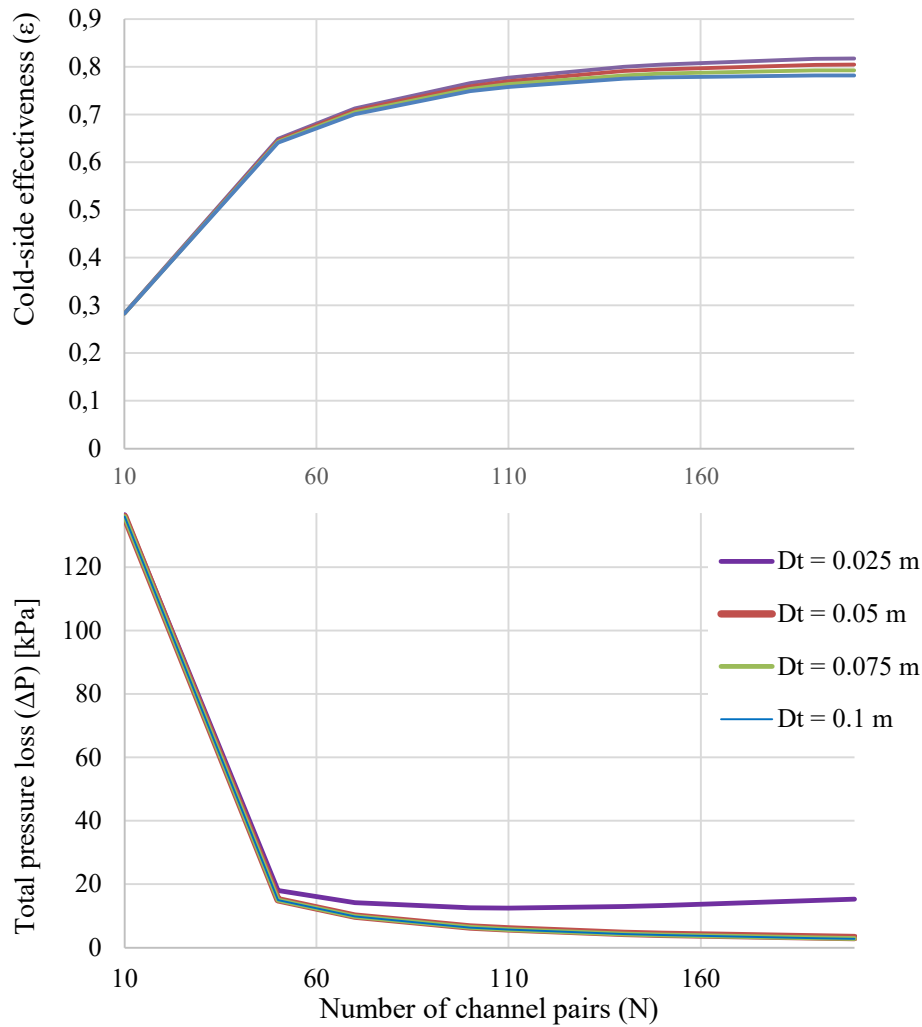
Figure 33 Model results for pressure loss versus number of channel pairs at various channel lengths.





**Figure 34 Effectiveness (top) and pressure loss (bottom) versus number of channel pairs for different numbers of recuperators.**

Another geometrical factor that was explored was that of the manifold tube diameters. Similar to Figure 34, the channel length was kept constant at  $L = 0.25$  m, but only a single recuperator was analysed at four different tube diameters. The smallest was 25 mm because any smaller produced larger pressure losses than what could possibly be allowed, and the largest was 100 mm due to the fact that increasing it further would not result in any significant reduction in pressure loss, but the heat loss would continue to increase, resulting in a lower effectiveness. Figure 35 shows the results of the aforementioned analysis:



**Figure 35 Effectiveness (top) and pressure loss (bottom) versus number of channel pairs for varying manifold tube diameters.**

### 6.3 Summary

The results of the analyses showed that there appeared to be no combination of geometries which allowed the recuperator design with parameters shown in Table 19 and Table 20 to adhere to the specifications set forth by McDonald (2000) because a cold-side effectiveness of 90% or above could not be achieved while maintaining a total pressure loss of below 5%. A maximum cold-side effectiveness of 89% with a total pressure loss of 19 kPa (8.8% loss) is shown in Figure 32 and Figure 33 where  $L = 0.95$  m. A 5% total pressure loss with the pressure ratio stipulated in Table 15 at an atmospheric pressure of  $P_{atm} = 87$  kPa equated to a total pressure loss of  $\Delta P_{tot} = 10.88$  kPa. Figure 32 shows that this can be achieved when  $N = 100$  and  $L = 0.45$  m, with an effectiveness of about 84%. It is recommended that the recuperator

could be successfully utilised within the small-scale STBC as well as a wide range of other potential applications for waste heat recovery where efficiencies of up to 89 % are required (see Figure 32). Despite the already promising results, there are other geometries which could be explored to further improve the performance of the recuperator. For example, a larger channel height could be examined, where recuperator height restrictions are not as important.

## 7 SUMMARY, CONCLUSION AND RECOMMENDATIONS

---

### 7.1 Summary

South Africa is an amazingly diverse country plagued by rolling blackouts, and many citizens do not have access to electricity or clean water. There is also a dire need for job creation. It has been stated that a personalised micro-turbine power generation system presents a solution to this issue and that it may become as commonplace as a personal computer. Couple this to South Africa's excellent solar direct normal irradiation (DNI) levels, and a small-scale recuperated solar thermal Brayton cycle (STBC) shows enormous potential. However, a recuperator comprises up to 30% of the capital cost associated with a micro-turbine package and requires complex and costly manufacturing methods within a South African context. Thus, the objective of this research was to investigate a clamped plate-style recuperator that can be cost-effectively manufactured locally.

Literature was consulted and criteria were outlined that a recuperator in a Brayton cycle should adhere to, stipulating that a cold-side effectiveness of 90% or above and a total pressure loss of less than 5% are necessary. To meet these requirements, it is suggested that a counterflow plate-style recuperator be used. To prevent complex manufacturing methods, a gasketed stacked-plate design was proposed. A sodium silicate-based sealant called Soudal Calofer is available locally and can withstand the operating temperatures of an STBC.

The modelling methodology was outlined, and the novel bone-shape of the stacked-plate recuperator offered a proposed solution. The heat transfer and heat losses were successfully accounted for whilst also considering the effect of pressure loss in both the channels themselves as well as in the inlet and outlet manifold tubes. Finally, the mechanical stresses present in the proposed design were also considered since the elevated temperatures coupled with a pressure difference would in fact affect the plate's integrity and the channel height due to deflection.

### 7.2 Conclusion

Experimental testing was carried out successfully on two small-scale versions of the proposed recuperator design, and consistent data was gathered. The testing showed firstly that the physical construction was simple and cost-effective, and that the clamped plate-style high-

temperature sealant combination worked very well for the recuperator core, facilitating an easy assembly and disassembly process. The ability of the recuperator to be easily disassembled allowed for a thorough post-testing inspection. The construction sustained an airtight seal (Mark I) at various pressures and high temperatures for the entire testing period, provided the assembly process was done in an expedient manner as well as uniformly. Despite the occurrence of heavy soot-based fouling deposits during Test 1, due to incomplete combustion of the LPG as a result of the very low air mass flow rates, the model was able to match the values gathered from the testing within a few percent, considering the aforementioned fouling layer's thickness and conductivity. The data showed a cold-side effectiveness of 58.6% and a total pressure loss of 17.78%. In the case of Test 2, a leak of the total mass flow rate from the cold channel to the hot inlet manifold tube was identified, quantified and accounted for, after which the model closely matched the experimental results for the recuperator core. This resulted in a cold-side effectiveness of 82.5% and a total pressure loss of 11.48%.

As a case study, input data from literature, gathered from an optimisation study conducted on the small-scale STBC, was implemented to investigate whether a specific recuperator design could function well within the STBC. The results showed that the combination of an effectiveness of 84% and a pressure loss of less than 5% could be attained when implementing the recuperator within the STBC for 100 channel pairs with channel height of 1 mm, channel width of 50 mm, and a channel length of 450 mm. Alternatively, if pressure loss is of less concern to the user, a cold-side effectiveness of 89% can be achieved by increasing the total pressure loss to 19 kPa with  $L = 950$  mm, which equates to an 8.8% total pressure loss. Because the STBC is not a mobile application and the main heat source is solar-thermal energy, the aforementioned performance characteristics could be very useful. Furthermore, the design may prove valuable where a cost-effective recuperator, which can easily be assembled and disassembled, is required.

### **7.3 Recommendations**

For future work, it is recommended that a large-scale recuperator be built and tested to confirm the performance characteristics of larger mass flow rates and that the insulation of the unit be varied to determine the effects thereof. Furthermore, the design could possibly benefit from the addition of heat transfer enhancement mechanisms. One such adjustment would be to have the

plates either laser cut out and then indented to form structural ridges or to have them stamped out of sheet with the structural geometries included. This will allow for a larger channel width to be explored before mechanical stress and deflection of the plates becomes an issue. A larger channel width should improve the heat transfer to heat loss area ratio while maintaining overall compact dimensions.

The main areas of concern should be the gasket geometry and assembly method so as to develop a uniform and consistent assembly technique that results in an airtight seal for every unit assembled. This may be achieved by regulating the amount of water added to the Soudal Calofer for thinning purposes to achieve a consistency which facilitates uniform application and extended drying time to allow for the assembly to be completed, while not thinning the sealant too much so as to lead to a seal failure. In conjunction, the clamping force distribution is critical to sealing the inner channel division, where the leak occurred in Test 2. Alternatively, the channel division section of the gasket should be designed more carefully to aid the Calofer in sealing, perhaps by incorporating a double-walled design, thus trapping Calofer more securely.

Furthermore, it is recommended that the usable lifespan of such a recuperator be determined. To do so, one or several recuperators, potentially of varying geometries, could be tested at a multitude of operating conditions. Most crucially, thermal and pressure cycling must be investigated, especially when seal integrity is concerned.

A potential solution to the requirements for a cost-effective, locally manufactured recuperator has been investigated in this work. The theoretical model was validated by data gathered from multiple experiments, illustrating that potential recuperator geometries exist that will function as required within a small-scale solar thermal Brayton cycle. This could have positive implications for the South African energy industry.

## 8 REFERENCES

---

- Aeristech, 2015. *FullElectric Turbocharger*. [Online]  
Available at: <http://www.aeristech.co.uk/full-electric-turbocharger-technology/>  
[Accessed 16 March 2019].
- Allen, K. G., 2010. *Performance characteristics of packed bed thermal energy storage for solar thermal power plants*, Thesis: University of Stellenbosch.
- Aquaro, D. & Pieve, M., 2007. High temperature heat exchangers for power plants: Performance of advanced metallic recuperators. *Applied Thermal Engineering*, Volume 27, pp. 389-400.
- Bladon, 2019. *Bladon MT*. [Online]  
Available at: <https://www.bladonmt.com/micro-turbine-genset/the-bladon-mtg>  
[Accessed 19 November 2019].
- Borgnakke, C. & Sonntag, R. E., 2013. *Fundamentals of Thermodynamics*. 8th ed. Michigan: Don Fowley.
- BorgWarner, 2016. *History*. [Online]  
Available at: <http://www.turbos.bwauto.com/products/turbochargerHistory.aspx>  
[Accessed 17 March 2019].
- Cadorin, M. et al., 2012. Analysis of a Micro Gas Turbine Fed by Natural Gas and Synthesis Gas: MGT Test Bench and Combustor CFD Analysis. *Journal of Engineering for Gas Turbines and Power*, 134(71401).
- Cameron, H., Mueller, L. & Namkoong, D., 1972. *Preliminary design of a solar heat receiver for a Brayton-cycle space power system*, Washington, D.C.: Report NASA TM X-2552, National Aeronautics and Space Administration, Lewis Research Center.

Capehart, B. L., 2016. *Microturbines*. [Online]

Available at: <https://www.wbdg.org/resources/microturbines.php>

[Accessed 2 December 2019].

Capstone, 2019. *C30 Microturbine*. [Online]

Available at: <https://www.capstoneturbine.com/products/c30>

[Accessed 5 August 2019].

Çengel, Y. A. & Ghajar, A. J., 2011. *Heat and Mass Transfer: Fundamentals and Applications*. 4 ed. New York: McGraw-Hill.

Clay, A. & Tansley, G. D., 2011. Exploration of a simple, low cost, micro gas turbine recuperator solution for a domestic combined heat and power unit. *Applied Thermal Engineering*, Volume 31, pp. 2676-2684.

Cordova, J. L., Walton, J. F. & Heshmat, H., 2015. *High effectiveness, low pressure drop recuperator for high speed and power oil-free turbogenerator*. Montréal, Canada, ASME.

Department of Energy South Africa, 2019. *Coal resources*. [Online]

Available at: [http://www.energy.gov.za/files/coal\\_frame.html](http://www.energy.gov.za/files/coal_frame.html)

[Accessed 29 November 2019].

Department of Statistics South Africa, 2019. *Youth graduate unemployment rate increases in Q1: 2019*. [Online]

Available at:

<http://www.statssa.gov.za/?p=12121#:~:targetText=Youth%20graduate%20unemployment%20rate%20increases%20in%20Q1%3A%202019,1st%20quarter%20of%202019>.

[Accessed 20 November 2019].

Dickey, B., 2011. *Test results from a concentrated solar microturbine Brayton cycle integration*. Vancouver, British Columbia, Canada, In: Proceedings of ASME TurboExpo, GT2001, June 6-10.



Everts, M. & Meyer, J. P., 2018. Flow regime maps for smooth horizontal tubes at a constant heat flux. *International Journal of Heat and Mass Transfer*, Volume 117, pp. 1274-1290.

Formula 1 Dictionary, 2014. *2014 Formula 1 Rule change New Power Unit (1.6 V6) with ERS*. [Online]

Available at: [http://www.formula1-dictionary.net/engine\\_power\\_unit\\_and\\_ers.html#index\\_top\\_page](http://www.formula1-dictionary.net/engine_power_unit_and_ers.html#index_top_page)  
[Accessed 6 December 2019].

G+L Innotec, 2014. *Turbo-by-wire*. [Online]

Available at: [http://www.gl-innotec.de/index.php?id=31&tx\\_ttnews%5Byear%5D=2014&tx\\_ttnews%5Bmonth%5D=05&tx\\_ttnews%5Bday%5D=16&tx\\_ttnews%5Btt\\_news%5D=13&L=1&cHash=d28ab73d99a3113781d6c70984b56d16](http://www.gl-innotec.de/index.php?id=31&tx_ttnews%5Byear%5D=2014&tx_ttnews%5Bmonth%5D=05&tx_ttnews%5Bday%5D=16&tx_ttnews%5Btt_news%5D=13&L=1&cHash=d28ab73d99a3113781d6c70984b56d16)

[Accessed 15 March 2019].

Garrett, 2009. *Garrett by Honeywell: Turbochargers, Intercoolers, Upgrades, Wastegates, BlowOff Valves, Turbo-Tutorials*. [Online]

Available at: <http://www.TurboByGarrett.com>

[Accessed 26 April 2010].

Heli-Factory, 2013. *HELICOPTER-TURBINES*. [Online]

Available at: <http://www.heli-factory.com/eng/turbines/helicopter-turbinen/index.php>

[Accessed 26 November 2019].

Jakadofsky, 2019. *Jakadofsky Jet Engines*. [Online]

Available at: <https://jakadofsky.com/index1.php?bereichID=11&lang=en>

[Accessed 19 November 2019].

Kesseli, J., Wolf, K., Nash, J. & Freedman, S., 2003. *Micro, industrial and advanced gas turbines employing recuperators*. New York, NY, ASME, pp. ASME Paper No. GT2003-38938.

Korzynietz, R. et al., 2016. Solugas – Comprehensive analysis of the solar hybrid Brayton plant. *Solar Energy*, Volume 135, pp. 578-589.

Lanchi, M. et al., 2015. Investigation into the coupling of Micro Gas Turbines with CSP technology: OMSoP project. *Energy Procedia*, Volume 69, pp. 1317-1326.

Le Roux, W. G., 2015. *Thermodynamic optimisation and experimental collector of a dish-mounted small-scale solar thermal Brayton cycle*, Thesis: Department of Mechanical and Aeronautical Engineering, University of Pretoria.

Le Roux, W. G., 2018. *Feasibility study of a hybrid small-scale dish-mounted solar thermal Brayton cycle with cogeneration*. Beijing, China, IHTC, pp. 7929-7936.

Le Roux, W. G., Bello-Ochende, T. & Meyer, J. P., 2013. *A review on the thermodynamic optimization and modelling of the solar thermal Brayton cycle*, Pretoria: Renewable and Sustainable Energy Reviews, Volume 28: pp. 677–690.

Le Roux, W. G., Bello-Ochende, T. & Meyer, J. P., 2014. *Optimization of an open rectangular cavity receiver and recuperator used in a small-scale solar thermal Brayton cycle with thermal losses*, s.l.: Energy Conversion and Management, Volume 84: 457-470.

Le Roux, W. G. & Meyer, J. P., 2015. *Modelling the small-scale dish mounted solar thermal Brayton cycle*. Cape Town, In: AIP Conference Proceedings (SolarPACES) 1743, pp. 060002-1-060002-8.

Le Roux, W. G. & Meyer, J. P., 2017. Small-scale dish-mounted solar thermal Brayton cycle. In: *Clean Energy for Sustainable Development*. 1 ed. Queensland: Elsevier, pp. 167-190.

Le Roux, W. G. & Sciacovelli, A., 2019. Recuperated solar-dish Brayton cycle using turbocharger and short-term thermal storage. *Solar Energy*, Volume 194, pp. 569-580.

McDonald, C. F., 2000. Low-cost compact primary surface recuperator concept for micro-turbines. *Applied Thermal Engineering*, Volume 20, pp. 471-497.

McDonald, C. F., 2003. Recuperator considerations for future higher efficiency micro-turbines. *Applied Thermal Engineering*, Volume 20, pp. 1463-1487.

McDonald, C. F. & Rodgers, C., 2002. The ubiquitous personal turbine-A power vision for the 21st Century. *Journal of Engineering for Gas Turbines and Power*, Volume 124, pp. 835-844.

Meyer, J. P. & Everts, M., 2018. Single-phase mixed convection of developing and fully developed flow in smooth horizontal circular tubes in the laminar and transitional flow regimes. *International Journal of Heat and Mass Transfer*, Volume 117, pp. 1251-1273.

Mills, D., 2004. Advances in solar thermal electricity technology. *Solar Energy*, 76(1-3), pp. 9 -31.

Mirshahidi, S., 2012. *KJ-66 RC TurboJet Engine*. [Online]  
Available at: <https://grabcad.com/library/kj-66-rc-turbojet-engine-1>  
[Accessed 17 March 2019].

MTT, 2019. *EnerTwin Technology*. [Online]  
Available at: [https://www.enertwin.com/cms/EN\\_Specifications\\_EnerTwin-2017.pdf](https://www.enertwin.com/cms/EN_Specifications_EnerTwin-2017.pdf)  
[Accessed 4 December 2019].

Nellis, G. F. & Pfothner, J. M., 2005. Effectiveness-NTU relationship for a counterflow heat exchanger subjected to an external heat transfer. *Journal of Heat Transfer*, Volume 127, pp. 1071-1073.

Ohadi, M. M. & Buckley, S. G., 2001. High temperature heat exchangers and microscale combustion systems: applications to thermal system miniaturization. *Experimental Thermal and Fluid Science*, Volume 25, pp. 207-217.

Pietsch, A. & Brandes, D. J., 1989. *Advanced solar Brayton space power systems*. Los Alamitos, In: Proceedings of Intersociety Energy Conversion Engineering Conference (IECEC), pp. 911-916.

Samad Power Ltd, 2019. *TGB2*. [Online]  
Available at: <https://samad-power.co.uk/micro-chp-series/>  
[Accessed 19 November 2019].

Samad Power Ltd, 2019. *TwinGen*. [Online]  
Available at: <https://samad-power.co.uk/micro-chp-series/>  
[Accessed 19 November 2019].

Scaccia, C. & Theoclitus, B., 1980. Heat exchangers-types, performance and applications. *Chemical Engineering*, Volume 20, pp. 121-132.

Schoeman, T. & Saunders, M., 2018. *The impact of power outages on small businesses in the city of Johannesburg*. Cape Town, In: Proceedings of International Conference on Education, Business, Humanities and Social Sciences Studies (EBHSSS-18), pp. 328-333.

Shah, R. K., 1981. *Heat Exchangers: Thermal-Hydraulic Fundamentals and Design*. Washington, DC: Hemisphere Publishing.

Shah, R. K., 2005. *Compact heat exchangers for micro-turbines*. Hoboken, NJ, In: Proceedings of Fifth International Conference on Enhanced, Compact and Ultra-Compact Heat Exchangers: Science, Engineering and Technology, pp. 247-257.

Shiraishi, K. & Ono, Y., 2007. *Hybrid turbocharger with integrated high speed motor-generator*, Nagasaki, Japan: Mitsubishi Heavy Industries, Ltd.

Solargis, 2019. *Solar resource maps and GIS data for 200+ countries*. [Online]  
Available at: <https://solargis.com/maps-and-gis-data/overview>  
[Accessed 10 November 2019].

Soudal, 2015. *Calofer: Technical data sheet*. [Online]  
Available at: <https://www.pfe.tech/wp-content/uploads/2017/02/Calofer-TDS-ID253.pdf>  
[Accessed 12 March 2019].

Ssebabi, B., Dinter, F., van der Spuy, J. & Schatz, M., 2019. Predicting the performance of a micro gas turbine under solar-hybrid operation. *Energy*, Volume 177, pp. 121-135.

Stevens, T., Verplaetsen, F. & Baelmans, M., 2004. *Requirements for recuperators in micro gas turbines*. Kyoto, Japan, In: Proceedings of Fourth International Workshop on Micro and Nanotechnology for Power Generation and Energy Conversion Applications (IWMNPGECA), pp. 96-99.

Turbo Direct, 2019. *Home*. [Online]  
Available at: <http://www.turbodirect.co.za/site/>  
[Accessed 25 November 2019].

Van Greuning, J., 2006. *Material Selection and Optimisation of a High-Temperature Compact Heat Exchanger*, Potchefstroom: Thesis: School of Mechanical and Materials Engineering, North-West University.

Vick, M. J., 2012. *High efficiency recuperated ceramic gas turbine engines for small unmanned air vehicle propulsion*, London: Imperial College London: Department of Mechanical Engineering.

Visser, W. P. J., Shakariyants, S. A. & Oostveen, M., 2011. Development of a 3 kW microturbine for CHP applications. *Journal of Engineering for Gas Turbines and Power*, Volume 133, pp. 042301-1-042301-8.

Wang, K. et al., 2015. Experimental study on a coiled tube solar receiver under variable solar radiation condition. *Solar Energy*, Volume 122, pp. 1080-1090.

Weston, K. C., 2000. *Energy Conversion*. [e-book]. [Online]  
Available at: <http://www.personal.utulsa.edu/~kenneth-weston>  
[Accessed 07 December 2019].

Wolff, T. M., Le Roux, W. G. & Meyer, J. P., 2018. *Heat loss analysis for an open-cavity tubular solar receiver*. Beijing, China, In: Proceedings of the 16th International Heat Transfer Conference (IHTC-16), pp. 7695-7702.

World Energy Council, 2016. *Average electricity consumption per electrified household*. [Online]  
Available at: <https://wec-indicators.enerdata.net/household-electricity-use.html>  
[Accessed 04 December 2019].

Xiao, G. et al., 2017. Recuperators for micro gas turbines: a review. *Applied Energy*, Volume 197, pp. 83-99.

Young, W. C. & Budynas, R. G., 2002. *Roark's Formulas for Stress and Strain*. 7th ed. New York: McGraw-Hill.

# APPENDICES

## Appendix A Soudal Calofer specification sheet (Soudal, 2015)



Technical Data Sheet

### Calofer

Revision: 8/09/2015

Page 1 from 2

#### Technical data

Basis	Sodium silicate
Consistency	Stable paste
Curing system	Physical drying
Density	1,82 g/ml
Maximum allowed distortion	Ca. 2 %
Temperature resistance	-40 °C → 1500 °C
Application temperature	5 °C → 30 °C

(\*) these values may vary depending on environmental factors such as temperature, moisture, and type of substrates.

#### Product description

Calofer is a high quality sealing paste based on sodium silicate.

#### Properties

- Ready for use
- No fragmentation or cracking after curing
- Heat resistant up to 1500°C
- Free of asbestos

#### Applications

- Sealing of joints and openings where high temperatures are possible.
- Sealing of stoves, ovens, fireplaces.

#### Packaging

Colour: black

Packaging: 310 ml cartridge

#### Shelf life

12 months in unopened packaging in a cool and dry storage place at temperatures between +5°C and +25°C. Protect against frost.

#### Substrates

Substrates: brick, concrete, metals

Nature: clean, dry, free of dust and grease.

Surface preparation: Slightly moistening porous surfaces improves the adhesion.

We recommend a preliminary compatibility test.

#### Joint dimensions

Min. width for joints: 5 mm

Max. width for joints: 15 mm

#### Application method

Application method: Apply with spatula, filling knife or sealing gun.

Cleaning: Before curing, Calofer can be removed with water from substrates and tools.

Finishing: Finish with a spatula or putty knife.

Repair: With the same material

#### Health- and Safety Recommendations

Take the usual labour hygiene into account.

Consult the packaging label for more information.

#### Remarks

- A slight warming of the heating installation during 12 hours after application prevents bubbleforming and improves structure.
- Do not apply in situations where constant water immersion is possible.

#### Environmental clauses

Leed regulation:

Calofer conforms to the requirements of LEED.

Low -Emitting Materials: Adhesives and

Sealants. SCAQMD rule 1168. Complies with

USGBC LEED® 2009 Credit 4.1: Low-Emitting

Materials – Adhesives & Sealants concerning

the VOC-content.

Remark: This technical data sheet replaces all previous versions. The directives contained in this documentation are the result of our experiments and of our experience and have been submitted in good faith. Because of the diversity of the materials and substrates and the great number of possible applications which are out of our control, we cannot accept any responsibility for the results obtained. Since the design, the quality of the substrate and processing conditions beyond our control, no liability under this publication is accepted. In every case it is recommended to carry out preliminary experiments. Soudal reserves the right to modify products without prior notice.

Soudal NV  
Tel: +32 (0)14-42.42.31

Everdongenlaan 18 - 20  
Fax: +32 (0)14-42.65.14

BE-2300 Turnhout  
www.soudal.com



## Calibration certificate

**Instrument:** S 421  
**Serial number:** 1719 7355  
**Item number:** S695 4120



S 421 SN 17197355

**Test conditions:**

Test medium	Air	Ambient temperature:	18...26 °C
Test temperature:	23 °C	Ambient humidity:	30...60 % rH
Test humidity:	<30 %rH	Ambient pressure:	990...1050 mbar
Test pressure:	6 bar	Calibration range:	Standard
Testing tube D <sub>1</sub> :	53.1 mm	Testing method:	Calibration by comparison

**References used:**

Type	Model	Uncertainty	S/N	Last Calibration
Flow Meter	GSM-D2TA	± 0.2%	178108	01.2019
Flow Meter	LA-5-C-MA-9	± 0.25%	141119E39092	08.2018
Flow Meter	LA-5-C-MA-9	± 0.25%	141119E39094	08.2018
Flow Meter	LA-5-C-MA-9	± 0.25%	141119E39096	08.2018
Pressure	P-30	± 0.05%	2245356	07.2018

**Calibration test results:**

Description	Units	Nominal value	Permissible uncertainty	Actual value	Evaluation
Flow	m3/h	117.9	±(1.5 % + 0.3% FS)	119.1	passed
Flow	m3/h	461.6	±(1.5 % + 0.3% FS)	463.3	passed
Flow	m3/h	812.8	±(1.5 % + 0.3% FS)	810.8	passed

*We hereby confirm, that the above-mentioned measuring system was calibrated according to SUTO iTEC working standard and traceability chain for dew point, temperature and pressure calibrations. The measuring facilities used for calibration are regularly calibrated and are based on national standards. We recommend that this measuring instrument should be calibrated annually.*

The product has been calibrated by:

**SUTO iTEC GmbH**

**Calibration date:** 26 Apr 2019

Werkstr. 2  
 79426 Buggingen  
 Tel: +49 (0)7631 936 889 0  
 Fax: +49 (0)7631 936 889 14  
 E-mail: sales@suto-itec.com  
 Web: www.suto-itec.com

**Inspector:** A.Pietras

**Signature:**



## Factory settings

**Instrument:** S 421  
**Serial number:** 1719 7355  
**Item number:** S695 4120

We hereby confirm, that the above-mentioned measuring system has received following settings before shipment:

### Measurement Setting

Tube diameter:	<b>80.9 mm</b>	Gas type:	<b>Air</b>
Flow unit:	<b>m<sup>3</sup>/h</b>	Operation pressure:	16 bar
Consumption unit:	<b>m<sup>3</sup></b>	Consumption counter:	0
Reference conditions:	Ps = 1000.00 <b>mbar</b> Ts = 20.00 <b>°C</b>	Flow direction:	Standard

### Analogue Output

Output 1:	<b>Flow</b>	Type:	<b>Active</b>
Scaling:	<b>4 mA: 0.0 m<sup>3</sup>/h 20 mA: 2373.7 m<sup>3</sup>/h</b>		
Output 2:	N/A	Type:	N/A
Scaling:	4 mA: N/A 20mA: N/A		

### Counter Output

Type:	Pulse	Pulse per consumption unit:	1
-------	-------	-----------------------------	---

### Fieldbus Interface

#### HART

Fieldbus address	N/A	Preambles:	N/A
------------------	-----	------------	-----

#### Modbus

Device address:	N/A	Baudrate:	N/A
Framing/parity/Stop bit:	N/A	Transmission mode:	N/A

#### M-Bus

Address:	N/A	Manufacturer Code:	N/A
Baudrate:	N/A	Access No.:	N/A

**WIKA Instruments (Pty) Ltd.  
South Africa**



**SANAS Accredited Laboratory  
Number 246  
for  
Pressure Metrology**

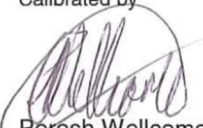
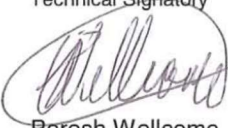


Certificate Number 01-00003101

**CALIBRATION CERTIFICATE**

<p>Calibration of a</p> <p>Manufacturer</p> <p>Type</p> <p>Serial number</p> <p>Customer</p> <p>Order No.</p> <p>Number of pages of the calibration certificate</p> <p>Date of calibration</p> <p><b>Recalibration Date As Per Customer</b></p>	<p>Pressure transmitter</p> <p>Honeywell</p> <p>PX2EF1XX050PAAAX</p> <p>1609810115</p> <p>University of Pretoria Engineering 3 6th Floor Lynnwood Road Pretoria 0002</p> <p>0000640039</p> <p>5</p> <p>09/04/2019</p> <p><b>April 2020</b></p>	<p>This calibration certificate documents the traceability to national standards and international standards, which realise the units of measurement according to the International System of Units (SI).</p> <p>The South African National Accreditation System (SANAS) is a member of the International Laboratory Accreditation Cooperation (ILAC) Mutual Recognition Arrangement (MRA). This arrangement allows for the mutual recognition of technical test and calibration data by member accreditation bodies worldwide. For more information on the arrangement please consult <a href="http://www.ilac.org">www.ilac.org</a></p> <p>The measurement results recorded in this certificate were correct at the time of calibration and the results are only valid for the instrument calibrated. The subsequent accuracy of the instrument will depend on factors such as care, handling, frequency of use, operating temperature and use under conditions other than specified by the manufacturer and or conditions of calibration. It is recommended that recalibration be undertaken, by the user, at an interval that will ensure that the instrument remains within the desired limits.</p> <p>Legal liability shall be limited to the cost of recalibration and or certification, but the applicant indemnifies WIKA INSTRUMENTS against any consequential or other loss.</p>
---	--	---

This calibration certificate may not be reproduced other than in full except with the permission of the issuing laboratory. Calibration certificates without Technical Signatory's signature are not valid.

<p>Date of issue</p> <p>09/04/2019</p>	<p>Calibrated by</p>  <p><b>Peresh Wellcome</b> Metrologist and Lab Manager</p>	<p>Technical Signatory</p>  <p><b>Peresh Wellcome</b></p>
--	--	--

WIKAI Instruments (Pty) Ltd.  
Chilvers Street, Denver, 2094  
Johannesburg, South Africa  
PO Box 75225, Gardenview, 2047

Tel.: (011) 621 0000  
Fax: (011) 621 0059  
email: sales.za@wika.com

**Device Under Test (DUT)**

Pressure transmitter	
Model	PX2EF1XX050PAAAX
Serial No.	1609810115
Scale range	(0 ... 50) psi a
Signal	(0.5 ... 4.5) V
Accuracy	0.25 % FS
Resolution (scale division)	0.001 V
Tag No.	n/a

**Calibration Method**

Calibration was carried out according to DKD-R 6-1 "Calibration of Pressure Gauges" (Edition 03/2014) calibration sequence A, by comparing the measured values of the DUT with those of the Reference or Working Standard. LW-007 r7 & LW-012 r6

**Place of calibration**

WIKA SA Jhb Cal Lab

$$g = (9.7855 \pm 0.0000005) \text{ m/s}^2$$

**Measurement conditions**

Working standard (WS) Pressure controller	
Model	CPC8000 Z80103
Calibration mark	03993360 DKD 01/19
Scale range	(0 ... 35) bar a
Accuracy	0.00457 % FS

WIKA Instruments (Pty) Ltd.  
Chilvers Street, Denver, 2094  
Johannesburg, South Africa  
PO Box 75225, Gardenview, 2047  
Tel.: (011) 621 0000  
Fax: (011) 621 0059  
email: sales.za@wika.com



**Measurement conditions**

**Digital multimeter**

Model	Keithley 2000 DMM
Calibration mark	104412-1 SANAS 09/18

**Assembly of the DUT  
at the time of calibration**

Pressure medium	Dry air
Reference height (for reference value)	Connection of object
Position during calibration	Vertical

**Environmental conditions**

Temperature	21.5 ± 0.50 °C
Atmospheric pressure	834.0 ± 0.60 hPa
Rel. Humidity	67.0 ± 2.00 %

**Measurement results**

Calc. reference value	Reading DUT		
V	M1 ↑	M2 ↓	M3 ↑
0.558	0.543	0.544	0.546
1.000	0.991	0.985	0.991
1.500	1.490	1.487	1.491
2.000	1.990	1.984	1.989
2.500	2.490	2.484	2.490
3.000	2.989	2.984	2.991
3.500	3.489	3.482	3.489
4.000	3.989	3.984	3.987
4.500	4.490	4.488	4.488

WIKA Instruments (Pty) Ltd.  
Chilvers Street, Denver, 2094  
Johannesburg, South Africa  
PO Box 75225, Gardenview, 2047  
Tel.: (011) 621 0000  
Fax: (011) 621 0059  
email: sales.za@wika.com



## Measurement results

$p \text{ in bar} = (\text{Reading} - I_{\text{min}}) \cdot ((P_{\text{min}} - P_{\text{max}}) / (I_{\text{min}} - I_{\text{max}})) + P_{\text{min}}$   
 Alternative calculation:  $p \text{ in psi} = \text{Reading} \cdot 12.5 \text{ psi/V} - 6.25 \text{ psi}$

Reading Reference WS psi	Calculated pressure DUT psi		
	M1 ↑	M2 ↓	M3 ↑
0.725	0.54	0.55	0.58
6.250	6.14	6.06	6.14
12.500	12.38	12.34	12.39
18.750	18.63	18.55	18.61
25.000	24.88	24.80	24.88
31.250	31.11	31.05	31.14
37.500	37.36	37.28	37.36
43.750	43.61	43.55	43.59
50.000	49.88	49.85	49.85

## Evaluation of measurement results

The deviation must be subtracted algebraically from the DUT reading to obtain the correct value.

Reading Reference WS psi	Mean Value psi	Deviation psi	Repeatability psi	Hysteresis psi	Uncertainty of Measurement psi
0.725	0.55	-0.18	0.04	0.01	0.040
6.250	6.11	-0.14	0.00	0.07	0.055
12.500	12.37	-0.13	0.01	0.04	0.040
18.750	18.60	-0.15	0.01	0.08	0.055
25.000	24.85	-0.15	0.00	0.07	0.055
31.250	31.10	-0.15	0.03	0.06	0.051
37.500	37.33	-0.17	0.00	0.09	0.061
43.750	43.58	-0.17	0.02	0.06	0.051
50.000	49.86	-0.14	0.02	0.02	0.039

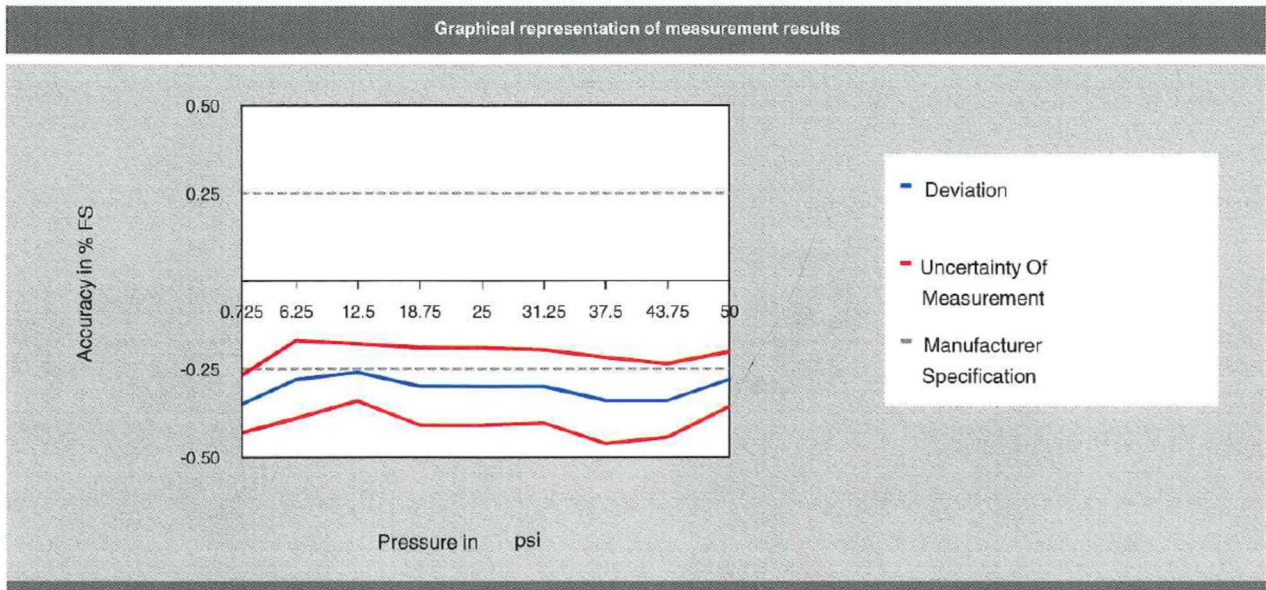
The reported expanded uncertainty of measurement is valid after a correction of the reading value with the systematical deviation (see table "evaluation").

The reported expanded uncertainty of measurement is stated as the standard uncertainty of measurement multiplied by the coverage factor  $k=2$ , which for a normal distribution corresponds to a coverage probability of 95,45%, the uncertainty of measurement has been estimated in accordance with the principles defined in the GUM, 'Guide to Uncertainty of Measurement, ISO, Geneva, 1993'.

To convert in official-unit -kPa- use multiplier : 6.894757 kPa/psi  
 M1 & M3 Indicates Rising Pressure, M2 Indicates Falling Pressure

**NOTE:** All readings entered on computer directly.

**Evaluation of measurement results**



The accuracy of the DUT is 0.241 psi

**Statement of compliance**

**Additional information**

*Partial calibration 0.725 to 50 psi absolute only.*

-----END OF CERTIFICATE-----

WIKA Instruments (Pty) Ltd.  
Chilvers Street, Denver, 2094  
Johannesburg, South Africa  
PO Box 75225, Gardenview, 2047  
Tel.: (011) 621 0000  
Fax: (011) 621 0059



# Appendix D In-stream K-Type thermocouple calibration certificate

**WIKA Instruments (Pty) Ltd  
South Africa**

**SANAS Accredited Laboratory  
Number 346  
for  
Temperature Metrology**



Certificate Number 11-00000856

## CALIBRATION CERTIFICATE

Calibration of a	Thermocouple
Manufacturer	WIKA Instruments (Pty) Ltd
Type	K Simplex
Serial number	800019V3
Tag number	n/a
Customer	University of Pretoria Engineering 3 6th Floor Lynnwood Road Pretoria 0002
Order No.	0000640039
Number of pages of the calibration certificate	3
Date of calibration	15 - 16/05/2019
<b>Recalibration Date As Per Customer</b>	<b>May 2020</b>

This calibration certificate documents the traceability to national standards and international standards, which realise the units of measurement according to the International System of Units (SI).

The South African National Accreditation System (SANAS) is a member of the International Laboratory Accreditation Cooperation (ILAC) Mutual Recognition Arrangement (MRA). This arrangement allows for the mutual recognition of technical test and calibration data by member accreditation bodies worldwide. For more information on the arrangement please consult [www.ilac.org](http://www.ilac.org)

The measurement results recorded in this certificate were correct at the time of calibration and the results are only valid for the instrument calibrated. The subsequent accuracy of the instrument will depend on factors such as care, handling, frequency of use, operating temperature and use under conditions other than specified by the manufacturer and or conditions of calibration. It is recommended that recalibration be undertaken, by the user, at an interval that will ensure that the instrument remains within the desired limits.

Legal liability shall be limited to the cost of recalibration and or certification, but the applicant indemnifies WIKA INSTRUMENTS against any consequential or other loss.

This calibration certificate may not be reproduced other than in full except with the permission of the issuing laboratory. Calibration certificates without Technical Signatory's signature are not valid.

Date of issue	Checked by Laboratory Assistant	Calibrated by Technical Signatory
21/05/2019		
	Sanele Buthelezi Metrologist	Tshepo Mashiloane Metrologist

WIKA Instruments (Pty) Ltd.  
Chilvers Street, Denver, 2004  
Johannesburg, South Africa  
PO Box 75225, Gardenview, 2047

Tel: (011) 621 0000  
Fax: (011) 621 0059  
email: sales.za@wika.com

**Device Under Test (DUT)**

Thermocouple	
Type	K Simplex
Serial Number	800019V3
Transmitter Serial Number	n/a
Transmitter Range	n/a
Transmitter Output Signal	n/a
Tag Number	n/a

**Reference Standards and Equipment used**

The following measuring devices and references were used:

- Range 50°C to 600°C CTD 9300 Dry Block Calibrator S/N 1306179, Cert. 104575-7 08/10/2018
- FLUKE 8508A DMM S/N: 24667011, Cert. 104412-2, 20/09/2018
- WIKA CJC for Thermocouple Type K, s/n TE-8908, Cert. 308-57147 30/04/2019
- Range 0.0°C Ice Point Reference, Demineralised ice and water mixture

The following uniformed temperature devices were used:

- Range 50°C to 600°C CTD 9300 Dry Block Calibrator S/N 1306179, Cert. 104575-7 08/10/2018

**Environmental conditions**

Ambient Temperature in °C 20.25 ± 0.5  
Humidity %RH 37.65 ± 2

**Place of calibration**

WIKA Laboratory Johannesburg

**Calibration procedure**

Method by Comparison  
Work instruction LTW-002 r6, LTW-003 r3 & LTW-005 r2

For calibration the following norm is used:

- DKD-R 5-1 Guideline for calibration of Resistance Thermometers by German Calibration Service "Deutscher Kalibrier Dienst" (DKD) English translation Edition 02/2009

WIKA Instruments (Pty) Ltd.  
Chilvers Street, Denver, 2094  
Johannesburg, South Africa  
PO Box 75225, Gardenvue, 2047  
Tel.: (011) 621 0000  
Fax: (011) 621 0059  
email: sales.za@wika.com





**Results**

Immersion depth (mm)	Reference Temperature °C	DUT					Uncertainty of Measurement ±°C
		Indicated Reading Ω	Indicated Reading mV	Indicated Reading mA	Equivalent Temperature °C	Deviation Temperature °C	
150	100.000	-	4.075	-	99.492	-0.508	0.90
150	300.000	-	12.198	-	299.734	-0.266	1.30
150	600.000	-	24.923	-	600.414	0.414	2.39

The reported expanded uncertainty of measurement is stated as the standard uncertainty of measurement multiplied by the coverage factor k=2, which for a normal distribution corresponds to a coverage probability of 95,45%, the uncertainty of measurement has been estimated in accordance with the principles defined in the GUM, 'Guide to Uncertainty of Measurement, ISO, Geneva, 1993'.

**Remarks**

1. Standard used to convert resistance to temperature: IEC 60751:2008
2. Standard used to convert millivolts to temperature: IEC 60584-1:2013
3. The deviation must be subtracted algebraically from the DUT reading to obtain the correct temperature reading.

**Label**

The calibration object is labelled, which shows the number of this calibration certificate, serial/tag number and the date of calibration.

-----END OF CERTIFICATE-----

WIKA Instruments (Pty) Ltd.  
 Chilvers Street, Denver, 2094  
 Johannesburg, South Africa  
 PO Box 75225, Gardenview, 2047  
 Tel.: (011) 621 0000  
 Fax: (011) 621 0059  
 email: sales.za@wika.com



# Appendix E Weld-pad K-Type thermocouple calibration certificate

**WIKA Instruments (Pty) Ltd  
South Africa**

**SANAS Accredited Laboratory  
Number 346  
for  
Temperature Metrology**


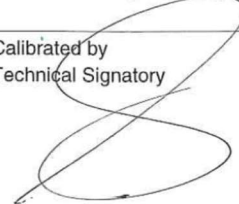


Certificate Number 11-00000926

## CALIBRATION CERTIFICATE

<p>Calibration of a                      Thermocouple</p> <p>Manufacturer                          WIKA Instruments (Pty) Ltd</p> <p>Type                                      K Simplex</p> <p>Serial number                          80001AIF</p> <p>Tag number                              n/a</p> <p>Customer                                University of Pretoria Engineering 3 6th Floor Lynnwood Road Pretoria 0002</p> <p>Order No.                                0000640039</p> <p>Number of pages of the calibration certificate                      3</p> <p>Date of calibration                      03 - 06/06/2019</p> <p><b>Recalibration Date As Per Customer    June 2020</b></p>	<p>This calibration certificate documents the traceability to national standards and international standards, which realise the units of measurement according to the International System of Units (SI).</p> <p>The South African National Accreditation System (SANAS) is a member of the International Laboratory Accreditation Cooperation (ILAC) Mutual Recognition Arrangement (MRA). This arrangement allows for the mutual recognition of technical test and calibration data by member accreditation bodies worldwide. For more information on the arrangement please consult <a href="http://www.ilac.org">www.ilac.org</a></p> <p>The measurement results recorded in this certificate were correct at the time of calibration and the results are only valid for the instrument calibrated. The subsequent accuracy of the instrument will depend on factors such as care, handling, frequency of use, operating temperature and use under conditions other than specified by the manufacturer and or conditions of calibration. It is recommended that recalibration be undertaken, by the user, at an interval that will ensure that the instrument remains within the desired limits.</p> <p>Legal liability shall be limited to the cost of recalibration and or certification, but the applicant indemnifies WIKA INSTRUMENTS against any consequential or other loss.</p>
--	---

This calibration certificate may not be reproduced other than in full except with the permission of the issuing laboratory. Calibration certificates without Technical Signatory's signature are not valid.

<p>Date of issue</p> <p>07/06/2019</p>	<p>Checked by Laboratory Assistant</p>  <p>Sanele Buthelezi Metrologist</p>	<p>Calibrated by Technical Signatory</p>  <p>Tshepo Mashiloane Metrologist</p>
--	--	---

WIKAI Instruments (Pty) Ltd.  
Chilvers Street, Denver, 2094  
Johannesburg, South Africa  
PO Box 75225, Gardenview, 2047

Tel.: (011) 621 0000  
Fax: (011) 621 0059  
email: sales.za@wika.com

# WIKA Instruments (Pty) Ltd South Africa

Certificate Number

11-00000926

Page 2 of 3 pages of calibration certificate dated 03 - 06/06/2019

## Device Under Test (DUT)

### Thermocouple

Type	K Simplex
Serial Number	80001AIF
Transmitter Serial Number	n/a
Transmitter Range	n/a
Transmitter Output Signal	n/a
Tag Number	n/a

## Reference Standards and Equipment used

The following measuring devices and references were used:

- WIKA CTP1000, Serial Number 321087\_5, Cert. TH/RT-7005 21/09/2018
- Range 50°C to 600°C CTD 9300 Dry Block Calibrator S/N 1207223, Cert. 104575-4 09/10/2018
- FLUKE 8508A DMM S/N: 243166990, Cert. 105838-7, 14/02/2019
- WIKA CJC for Thermocouple Type K, s/n TE-8908, Cert. 308-57147 30/04/2019
- Range 0.0°C Ice Point Reference, Demineralised ice and water mixture

The following uniformed temperature devices were used:

- Range 50°C to 600°C CTD 9300 Dry Block Calibrator S/N 1207223, Cert. 104575-4 09/10/2018
- Range -30°C to 160°C WIKA CTB9100 Stirred Liquid Bath, Medium : Silicone Oil M20

## Environmental conditions

Ambient Temperature in °C	22.5 ± 0.5
Humidity %RH	24 ± 2

## Place of calibration

WIKA Laboratory Johannesburg

## Calibration procedure

Method	by Comparison
Work instruction	LTW-002 r6, LTW-003 r3 & LTW-005 r2

For calibration the following norm is used:

- DKD-R 5-1 Guideline for calibration of Resistance Thermometers by German Calibration Service "Deutscher Kalibrier Dienst" (DKD) English translation Edition 02/2009

WIKA Instruments (Pty) Ltd.  
Chilvers Street, Denver, 2094  
Johannesburg, South Africa  
PO Box 75225, Gardenvue, 2047  
Tel.: (011) 621 0000  
Fax: (011) 621 0059  
email: sales.za@wika.com



**WIKA Instruments (Pty) Ltd  
South Africa**

Certificate Number

11-00000926

Page 3 of 3 pages of calibration certificate dated 03 - 06/06/2019

**Results**

Immersion depth (mm)	Reference Temperature °C	DUT					Uncertainty of Measurement ±°C
		Indicated Reading Ω	Indicated Reading mV	Indicated Reading mA	Equivalent Temperature °C	Deviation Temperature °C	
150	50.084	-	2.002	-	49.487	-0.597	0.90
150	250.000	-	10.174	-	250.513	0.513	1.79
150	500.000	-	20.670	-	500.600	0.600	1.99

The reported expanded uncertainty of measurement is stated as the standard uncertainty of measurement multiplied by the coverage factor k=2, which for a normal distribution corresponds to a coverage probability of 95,45%, the uncertainty of measurement has been estimated in accordance with the principles defined in the GUM,'Guide to Uncertainty of Measurement, ISO, Geneva, 1993'.

**Remarks**

1. Standard used to convert resistance to temperature: IEC 60751:2008
2. Standard used to convert millivolts to temperature: IEC 60584-1:2013
3. The deviation must be subtracted algebraically from the DUT reading to obtain the correct temperature reading.

**Label**

The calibration object is labelled, which shows the number of this calibration certificate, serial/tag number and the date of calibration.

-----END OF CERTIFICATE-----

WIKA Instruments (Pty) Ltd.  
Chilvers Street, Denver, 2094  
Johannesburg, South Africa  
PO Box 75225, Gardenview, 2047  
Tel.: (011) 621 0000  
Fax: (011) 621 0059  
email: sales.za@wika.com



## **Appendix F Error propagation analysis**

### **F.1 Measurement equipment**

The objective of the testing was to gather data, the most important of which for this experiment was the inlet and outlet temperatures of the recuperator core, so that the experimental effectiveness may be found and compared to the theoretical model. To achieve this, the TC 40 K-type thermocouple from WIKA was chosen. This particular thermocouple was chosen because it has a measurement range of  $-40\text{ }^{\circ}\text{C}$  to  $1260\text{ }^{\circ}\text{C}$ , which greatly encompasses the possible temperatures that could be expected during testing. It also comes in both an in-stream and weld-pad (surface temperature) variant, it can be ordered with fully customisable lengths and wire sheathing and it has a reliable construction that has been tested and is trusted. Another advantage to implementing the TC 40 is that WIKA can perform a certified calibration at the operational conditions specified by the client, in their SANAS approved facility.

The second parameter measured was that of pressure. It is necessary to identify at which hypothetical compressor pressure ratio the test is being performed, what the pressure losses are for the recuperator as well as to determine the mass flow rate. The mass flow rate was calculated by considering both the temperature and pressure measurements on either side of the throttle plate. In doing so, using Mach number relations for air flow through the throttle plate hole, the mass flow rate was determined. A calibrated Suto S421 mass flow meter was used to determine the total mass flow rate through the recuperator core. Since a compressor pressure ratio of 2.5 can be considered the maximum value that may ever be tested with the STBC due to the limitations of turbochargers, a pressure transducer that has a maximum value slightly above 130.5 kPa gauge (218 kPa absolute) pressure would be best. A sensor that measures too high will result in the resolution of the data being too coarse and the likelihood of encountering measurement noise or inconsistencies increases when only operating at the low end (below 30%) of the sensor's range. Finding the appropriate sensor was not easy. There were many sensors that measured up to 1 MPa absolute pressure, but in that case, measurement would occur below 20% of its range. Finally, a Honeywell PX2EF1XX050PAAAX ratiometric pressure transducer was found that has a maximum absolute operating pressure of 50 psi (344.74 kPa). This would allow for measurement to occur in 40-60% of the transducer's range. Although not ideal, a transducer that measured lower but still high enough to capture the operating points did not seem to be available. These sensors were also chosen because they are made by Honeywell, and were likely to be well constructed and thus adhere to their specifications and work reliably. The accuracy is stated to be  $\pm 0.25\%$  of the measured value.

These particular transducers output a voltage which is a percentage of the voltage supplied to them, hence the name ‘ratiometric’. These transducers require a supply voltage of 5 V. 0 kPa is set at 10% (0.5 V) and 344.74 kPa at 90% (4.5 V) of 5 V. Hence a function can be applied to these values to take a measured voltage from the transducer and determine the pressure value. This function is represented as Equation (F-1). Like the thermocouples, these transducers were also sent to WIKA to be calibrated and certified.

$$P = 86.1845(V) - 43.09225 \quad (F-1)$$

The final key component when gathering data during testing is the logger itself. The unit in question is the Keysight 34972A LXI data acquisition unit. The Keysight logger takes inputs from thermocouples, pressure transducers and any voltage output from a plethora of sensors, and with the aid of an application on a computer, displays and logs the data for further analysis. The Keysight has an accuracy of 1 °C for K-type thermocouple measurements and 0.0041% when measuring DC voltage.

## F.2 Error analysis

Equations (F-2) and (F-3), derived from the Gaussian equation for normally-distributed errors, show the effect that addition and subtraction, Equation (F-2), as well as multiplication and division, Equation (F-3), have on the propagation of errors.

$$\delta Q = \sqrt{(\delta a)^2 + (\delta b)^2 + \dots + (\delta z)^2} \quad (F-2)$$

$$\frac{\delta Q}{|Q|} = \sqrt{\left(\frac{\delta a}{a}\right)^2 + \left(\frac{\delta b}{b}\right)^2 + \dots + \left(\frac{\delta z}{z}\right)^2} \quad (F-3)$$

### F.2.1 Effectiveness

To analyse the effect that error propagation has on the cold-side effectiveness value, which was experimentally determined for Test 2, Equation (F-4) is considered.

$$\varepsilon_c = \frac{\dot{Q}_c}{\dot{Q}_{max}} = \frac{\dot{m}_{tot} C_{p,c} (T_{c,o} - T_{c,i})}{\dot{m}_{tot} C_{p,c} (T_{h,i} - T_{c,i})} = \frac{T_{c,o} - T_{c,i}}{T_{h,i} - T_{c,i}} \quad (F-4)$$

The error associated with the TC 40 in-stream thermocouples is provided by the calibration certificate in Appendix D. The uncertainty of the temperature measurement is dependent on the temperature. Table F-1 lists the uncertainties at various temperatures.

Temperature [°C]	Uncertainty [°C]
100	± 0.9
300	± 1.3
600	± 2.39

**Table F-1 In-stream thermocouple uncertainties at various temperatures.**

A polynomial curve was fitted to the data represented in Table F-1, which has a correlation coefficient of  $R^2 = 1$ , and produced Equation (F-5).

$$Uncertainty(T) = 0.00000327(T)^2 + 0.00069333(T) + 0.798 \quad (F-5)$$

[°C]	Temperature value	Uncertainty
Cold inlet temperature ( $T_{c,i}$ )	22.4	0.82
Cold outlet temperature ( $T_{c,o}$ )	479.8	1.88
Hot inlet temperature ( $T_{h,i}$ )	577	2.29

**Table F-2 Test 2 experimental temperatures and associated uncertainties.**

Therefore, considering the information in Table F-2 as well as Equation (F-2), the effect of the combined thermocouple and data logger uncertainties can be determined for each temperature.

$$\delta T_{c,i} = \sqrt{(0.82)^2 + (1)^2} = 1.29 \text{ } ^\circ\text{C} \quad (F-6)$$

$$\delta T_{c,o} = \sqrt{(1.88)^2 + (1)^2} = 2.13 \text{ } ^\circ\text{C} \quad (\text{F-7})$$

$$\delta T_{h,i} = \sqrt{(2.29)^2 + (1)^2} = 2.5 \text{ } ^\circ\text{C} \quad (\text{F-8})$$

Utilising the combined uncertainties for each temperature, the uncertainty due to temperature difference can be found by implementing Equation (F-2) once more.

$$\delta(T_{c,o} - T_{c,i}) = \sqrt{(2.13)^2 + (1.29)^2} = 2.49 \text{ } ^\circ\text{C} \quad (\text{F-9})$$

$$\delta(T_{h,i} - T_{c,i}) = \sqrt{(2.5)^2 + (1.29)^2} = 2.81 \text{ } ^\circ\text{C} \quad (\text{F-10})$$

$$T_{c,o} - T_{c,i} = 479.8 - 22.4 = 457.4 \text{ } ^\circ\text{C} \quad (\text{F-11})$$

$$T_{h,i} - T_{c,i} = 577 - 22.4 = 554.6 \text{ } ^\circ\text{C} \quad (\text{F-12})$$

Thus, the total uncertainty associated with the cold-side effectiveness can now be determined by substituting the results from Equations (F-9) to (F-12) into Equation (F-3).

$$\therefore \frac{\delta \varepsilon}{|\varepsilon|} = \sqrt{\left(\frac{2.49}{457.4}\right)^2 + \left(\frac{2.81}{554.6}\right)^2} = 0.0074 \approx \pm 0.74 \%$$

## F.2.2 Pressure loss

The total pressure loss can be characterised by Equation (F-13).

$$\Delta P_{tot} = (P_{c,o} - P_{c,i}) + (P_{h,i} - P_{h,o}) \quad (\text{F-13})$$

Because of the small uncertainty in DC voltage measurement of the data acquisition unit (Keysight 34972A LXI), it will be omitted from the uncertainty analysis. Therefore, the only uncertainty which plays a role in the cascading uncertainty is the pressure transducer uncertainty. According to the calibration certificate in Appendix C which provides the



uncertainty of the most inaccurate transducer, the pressure transducer uncertainty is 0.241 psi (1.66 kPa). Equations (F-14) to (F-16) detail the calculation of the uncertainty associated with the total pressure loss.

$$\delta(P_{c,o} - P_{c,i}) = \sqrt{(1.66)^2 + (1.66)^2} = 2.35 \text{ kPa} \quad (\text{F-14})$$

$$\delta(P_{h,i} - P_{h,o}) = \sqrt{(1.66)^2 + (1.66)^2} = 2.35 \text{ kPa} \quad (\text{F-15})$$

$$\therefore \delta(\Delta P_{tot}) = \sqrt{(2.35)^2 + (2.35)^2} = \pm 3.32 \text{ kPa} \quad (\text{F-16})$$